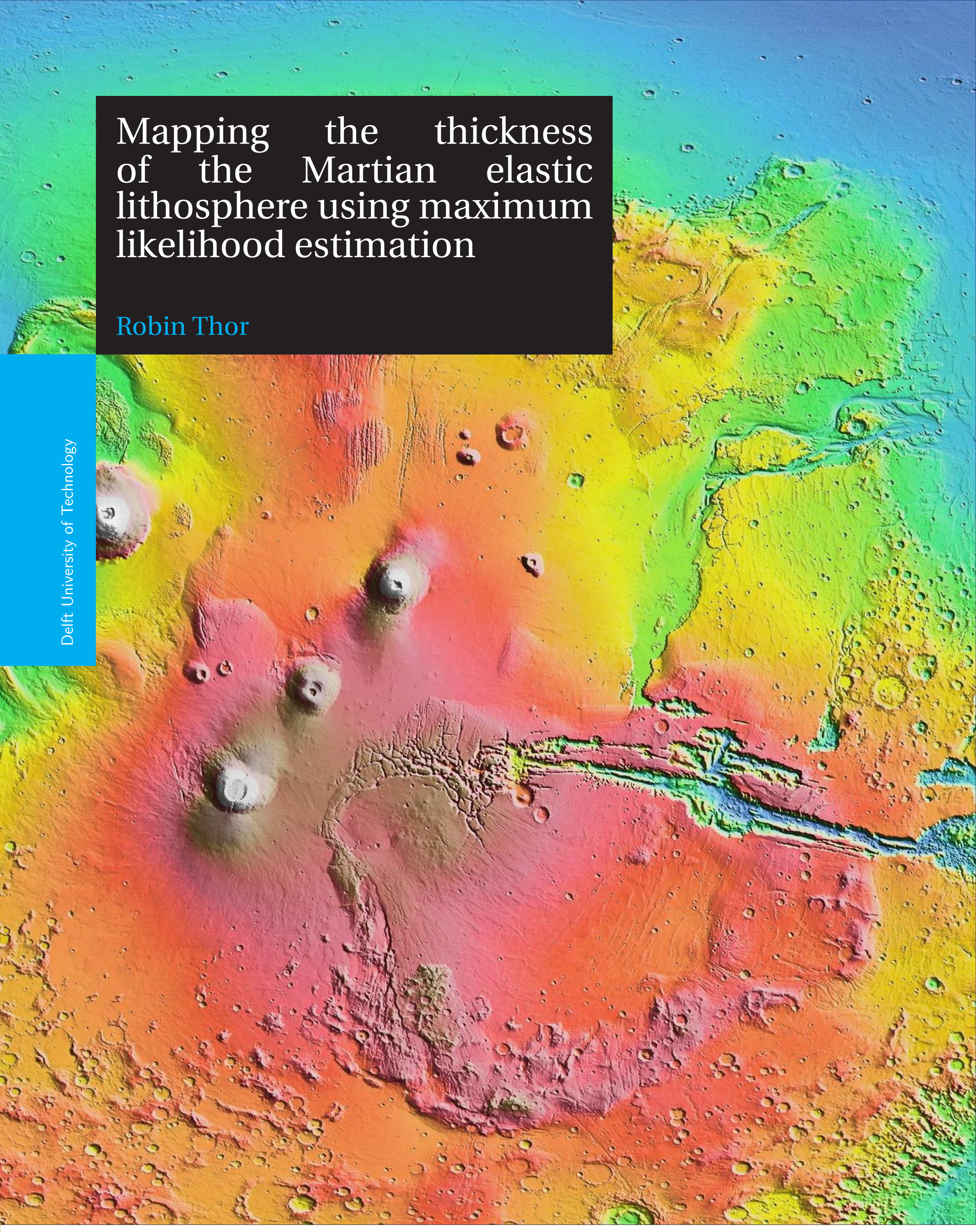

Mapping the thickness of the Martian elastic lithosphere using maximum likelihood estimation

Robin Thor

Delft University of Technology

TU Delft Delft University of Technology

Challenge the future

Mapping the thickness of the Martian elastic lithosphere using maximum likelihood estimation

by

Robin Thor

in partial fulfillment of the requirements for the degree of

Master of Science
in Civil Engineering

at the Delft University of Technology,
to be defended publicly on Tuesday June 28, 2016 at 14:00.

Student number:	4326563	
Supervisor:	Prof. dr. L. L. A. Vermeersen	
Thesis committee:	Dr. ir. W. van der Wal,	TU Delft
	Dr. R. E. M. Riva,	TU Delft
	Ir. B. C. Root,	TU Delft

Delft University of Technology

Abstract

The outermost strong part of a planet is called the lithosphere. When loads, such as volcanoes, sediments, or intrusions, are applied to the lithosphere, it flexes. The amount of flexure is controlled by the flexural rigidity of the lithosphere. The elastic thickness T_e is the thickness of an equivalent fully elastic spherical shell which flexes in the same way as the real lithosphere. It is an important quantity because it strongly depends on the lithospheric heat flux at the time that the load was applied, which is controlled by the thermal evolution of the planet and varies in space and time. The loads and the associated lithospheric deflections cause gravity anomalies and topographic relief. Observations of these can be used to constrain T_e.

In this study, a global map of the elastic thickness of Mars is presented. Several recent missions to Mars have provided global spherical harmonics data sets of gravity and topography. These data are inverted for the shape of the crust-mantle boundary, or equivalently the crustal thickness. This is assuming that all gravity anomalies are caused by only two density interfaces which are the surface and the crust-mantle boundary. The large amplitudes of the Martian gravity field necessitate the application of a finite amplitude correction. A simple, but realistic model, which allows loading and compensation at the same two interfaces, is derived. It uses the differential equations for the flexure of a thin elastic shell and depends on six parameters: the elastic thickness T_e, the ratio F of the amplitude of the loads at the two interfaces before flexure, the correlation r between these loads, and three parameters of a covariance function of the isotropic Matérn class which describes the topography before flexure. The input data are localized to specific grid points of a map using multitaper spectral estimation. Contrary to most elastic thickness studies which compute observed and modelled admittance or coherence to find a best-fit solution for T_e, this study uses maximum likelihood estimation as first proposed by Simons and Olhede (2013). This technique allows to determine the parameter set which is most likely to have produced the localized estimates of the topography and the shape of the crust-mantle boundary.

Maps of the most likely parameter sets are presented for different localization window sizes. The results generally agree with previous studies, yielding $T_e = 10\,\mathrm{km}$ in the southern uplands and higher values at the large volcanoes. This also corresponds to thermal evolution models predicting a more rigid lithosphere in more recently formed areas. Log-likelihood contours and Monte Carlo simulations with synthetically generated topographies reveal the quality of the results. The elastic thickness is well constrained in the southern uplands and at Elysium and Ascraeus Mons, but poorly constrained in the northern lowlands and at the other volcanoes. While this study shows that it is possible to retrieve T_e with maximum likelihood estimation, more research is needed to explain these poor constraints.

Cover figure: The Tharsis province. Laser altimetry data from MOLA (Source: `http://mola.gsfc.nasa.gov/images.html`).

Acknowledgments

I would like to thank F. Simons, M. Wieczorek, P. Audet, and A. Lang for fruitful discussions, and especially Bart Root for his help and guidance during the entire research and writing process.

Robin Thor
Delft, June 2016

Contents

1

Introduction

1.1. Geologic history of Mars

Since the late 1990's, Mars has been visited by several spacecrafts and landers, providing us with a large amount of data which has helped to understand the planet and its history.

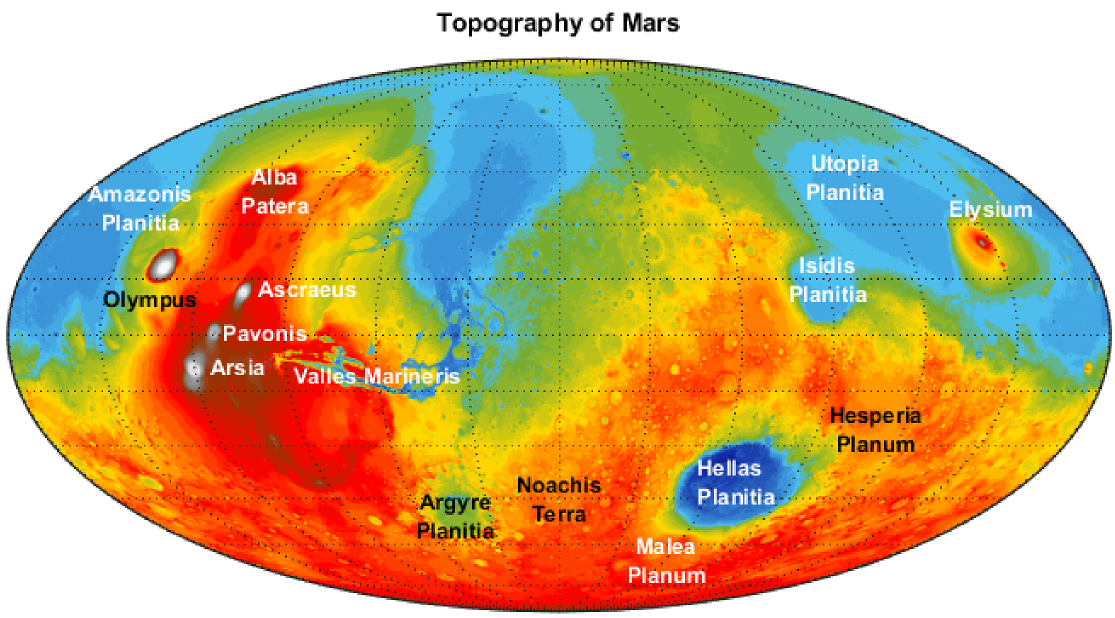

Figure 1.1: Topographic features superimposed on a map of the shape of Mars.

The history of Mars has been divided in three epochs: the Noachian, the Hesperian, and the Amazonian.
Little is known about the pre-Noachian period because no surfaces from that era remain, but the Martian dichotomy, a stark contrast in topography between the Northern and Southern Hemisphere whose origin remains unknown (Nimmo, 2002), has its origins in that time. The Southern Hemisphere is heavily cratered and its surface elevation is about 5 km higher than that of the Northern Hemisphere (Smith et al., 1999b). Thus, it must be older than the smooth Northern Hemisphere which has been resurfaced at some later point (Smith et al., 1999b), probably through liquid water erosion (Di Achille and Hynek, 2010; Head et al., 1999), although this ocean hypothesis remains contested.
The Noachian is named after the heavily cratered Noachis Terra (Figure 1.1), which characterizes the oldest period in Martian history. The beginning of the Noachian is marked by the formation of the Hellas impact basin approximately 3.8 to 4.1 Ga ago. It is the largest impact basin still clearly visible in the topography today and has the lowest elevation of the whole Martian surface with a total depth of 9 km (Smith et al., 1999b).

In the Noachian, cratering rates were very high. Especially large impacts formed both the Argyre and Isidis basins during this time (Carr and Head, 2010). Contrary to the Earth, some surfaces from this epoch are still preserved because of the absence of plate tectonics and less erosion on Mars. The Tharsis rise is an enormous volcanic province centered at 100° W on the Martian equator (Wieczorek, 2007) which probably began developing in the Noachian. The region encompasses about one fifth of the planet's surface area (Lowry and Zhong, 2003) and rises to 7 km above the surrounding terrain, not including the actual volcanoes (Beuthe et al., 2012). Together with the dichotomy, the Tharsis rise has caused a remarkable difference between the center of mass and center of figure of Mars of about 3.3 km (Wieczorek, 2007).

The Hesperian, following the Noachian, started about 3.7 Ga ago. It is named after Hesperia Planum whose surface characterizes this epoch. In the Hesperian, volcanism continued at a similar rate as in the Noachian, and about 30% of the planet was resurfaced. In this epoch, the Valles Marineris rift system probably formed.

The Amazonian is the most recent epoch in the geological history of Mars. Although the Hesperian-Amazonian boundary is very uncertain, the current Amazonian epoch is estimated to have begun approximately 3.3 to 2.9 Ga ago. It is named after Amazonis Planitia, a very smooth plain between Olympus and Elysium Mons. Amazonian surfaces are only sporadically cratered because cratering rates have dropped significantly. Although volcanic activity has declined with respect to the Hesperian, large areas were resurfaced in the Amazonian. The major volcanoes formed in this epoch. Olympus Mons is the largest volcano with an elevation of 22 km with respect to the areoid defined by the Mars Orbiter Laser Altimeter (MOLA). Additionally, Elysium Mons and the Tharsis Montes Ascraeus, Pavonis, and Arsia were also formed in the Amazonian.

A driving factor to many of these changes and an important quantity for the evolution of Mars is the heat flow, which mainly depends on the abundance of radiogenic heat producing elements in the crust and mantle. Modelling suggests that shortly after the formation of Mars, the heat flow was very high, possibly from 60 to $70\frac{\mathrm{mW}}{\mathrm{m}^2}$ Carr and Head (2010). With time, Mars became colder and the heat flow declined almost linearly to a present value of $6.4\frac{\mathrm{mW}}{\mathrm{m}^2}$ exhibiting considerable regional differences (Hahn et al., 2011). The current value is estimated from the abundance of heat producing elements derived from gamma-ray spectrometry.

For a more detailed review of the Martian geologic history, the reader is referred to Carr and Head (2010).

1.2. ELASTIC THICKNESS

The inner structure of terrestrial planets can be described both mechanically and chemically. From a mechanics point of view, the uppermost strong layer is the lithosphere which behaves elastically on geological time scales and is at least as thick as the crust, but often also includes the upper part of the mantle. It is underlain by the ductile and viscous asthenosphere. Chemically, the crust and mantle can be distinguished by their different seismic velocities and densities. On Mars, the crust and mantle have differentiated within the first few millions of its formation.

The MOLA instrument on the Mars Global Surveyor mission has provided us, for the first time, with high resolution topography data by means of laser altimetry. Radio science experiments aboard the Mars Global Surveyor, Mars Express, and the Mars Reconnaissance Orbiter complemented MOLA's data with high resolution gravity measurements which made it possible to reliably determine the structure of the crust and upper mantle (Zuber et al., 2000). These remotely sensed data will remain the best way to probe the subsurface of Mars until a seismometer is deployed to the surface as planned for the InSight mission due for launch in 2018 (Zuber, 2001, `http://insight.jpl.nasa.gov/science.cfm`). From the subsurface structure, insights can be gained about composition, differentiation, and mantle flows (McKenzie et al., 2002; Zuber et al., 2000).

In the gravity field, the hemispherical dichotomy behaves contrary to the topography. The Southern Hemisphere is mostly smooth, indicating widespread isostatic compensation, whereas large gravity anomalies in the Northern Hemisphere lack topographic expression (Smith et al., 1999a). This difference in compensation may be explained by a thinner, but stronger crust in the Northern Hemisphere than in the Southern (Smith et al., 1999a).

The effective elastic thickness of the lithosphere is a measure of the flexural rigidity which describes the behavior of the lithosphere when loads are applied vertically. It is not a physical quantity describing the depth to an actual interface in the planetary lithosphere, but instead refers to a hypothetical, fully elastic plate which possesses the same flexural properties as the real lithosphere (Watts and Burov, 2003). It can, however, also be regarded as the depth to the isotherm at which the material becomes too weak to support loads over geologically long periods of time (McKenzie and Fairhead, 1997) which lies at $\sim 650\,°\mathrm{C}$ on Mars (Zuber et al., 2000) and at $\sim 450-600\,°\mathrm{C}$ on Earth (Burov and Diament, 1995). An elastic thickness which is larger than the crustal thickness implies high mantle strength (Burov and Watts, 2006). The elastic thickness of the lithosphere strongly depends on the lithospheric heat flux and thermal gradient (McGovern et al., 2002; Zuber et al., 2000) and is thus a function of time. On a generally cooling planet, the elastic thickness increases over time. Elastic thickness T_e and flexural rigidity D are related by the equation (Timoshenko and Woinowsky-Krieger, 1959)

$$D = \frac{ET_e^3}{12(1-\nu^2)} \tag{1.1}$$

where E is Young's modulus and ν is Poisson's ratio.
The lithosphere is in complete hydrostatic equilibrium when the flexural rigidity or, equivalently, the elastic thickness is zero. This case is called local isostasy and can be described by the Airy-Heiskanen model where loads are compensated by changes in crustal thickness or by the Pratt-Hayford model where loads are compensated by density variations in the crust (Watts, 2001). Intermediate values of the elastic thickness correspond to regional isostasy, as suggested by Vening-Meinesz. In the Bouguer case, a theoretical case of a plate of infinite rigidity, no isostasy exists, and surface and subsurface processes are decoupled (Forsyth, 1985; Watts, 2001).
There are three common methods for estimating the elastic thickness: forward modelling, inverse modelling, and rheological modelling (Kirby, 2014).
In forward modelling, the observed topography is used to calculate the expected gravity anomaly assuming a value of T_e and then the observed and calculated gravity anomalies are compared in the spatial domain. T_e is then chosen as the value that yields the best fit between calculated and observed gravity anomalies (e.g. Burov and Watts, 2006).
Dorman and Lewis (1970) refrained from assuming a non-linear hypothesis of Airy or Pratt compensation for the computation of isostasy, and instead advocated for using a linear transfer function, which they called the isostatic response function. The gravity and topography are related by

$$\Delta g_c = q * h, \tag{1.2}$$

where h is the topography, Δg_c the gravity anomaly due to compensation, and q is the isostatic response function. The operation $*$ indicates convolution, and hence it is obvious to perform the computations in the spectral domain. In inverse modelling, the misfit between the transform of the linear transfer function and the model prediction is minimized to determine the optimal value of T_e (e.g. Burov and Watts, 2006; McKenzie and Bowin, 1976; Zuber et al., 2000). Spectral modelling is also better than modelling in the spatial domain when dealing with long wavelength features which are unrelated to compensation (Wieczorek, 2007).
Both forward and inverse modelling are based on observations of gravity and topography. They can only reveal the elastic thickness at the time of loading because gravity and topography have not changed since loading occurred. In this study, the notion of elastic thickness implicitly refers to the the elastic thickness at the time of loading, unless otherwise stated.
Finally, rheological models determine T_e from yield strength envelopes, which depend on the internal temperature profile, strain rate, and rheological parameters and indicate the lithospheric strength as a function of depth (Burov and Diament, 1995; Grott and Breuer, 2008; Tesauro et al., 2012). They do not directly depend on gravity and topography and can therefore serve as an independent control for T_e results from forward and inverse modelling.
Estimates of the elastic thickness at the time of loading make conclusions about the thermal evolution and origin of surface features of Mars possible. Generally, the elastic thickness is lower in older surface regions on Mars because these regions formed when the planet was younger and the heat flux was still high (Zuber, 2001). When the age of a feature is well known, accepted, and derived through other methods, the elastic thickness can be used to constrain the heat flow at that time. For example, Grott and Breuer (2008) compared the elastic thicknesses of surface features of different ages obtained from inverse modelling. They found that the elastic thickness increased from ~20 km in the Noachian to ~70 km in the Amazonian and attributed that to the rapid cooling of Mars. They also applied rheological modelling to determine the elastic thickness using yield strength envelopes. The constraints imposed on the rheological model by the elastic thicknesses obtained from spectral modelling led them to conclude a wet crust and mantle rheology. Conversely, the heat flow can also be modelled independently to constrain the age of a surface feature. To determine today's elastic thickness, gravity and topography can only be used at the poles because the ice caps are a recent loading process. Estimates for the north pole (Phillips et al., 2008) and the south pole (Wieczorek, 2008) have yielded quite different results which also do not agree very well with heat flux models (Grott and Breuer, 2010). Grott

and Breuer (2010) explained high elastic thickness values at the north pole by an uneven distribution of radiogenic heat in the mantle, depositing less excess heat at the north pole and more in active mantle plumes under the Tharsis rise.

1.3. SPECTRAL RATIOS

To obtain estimates of the elastic thickness, measurements of the gravity and topography are thus transformed in the spectral domain. The common procedure is to compute ratios of their observed power spectra and cross-power spectra and compare them to modelled ratios which depend on the elastic thickness as an input parameter to the model. The misfit between model and observations is then minimized to yield an optimal value of the elastic thickness.
The spectral ratios which are used are in principle arbitrary (McKenzie and Fairhead, 1997), however, commonly used are the admittance and the coherence, given by

$$\bar{q} = \frac{\langle \bar{g}\bar{h}^{*}\rangle}{\langle \bar{h}\bar{h}^{*}\rangle}, \tag{1.3}$$

and

$$\gamma^2 = \frac{|\langle \bar{g}\bar{h}^{*}\rangle|^2}{\langle \bar{g}\bar{g}^{*}\rangle\langle \bar{h}\bar{h}^{*}\rangle}, \tag{1.4}$$

respectively, where the bar indicates Fourier transformed variables, the * indicates the complex conjugate, and $\langle\cdot\rangle$ indicates averaging over a distinct wavenumber band (e.g. Kirby, 2014). The admittance was found by McKenzie and Bowin (1976) to be identical to the Fourier transform of the isostatic response function from Equation 1.2. Either free-air or Bouguer gravity anomalies can be used as input gravity observations. After the publication of Forsyth (1985) it has been common practice to use the Bouguer coherence for the inversion of T_e (e.g. Djomani et al., 1999; Lowry and Smith, 1994; Simons et al., 2000) because it is more sensitive to T_e than the free-air admittance (Watts and Burov, 2003), but McKenzie and Fairhead (1997) and McKenzie (2003) advocated for using the free-air admittance instead, arguing that the high values of T_e resulting from most Bouguer coherence studies would not match geophysical expectations, and finding T_e values of about 25 km. Specifically, they argued that elastic thicknesses of 100 km to 130 km correspond to geotherms which should not be able to support elastic stresses, and that the seismogenic thickness T_s, which is the thickness of the layer in which most earthquakes occur, should be higher than the elastic thickness. However, Pérez-Gussinyé et al. (2004) found that the differences between the lower results of McKenzie and Fairhead (1997) and those obtained by other studies are not principally due to the usage of a different spectral ratio, but rather originate from different methodologies. Watts and Burov (2003) and Burov and Watts (2006) then argued that T_s and T_e are not directly related to each other because T_s represents the strength of the uppermost crust on short time scales, while T_e represents the integrated strength of the lithosphere over long time scales, so that occasionally, T_e can in fact be smaller than T_s. Wieczorek (2007) pointed out that any good model must fit both spectral ratios and proposed a joint inversion of coherence and admittance which was first carried out by Audet (2014). McKenzie (2015) showed that the Bouguer coherence does not depend on T_e in areas where there is little coherence between the free-air gravity and the topography and deemed the T_e estimates produced by the Bouguer coherence method in such regions as meaningless. Such areas are often found when the topography is almost flat over large regions due to processes like erosion and sedimentation, and especially also in the Northern Hemisphere of Mars (Zuber et al., 2000). Nevertheless, the debate is still ongoing today (Kirby, 2014; McKenzie, 2015).

1.4. GEOPHYSICAL MODELS

On Mars, the elastic thickness has so far been calculated locally for the Tharsis region (Belleguic et al., 2005; Beuthe et al., 2012; Lowry and Zhong, 2003; McKenzie et al., 2002), for the Elysium region (Belleguic et al., 2005; McKenzie et al., 2002), for the dichotomy boundary (Nimmo, 2002), for the northern lowlands (Hoogenboom and Smrekar, 2006), for the south pole (McKenzie et al., 2002), and for a variety of other surface features and regions (McGovern et al., 2002, 2004; McKenzie et al., 2002), and has recently been mapped globally for the first time by Audet (2014). Audet (2011) compute admittance and coherence globally under consideration of anisotropy, but could not estimate the elastic thickness from those values because they lacked a suitable

spherical flexure model which also takes into account anisotropy.
There have been several missions probing the gravity field through radio science experiments, but all of them have been flying in near-polar areocentric orbits. This causes aliasing when computing the spherical harmonics coefficients of the gravity field which are therefore inaccurate (McKenzie et al., 2002). Several studies on Mars (Beuthe et al., 2012; McKenzie et al., 2002; Nimmo, 2002) have therefore computed the admittance from the line-of-sight Doppler accelerations directly without using the spherical harmonics representation of the gravity field. Inverting for the elastic thickness along such one-dimensional tracks is an intrinsically local method (Beuthe et al., 2012). For the creation of global maps it is more convenient to use global gravity and topography data sets. In such two-dimensional treatments, there is also more data available, which causes the results to be less noisy, so that smaller windows can be applied (McKenzie et al., 2002). While on Earth, most studies use two-dimensional Cartesian coordinate systems, the planetary science community has preferred to work in spherical coordinates (Audet, 2014). The distortions caused by projection of the data fields onto a Cartesian grid and the subsequent reprojection of the results onto the sphere are larger for bodies with a smaller radius of curvature. The same holds for the effect of neglecting membrane stresses in Cartesian models (Turcotte et al., 1981). Thus, for small bodies like Mars, the choice of coordinate system makes a non-negligible difference.
A model of the lithosphere is used to relate the elastic thickness to the gravity and topography. Most commonly it is modelled as a thin elastic plate of infinite lateral extent on top of an inviscid asthenosphere in the Cartesian domain, or as a thin elastic shell in the spherical domain, respectively. Before the study of Forsyth (1985), models without bottom loads were common, but inconsistent (Kirby, 2014; Lowry and Zhong, 2003) and biased (Stark et al., 2003) results were achieved. Nowadays, loads are usually applied as undulations of the density interfaces at the surface and the Mohorovičić discontinuity, often denoted as top and bottom loads, respectively. This implies that the upper layer uses the crustal density and the lower layer the mantle density.
The models require several input parameters, which can either be solved for or be assumed to be known. These parameters include the densities of the layers, crustal thickness, elastic moduli, and ratio and phase correlation of top and bottom loads. While the internal density structure of the Earth is quite well known, the data situation on Mars is much worse, and the only way to meaningfully improve it is by placing a seismometer on the surface (Beuthe et al., 2012; Neumann et al., 2004; Zuber, 2001). Therefore, McGovern et al. (2002) jointly estimated the elastic thickness and either load density, or crustal thickness, or load ratio, thus solving for two parameters at a time, but for four in total. When multiple parameters are solved for, it becomes increasingly non-trivial to find that parameter set which constitutes the optimal solution. Few studies mention their solution strategy, but for example Kirby and Swain (2009) used a least-squares estimation technique and Audet (2014) applied a neighbourhood algorithm.
An even bigger controversy is the proper estimation of load ratio F and correlation r (Audet, 2014; Kirby, 2014). The load ratio is given by (Kirby, 2014)

$$F = \frac{f}{1+f}, \tag{1.5}$$

with

$$f^2 = \frac{\langle L^b L^{b*} \rangle}{\langle L^t L^{t*} \rangle} \tag{1.6}$$

and where L^b and L^b are the (unknown) bottom and top loads in the spectral domain, respectively. A load ratio of zero corresponds to a model which only considers loads at the surface and a load ratio of one signifies that loads are only present at the Mohorovičić discontinuity. The load correlation takes values between -1 and 1, and expresses the phase difference between top and bottom loads. Both F and r are needed to calculate spectral ratios for given T_e.
Forsyth (1985) first proposed a method to “deconvolve the loads” (Lowry and Smith, 1994) and retrieve F as a function of wavelength under the assumption of zero correlation between the loads, thereby potentially describing the physical world better than with an inversion for a value of F which is uniform over all wavelengths. His method exactly reproduces the observation because the load ratio is wavelength dependent. Kirby and Swain (2009) compared the load deconvolution method with estimating F as an independent parameter which is uniform over all wavelengths and found large differences of over 50 km, but only in those areas where the estimation is unreliable for both methods. Audet (2014) also included F as an independent model parameter. While most studies investigating Earth after Forsyth (1985) have assumed zero correlation

between the phases of the loads, the planetary community has usually assumed perfect correlation ($r = 1$) or anti-correlation ($r = -1$; Belleguic et al., 2005; McGovern et al., 2002). When top and bottom loads are due to the same cause, for example volcanoes, an important origin of loads on Mars, the loads are correlated (Audet, 2011). When top loads develop through surface processes which do not strongly influence the bottom loads, like for example erosion and sedimentation, they are not strongly correlated.
Audet (2014) states that estimating the load correlation in his model would have likely yielded significant improvements, but is difficult to perform for planetary applications because of limited data resolution. Simons and Olhede (2013) developed a model for the joint estimation of elastic thickness, load ratio, and load correlation, and applied it to synthetic data, obtaining encouraging results (McKenzie, 2015).
Numerous variations from this thin elastic two-layer model exist, but so far none yielded significant improvements. For example, McKenzie (2003) included an intermediate load interface in the lithosphere, reformulating the problem as a three-layer model, and McKenzie and Bowin (1976) considered an incompressible elastic plate. A number of approximations have to be made to keep the models sufficiently simple. While tangential loads are important in stress modelling (Banerdt, 1986), they are negligible in elastic thickness modelling (Audet, 2014), and hence as a first approximation, only radial loads are considered. As previously mentioned, a second common approximation is that F and r are considered independent of wavelength. A third approximation is to consider loads as mass sheets without vertical extent located at the density interfaces. The gravity anomaly is then calculated from the topography and the deflected interface at the crust-mantle boundary. This does not have a big impact when the geoid undulation is in the order of 100 m, like on Earth, but can become important on Mars, where the dynamic range of the areoid exceeds 2 km (Smith et al., 1999a) with areoid heights of ~1.8 km in the Tharsis region (Wieczorek, 2007). Wieczorek and Phillips (1998) derived a correction term for this approximation, and McGovern et al. (2002) demonstrated that applying this so-called finite amplitude correction improves the estimated elastic thickness on Mars. The correction has later been refined by Belleguic et al. (2005).
The averaging in Equations 1.3 and 1.4 is in most studies performed over discrete wavenumber annuli, assuming that the properties of the lithosphere are isotropic. It is also possible to average for discrete wavenumber and azimuth bins, thus modelling the lithosphere anisotropically and achieving a more realistic flexural model. Anisotropy reflects the preferred direction of isostatic compensation of the lithosphere due to faulting in the crust. When erosion or sedimentation erase the directionality in the topography, anisotropy is also induced (Audet, 2011; Audet and Mareschal, 2007). Simons et al. (2000) and Audet and Mareschal (2007) both found significant anisotropy in Australia and Canada, respectively. Audet (2011) stresses that the incorporation of anisotropy into flexural models is also important for the Moon and Mars because admittance and coherence signals are sometimes strongly anisotropic. However, flexural models respecting anisotropy only exist for the thin elastic plate to date, and not for the thin elastic sphere.

1.5. SPECTRAL ESTIMATION TECHNIQUES

Equations 1.3 and 1.4 strictly describe signals which are Fourier transformed and then averaged over discrete wavelengths. In actuality, there are various spectral estimation techniques available which all have their respective advantages and limitations. The data are windowed prior to transforming them into the spectral domain and each window applies to one set of parameters which are constant over the extent of that window. For the mapping of the elastic thickness this means in practice that overlapping windows are considered whose centers are the sample points of the map.
The simplest spectral estimation method is the periodogram, but its power is strongly biased, a phenomenon which is known as spectral leakage. One method to decrease that effect is to mirror the signal at the edges to avoid the Gibbs phenomenon while maintaining the spectral properties. However, mirroring causes aliasing when applied to red spectra, i.e. spectra with more power in long wavelengths than in short wavelengths, like that of planetary topography (McKenzie and Fairhead, 1997). Maximum entropy spectral estimation (Lowry and Smith, 1994) also uses extrapolation, but rather of the autocorrelation function than of the original signal, to decrease the effects of data windowing. Lowry and Smith (1994) found that the maximum entropy method produces better estimates than the periodogram, especially for small windows, but also noted a bias in the estimates and a high computational complexity.
Multitaper estimation is another spectral estimation technique which is available in 2D (Hanssen, 1997) and spherical coordinates (Wieczorek and Simons, 2005). In this method, the data are tapered, or windowed, using multiple orthogonal tapers. As shown by Simons et al. (2000), the weighted average of the tapered data then possesses minimal spectral leakage, and the elastic thickness estimates are therefore better than those

produced by the periodogram and maximum entropy methods. The variance of the estimation is lower when more tapers are used. The disadvantage of the multitaper method is that there is always a trade-off between window size and variance (Wieczorek and Simons, 2005). As previously described, small windows are generally desired to avoid large variations of the geophysical parameters in the windowed area, but large windows are needed to recover large wavelengths.

The wavelet transform circumvents the problem of the window size by not using windows in the first place. As previously mentioned, windowing data also always assumes that the geophysical parameters are stationary over the extent of the window (Daly et al., 2004), an approximation which is overcome by the wavelet transform. Its wavenumber resolution increases with increasing wavenumber which can cause spectral leakage in red spectra (Audet and Mareschal, 2007; Kirby, 2014). The wavelet transform is also available in 2D Cartesian and spherical coordinates (Audet, 2011) and has a greater computational efficiency than the multitaper method (Daly et al., 2004).

In recent years, most studies have either used the multitaper method (Beuthe et al., 2012; McKenzie, 2003, 2010; McKenzie and Fairhead, 1997; Pérez-Gussinyé et al., 2004; Simons et al., 2000; Zuber et al., 2000) or the wavelet transform (Audet, 2011, 2014; Audet and Bürgmann, 2011; Audet and Mareschal, 2007; Kirby and Swain, 2009; Stark et al., 2003). Daly et al. (2004) compared the two techniques on real data and found differences of no more than ~25%, and observed consistency with results from maximum entropy estimation and rheological forward modelling as well, but there is no general consensus that one or the other method would provide better estimation results.

In summary, there is still a lot of controversy about the correct way of spectrally estimating the elastic lithospheric thickness. While studies following the methodology of Forsyth (1985) using Bouguer coherence and load deconvolution generally received high estimates in the order of 100 km on Earth, McKenzie and Fairhead (1997) argued that such high values are not realistic and proposed much lower estimates of ~30 km with his free-air admittance method. The inclusion of load ratio and load correlation as model parameters, or as fixed quantities of an assumed value, or obtaining the load ratio independently from deconvolution also all lead to different estimates of T_e which is potentially one of the biggest limitations of current models (Audet, 2014). The multitaper method and the wavelet transform yield relatively similar estimates, but still applying the one or the other method biases comparable results. Nowadays, there is a variety of estimation techniques which have been combined into even more variations, but there is no unique setup emerging as the best or generally accepted approach. This argument needs to be resolved in order to make spectral elastic thickness estimates more valuable for geophysicists and geologists again, especially since the data needed to compute these estimates have become so widely available (McKenzie, 2003). Rheological modelling cannot resolve this issue either. Tesauro et al. (2012) compared rheological modelling to the spectral estimates of Audet and Bürgmann (2011) and found significantly different values in about half of the Earth's continental areas, usually with a higher elastic thickness value coming from the spectral estimation compared to the rheological estimation.

1.6. MAXIMUM LIKELIHOOD ESTIMATION

Recently, a completely new spectral estimation method has been presented by Simons and Olhede (2013). They argued that joining a geophysical model and the observations over an intermediate quantity like admittance or coherence is not a straightforward approach and not statistically rigorous either. Because of the non-Gaussianity of those spectral ratios, they said, minimising the least-squares misfit between observed and computed value is not appropriate. Instead, they proposed to estimate the flexural rigidity from the data as directly as possible using maximum likelihood estimation. This way, spectral ratios such as admittance and coherence are not needed any more. Their approach also includes both load ratio and load correlation as independent parameters into the model, with one value which is uniform over all wavelengths, thereby circumventing another current problem in elastic thickness modelling.

In maximum likelihood estimation, a likelihood function is maximized instead of a least-square misfit. This means that the parameter set is found which is most likely to have produced the observations, and not the one which most accurately describes them (e.g. Myung, 2003). The likelihood function depends on the geophysical model, the model input parameters T_e, F, and r, the Fourier transformed observations, and an assumed covariance function, for which Simons and Olhede (2013) chose the isotropic Matérn covariance function (Matérn, 1960) which depends on another three parameters. The likelihood function is then maximized to find the optimal set of the total of six parameters. The confidence intervals of the parameters can be computed analytically (Simons and Olhede, 2013), but in practice this is difficult because of the necessary localization of the global input fields which would have to be applied to the analytical expressions as well.

1.7. RESEARCH MOTIVATION

The thickness of the Martian elastic lithosphere has already been the subject of several studies in the past decades, most of which focused their investigation on specific surface features. The creation of a global map of the elastic thickness has previously been achieved by Audet (2014) using the wavelet transform and a simultaneous estimation of T_e and F from a joint inversion of both Bouguer and free-air admittance and coherence. His study did not include the finite amplitude correction (Wieczorek and Phillips, 1998) which is necessary because of the high dynamic range of the areoid (McGovern et al., 2002).

Similarly, the goal of this study is to create a global map of the elastic thickness. The map is primarily concerned with the global distribution of the elastic thickness and sheds light into regions that have not yet been thoroughly explored in other studies, such as the northern lowlands of Mars. Unlike other studies using admittance or coherence methods, this study will uniquely be conducted using the maximum likelihood formalism proposed recently by Simons and Olhede (2013) and apply it for the first time to recently collected actual data. The multitaper spectral estimation technique, as described by Wieczorek and Simons (2005), will be applied to localize the input data. To consider the importance of membrane stresses on Mars, the two-layered thin elastic plate model of Simons and Olhede (2013) is transformed to a thin elastic shell model in spherical coordinates. Furthermore, the finite amplitude correction is applied for the retrieval of the subsurface interface.

The principal research question answered by this thesis is thus: What is the global distribution of the elastic thickness on Mars?

2

DATA

2.1. TOPOGRAPHY

The topographic data used in this study originates from the Mars Global Surveyor (MGS) spacecraft and was acquired between 1997 and 2001. The data is available freely at the Planetary Data System (PDS) Geosciences Node (http://pds-geosciences.wustl.edu) where a detailed description of the used measurements and the processing can also be found. The Mars Orbiter Laser Altimeter (MOLA) instrument on MGS was the first altimeter sent to Mars and therefore greatly improved the accuracy of the topography in both vertical and horizontal direction, reaching horizontal and vertical accuracies of $\sim 1\,\text{m}$ with respect to the center of mass (Smith et al., 2001). The data are provided as a map with horizontal resolution of $\frac{1}{32}^{\circ}$. For the mapping to planetocentric coordinates the IAU2000 reference system was used (Seidelmann et al., 2002). The heights are referenced to the areoid defined by the Goddard Mars potential model GMM3 (mgm1025) evaluated to degree and order 50 (Lemoine et al., 2001). The areoid is precisely defined as "the surface (gravitational plus rotational) whose average value at the equator is equal to the mean radius as determined by MOLA" (Smith et al., 2001).

Here, topography is defined as the height of the surface over a reference equipotential surface, which is the areoid. Shape is defined as the height with respect to the center of mass of Mars. With these definitions, caution should be exercised, because different conventions exist in literature (e.g. Wieczorek and Phillips, 1998). A topography defined with respect to the areoid is relatively meaningless for geophysical analyses (Turcotte et al., 2002) and in this study, the main concern is the shape, and thus the original data set from the PDS Geosciences Node is inconvenient, especially because a different reference radius is used than for the gravity data. Mark Wieczorek provides on his website (http://www.ipgp.fr/~wieczor/SH/SH.html) a processed version of the original data set in which he has converted topography to shape and transformed it to spherical harmonics coefficients to degree and order 2600 (Wieczorek, 2007). This processed data set is used in this study (Figure 2.1).

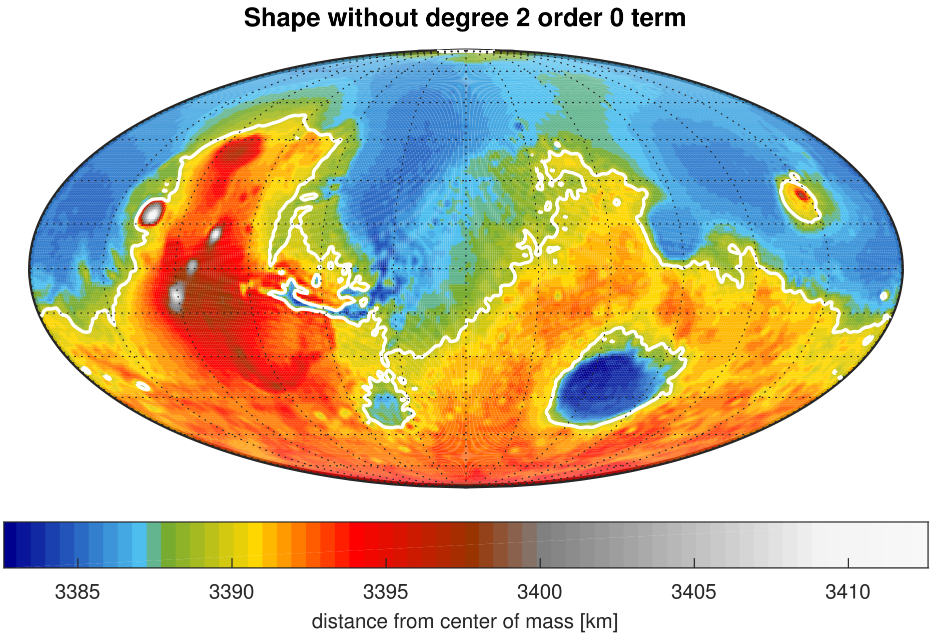

Figure 2.1: The shape of Mars after removing the h_{20} coefficient. The spherical harmonic data set is cut off after degree 110 and transformed into the spatial domain using the algorithm of Driscoll and Healy (1994). The minimum and maximum values plotted are 3382.601 km and 3412.586 km, respectively. The white line is a contour at the level of the mean planetary radius of 3389.500 km and will be shown in all subsequent global maps in this study to provide geographic reference to the reader.

2.2. GRAVITY

Here, the most recent gravity field of Mars from the Jet Propulsion Laboratory (JPL), MRO110C, is used, which is available under `http://pds-geosciences.wustl.edu` (Figure 2.2). Its computation is described in detail in Konopliv et al. (2006) and Konopliv et al. (2011). It includes radio science data from the Mars Global Surveyor (MGS), Mars Odyssey, Mars Reconnaissance Orbiter (MRO), Pathfinder, and Viking 1 Lander missions. The gravity field is provided in fully normalized spherical harmonic coefficients up to degree and order 110 and shows resolution to degree 100 (Figure 2.3, Konopliv et al., 2011). The MGS mission arrived at Mars in 1997 and entered in orbit around Mars, providing gravity solutions which are a drastic improvement over previously available ones because of the uniform global data sets from a low altitude of about 400 km and because it used X-band frequencies rather than the previously used S-band frequencies (Konopliv et al., 2006; Lemoine et al., 2001; Tyler et al., 1992). The arrival of the MRO mission in 2006 again increased the quality of the gravity field because of its lower orbit with a periapse of 255 km (Konopliv et al., 2011). The current gravity field is not expected to improve significantly until new spacecraft orbit Mars, but future data from the MRO and Mars Odyssey missions will yield slight improvements over time (Konopliv et al., 2011).
The gravity field data is provided in the form of normalized spherical harmonic coefficients, or Stokes coefficients, C_{lm}, from which the gravitational potential can be computed as (Hofmann-Wellenhof and Moritz, 2006)

$$U(\boldsymbol{r}) = \frac{GM}{R_g} \sum_{l=0}^{\infty} \sum_{m=-l}^{l} \left(\frac{R_g}{r}\right)^{l+1} C_{lm} Y_{lm}(\Omega) \tag{2.1}$$

where G is the gravitational constant, M is the mass of the planet, l is the degree, m is the order, R_g is the reference radius, Y_{lm} are the spherical harmonics (Equation A.3), $\boldsymbol{r} = (r, \Omega) = (r, \theta, \lambda)$ is the position, θ is the colatitude, λ is the longitude, and r is the distance from the center of mass, which is also the center of the reference system so that the degree one coefficients are zero. The reference radius is $R_g = 3396$ km for the MRO110C gravity field, but $R_g = 3397$ km for the GMM3 (mgm1025) gravity field used to reference the topography to the areoid (Lemoine et al., 2001). In practice, the infinite sum over l in Equation 2.1 is only evaluated to a maximum degree L depending on the data resolution.

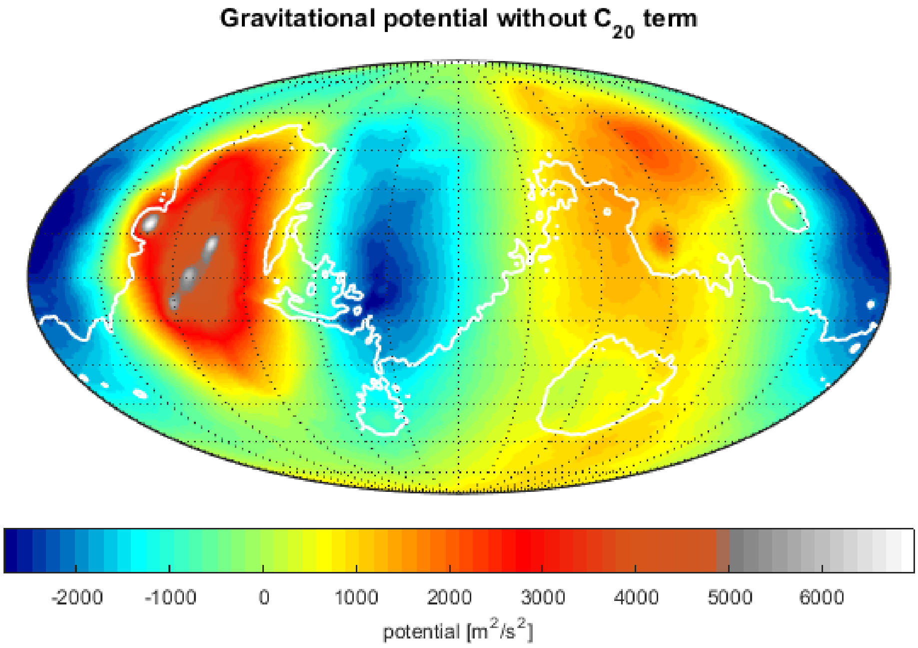

Figure 2.2: The potential of the Mars gravity field MRO110C, evaluated at the mean planetary radius and after removing the C_{20} term. The spherical harmonic data set is transformed into the spatial domain using the algorithm of Driscoll and Healy (1994).

The spherical harmonic degree variance is given by (Neumann et al., 2004)

$$\sigma_l = \sum_{m=-l}^{l} C_{lm}^2 \tag{2.2}$$

and indicates how much of the power is concentrated at which spherical harmonic degrees. The root of the potential power per coefficient is given by (Neumann et al., 2004)

$$\sigma = \frac{\sigma_l}{\sqrt{2l+1}} \tag{2.3}$$

and is usually used to compare gravity field solutions (Figure 2.3).
The gravity anomaly is given by

$$\Delta g = \frac{GM}{R_g^2} \sum_{l=0}^{\infty} (l-1) \sum_{m=-l}^{l} \Delta C_{lm} Y_{lm} \tag{2.4}$$

where

$$\Delta C_{lm} = C_{lm} - C'_{lm}, \tag{2.5}$$

and C'_{lm} are the coefficients of a theoretical ellipsoidal potential V, so that one can define a disturbing potential as (Hofmann-Wellenhof and Moritz, 2006)

$$T = U - V. \tag{2.6}$$

On Earth, the ellipsoidal potential is the potential of an ideal best-fit ellipsoid, and can be computed using the international gravity formula (Hofmann-Wellenhof and Moritz, 2006). On Mars, there is no standard definition of a reference body. A reference ellipsoid is needed to avoid very large areoid values which would otherwise result from the rotational flattening of Mars. The gravity anomaly Δg thus represents deviations of the gravitational attraction from the one caused by such an ideal ellipsoid at the surface of that ellipsoid.
This assumes that all masses are inside of the reference surface and therefore the gravity anomaly is incorrect whenever there is topography which does not coincide with the reference surface. This topography has to

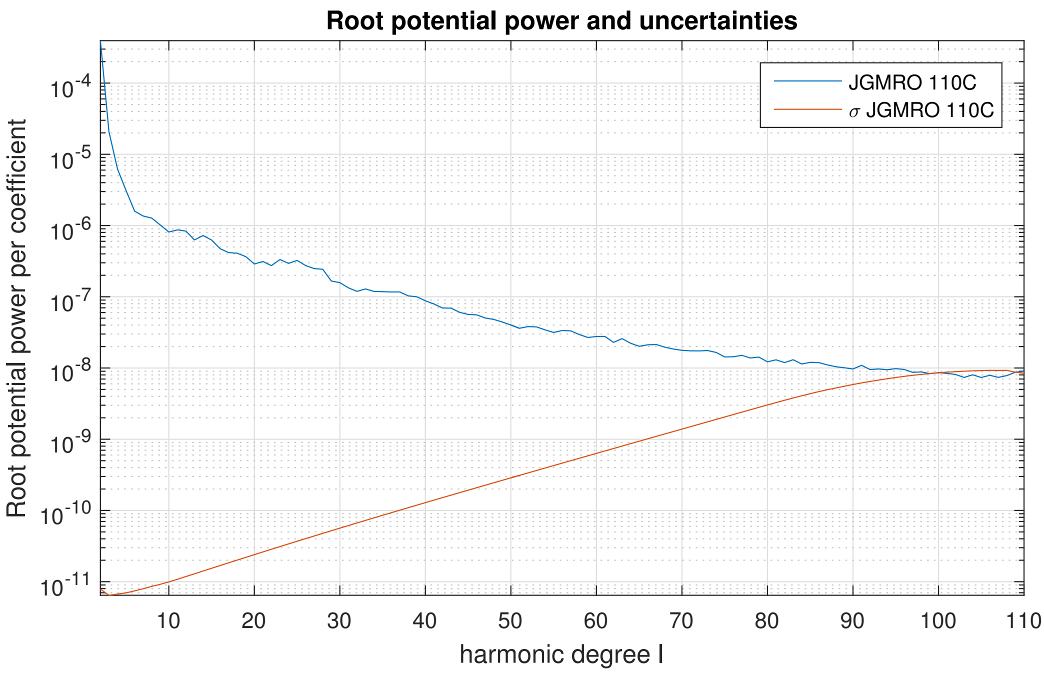

Figure 2.3: The root of the power of the gravity potential and its uncertainties per coefficient.

be corrected for to obtain the Bouguer anomaly, the true gravity anomaly at the reference surface, which can then be used to gain insight into the mass distribution in the inside of the planet, and especially in the crust and upper mantle.

The so-called simple Bouguer anomaly (Hofmann-Wellenhof and Moritz, 2006) corrects for the topography locally. It approximates the gravitational attraction of the topography at position $\boldsymbol{r}$ by the gravitational attraction of a Bouguer plate, that is a plate of infinite lateral extent and thickness h, which is the height of the topography over the reference surface. The Bouguer anomaly is then given by

$$g_B = \Delta g - \Delta g_B \tag{2.7}$$

where

$$\Delta g_B = 2\pi\rho_c G h(\Omega) \tag{2.8}$$

is called the Bouguer correction and ρ_c is the density of the topography which is assumed to be constant and identical to the crustal density. This simple correction model neglects the curvature of the planet and the topography in neighboring areas. It is therefore problematic for small planets like Mars and for areas with large topographic steepness like mountainous regions.

2.2.1. FINITE AMPLITUDE CORRECTION

An exact way of computing the potential caused by topography has been presented by Wieczorek and Phillips (1998). He gives the respective spherical harmonics coefficients as

$$C_{lm}^{\mathrm{BC}} = \frac{4\pi\rho_c(\bar{R}^t)^3}{M(2l+1)} \sum_{n=1}^{l+3} \frac{{}^n h_{lm}}{(\bar{R}^t)^n n!} \frac{\prod_{j=1}^{n}(l+4-j)}{l+3} \tag{2.9}$$

where ${}^n h_{lm}$ are the spherical harmonics coefficients of the n-th power of the shape, which is referenced to the mean planetary radius $\bar{R}^t = h_{00}$, and M is the mass of the planet. Equation 2.9 is called the finite-amplitude correction (McGovern et al., 2002) and is only valid for potential outside of topography, that is $r > \bar{R}^t + \max(h(\Omega))$. In practice, the summation over n can be truncated after a couple of terms and when the required precision is reached to save computation time. The coefficients of the Bouguer anomaly are then given in analogy to Equation 2.7 by

$$C_{lm}^{\mathrm{BA}} = C_{lm} - C_{lm}^{\mathrm{BC}}. \tag{2.10}$$

2.3. OTHER PARAMETERS

For the geophysical model used in this study further data input is required, which is not available in the resolution and quality of the topography and gravity data. Namely, these parameters are the elastic moduli of Mars' lithosphere, as well as the densities of the crust and mantle. This study uses the most common values used in literature to facilitate a comparison of the results. For the elastic moduli, most studies use Poisson's ratio $\nu = 0.25$ and Young's modulus $E = 10^{11}$ Pa (Belleguic et al., 2005; Beuthe et al., 2012; Hoogenboom and Smrekar, 2006; McGovern et al., 2002; Nimmo, 2002; Wieczorek, 2008). McKenzie et al. (2002) and Lowry and Zhong (2003) use significantly different values, which McKenzie et al. (2002) obtained from meteorites, but it is unclear if those meteorites are representative of the present surface of Mars (Neumann et al., 2004), and these values did not prevail in literature.

Zuber et al. (2000) found the crust and mantle density to be $\rho_c = 2900\frac{\mathrm{kg}}{\mathrm{m}^3}$ and $\rho_m = 3500\frac{\mathrm{kg}}{\mathrm{m}^3}$, respectively. These values or very similar ones are widely used (Beuthe et al., 2012; Hoogenboom and Smrekar, 2006; McGovern et al., 2002; Neumann et al., 2004; Wieczorek, 2008) and therefore also applied in this study. A more rigorous approach would of course be the local modelling of the crustal density, as performed by Beuthe et al. (2012), Belleguic et al. (2005), and McKenzie et al. (2002), but this is not done in this study for reasons of complexity, as described in more detail in Chapter 3.

3

Method

This chapter describes the processing steps needed to retrieve the elastic thickness of the lithosphere from the input gravity and topography data described in Chapter 2. At first, the global input data must be localized in order to receive outputs for one specific location and not a global value for the whole planet. For this localization, the multitaper spectral estimation technique is used, which is presented in Section 3.1. The core of this chapter is formed by Section 3.2, in which the geophysical model relating localized input and output variables is described. Section 3.3 treats maximum likelihood estimation, the method for finding the set of output parameters which is most likely to have produced the observations. Finally, Section 3.4 describes how the uncertainty of the results can be quantified using Monte Carlo simulations. The data processing scheme is also summarized in Figure 3.5, and Table C.1 gives an overview of all symbols and quantities used in this study.

3.1. Multitaper spectral estimation

The ultimate goal of this study is the creation of a global map of the elastic thickness of Mars. For this purpose, T_e is computed on a regular grid of locations (see Section 4.3). The data fields and their spectral estimates must therefore be localized to each of those grid points. The multiplication of window functions with the data fields in the spatial domain is called tapering. The windows are selected such that only data from an area around the location of interest are used for the estimation at that location while spectral leakage is minimized. In this section, the multitaper spectral estimation procedure developed by Wieczorek and Simons (2005) is presented.

Ideally, one would like to include all data from an area around the location of interest into the estimation and not include any data from outside of that area, or, in other words, one would like to apply a sharply truncated window. Here, a spherical cap is used as a window. Assuming that the location of interest is the north pole, then the sharply truncated spherical cap window includes all information up to a colatitude θ_0, and discards all other information. The window can then simply be rotated to any arbitrary desired location. Here, I restrict myself to axisymmetric windows because I assume isotropy in the whole model. The estimated spectra are only a function of the spherical harmonic degree l, and not of the order m. To estimate anisotropy, non-axisymmetric windows would be required.

When using sharply truncated windows, the phenomenon of spectral leakage occurs. Therefore, bandlimited windows are used which possess no power outside of a certain spectral bandwidth and are optimally concentrated in the spatial domain. The quality of the spatial concentration is measured by a parameter

$$c = \frac{\int_0^{2\pi} \int_0^{\theta_0} H^2(\Omega) \sin\theta \, \mathrm{d}\theta \, \mathrm{d}\lambda}{\int_0^{2\pi} \int_0^{\pi} H^2(\Omega) \sin\theta \, \mathrm{d}\theta \, \mathrm{d}\lambda} \tag{3.1}$$

which represents the ratio of the energy of the bandlimited taper $H(\Omega)$ in the spherical cap region $0 < \theta < \theta_0$ to the energy of $H(\Omega)$ over the whole sphere.

With Equation A.1 the filter functions can be expanded into spherical harmonics

$$H(\Omega) = \sum_{l=0}^{\infty} \sum_{m=-l}^{l} H_{lm} Y_{lm}(\Omega)\,, \tag{3.2}$$

but in practice, one can only expand the filter into spherical harmonic coefficients up to a certain degree L_b, so that

$$H(\Omega) = \sum_{l=0}^{L_b} \sum_{m=-l}^{l} H_{lm} Y_{lm}(\Omega)\,, \tag{3.3}$$

and since the taper is axisymmetric, this simplifies to

$$H(\Omega) = H(\theta) = \sum_{l=0}^{L_b} H_l Y_{l0}(\Omega) = \sum_{l=0}^{L_b} H_l \bar{P}_{l0}(\cos\theta)\,. \tag{3.4}$$

Applying Parsival's theorem (Equation A.8) and Equation 3.4 to Equation 3.1, the energy ratio can be written as

$$c = \frac{\sum_{l=0}^{L_b} \sum_{l'=0}^{L_b} H_l D_{ll'}(\theta_0) H_{l'}}{\sum_{l=0}^{L_b} H_l^2} \tag{3.5}$$

where

$$D_{ll'}(\theta_0) = \frac{1}{2} \int_{\cos\theta_0}^{1} \bar{P}_l(\cos\theta)\bar{P}_{l'}(\cos\theta)\,\mathrm{d}\cos\theta\,. \tag{3.6}$$

Equation 3.5 can be written in matrix form as

$$c = \frac{\boldsymbol{H}^\top \boldsymbol{D} \boldsymbol{H}}{\boldsymbol{H}^\top \boldsymbol{H}} \tag{3.7}$$

where $\boldsymbol{H}$ is the (L_b+1)-vector of filter coefficients H_l and $\boldsymbol{D}$ is the $(L_b+1)\times(L_b+1)$-matrix defined by Equation 3.6. Equation 3.7 has the same solutions of c as the eigenvalue problem

$$c\boldsymbol{H} = \boldsymbol{D}\boldsymbol{H}\,. \tag{3.8}$$

The L_b+1 orthogonal eigenvectors $\boldsymbol{H}_i$ therefore each form the filter coefficients of a filter with their energy ratio given by the corresponding eigenvalue c_i. The order of the eigenvalues is defined as

$$1 > c_1 > c_2 > \ldots > c_{L_b+1} > 0 \tag{3.9}$$

so that $\boldsymbol{H}_1$ is the filter with the best spatial concentration. Wieczorek and Simons (2005) showed that there is a sharp transition between eigenvalues that are close to one and eigenvalues that are almost zero. The eigenvectors whose corresponding eigenvalues are close to one are near-perfectly concentrated tapers. Wieczorek and Simons (2005) defined a space-bandwidth product

$$N_0 = (L_b+1)\frac{\theta_0}{\pi} \tag{3.10}$$

which is an important quantity in practice because the first N_0-1 tapers are near-perfectly concentrated. Windowing a function using the first $K = N_0-1$ tapers and then taking the weighted average is statistically more representative than windowing the function with only one taper. Here, I take the simple average of the first $K = N_0-1$ tapers because all of them are near-perfectly concentrated. This average is called the localized multitaper spectral estimate and it is asymptotically unbiased for an increasing number of tapers. Therefore, a large number of tapers is desired. However, Equation 3.10 shows that there is a trade-off between the window size and the bandwidth one the one hand, which are preferably kept small, and the number of applied tapers on the other hand.

When applying the tapers to a spherical harmonic gravity or topography field which is determined up to degree L, only the degrees $L_b < l < L-L_b$ can be determined reliably which puts serious restrictions on the window size and number of tapers that can be used for the spherical harmonic fields of degree $L=110$ which are used in this study. Furthermore, the Martian gravity and topography fields are globally influenced by the signature of the Tharsis region and its flexure up to degree $L=5$, and the gravity field only shows resolution up to degree $L\approx 100$. These low and high degrees must be removed before an analysis can take

place (Wieczorek and Zuber, 2004), so that the remaining degrees used for the elastic thickness estimation are $L_b + 5 < l < 100 - L_b$. As an example, for a spherical cap size of $\theta_0 = 15°$ and using $K = 2$ tapers, the bandwidth is $L_b = 35$, and only the spherical harmonic degrees $40 < l < 65$ can be used.
In this study, the freely available software package SHTOOLS (Wieczorek et al., 2015) is used in which multi-taper spectral estimation is implemented. From a choice of two of the three parameters N_0, L_b, and θ_0 from Equation 3.10, the third parameter can be determined. Then, with θ_0, the components of the matrix $\boldsymbol{D}$ (Equation 3.6) are computed, and the eigenvalue problem (Equation 3.8) is solved for $L_b + 1$ eigenvalues. These two processing steps are implemented in computationally efficient ways which are not presented here. The K optimally concentrated filters are then rotated to the point of interest using a standard algorithm and expanded into the spatial domain, where they can be multiplied with the data field. The windowed data fields are then expanded back into the spherical harmonic domain and the spectral estimates are averaged.

3.2. GEOPHYSICAL MODEL

In this section, a geophysical model is developed which relates the input variables topography and gravity to the elastic thickness of the lithosphere. It is necessary to use a thin shell model because Mars is too small to neglect the role of membrane stresses in lithospheric modelling (Turcotte et al., 1981). There is currently no thin elastic shell model available which incorporates the effect of anisotropy, which is therefore neglected (Audet, 2011; Simons and Olhede, 2013). This section presents a model which has previously been described by other authors in the Cartesian domain and by Audet (2014) in the spherical domain. Most derivations in this section are therefore also given in similar form in Audet (2014) and Simons and Olhede (2013).

3.2.1. FLEXURE

The equation for the flexure of a thin, isotropic shell is (Beuthe, 2008)

$$\left(D\nabla^2 \left(\nabla^2\right)' \left(\nabla^2\right)' + (\bar{R}^t)^2 E T_e \left(\nabla^2\right)'\right) u(\boldsymbol{r}) = -(\bar{R}^t)^4 \left(\left(\nabla^2\right)' - 1 - \nu\right) q(\boldsymbol{r}) \tag{3.11}$$

where $\bar{R}^t$ is the radius of the shell, $u(\boldsymbol{r})$ is the deflection at position $\boldsymbol{r}$ measured positive upwards, and $q(\boldsymbol{r})$ is the loading pressure at position $\boldsymbol{r}$ measured positive downwards (Figure 3.1). For a definition of the differential operators ∇^2 and $\left(\nabla^2\right)'$ see Appendix B. Note that Equation 3.11 is also given in McGovern et al. (2002), but incorrectly attributed to both load and deflection pointing in the same direction, contrary to the definition in Beuthe (2008), Turcotte et al. (1981), and this study. Note also that Turcotte et al. (1981) and after them many other studies (e.g. McGovern et al., 2002) used a slightly erroneous version of Equation 3.11 which includes the term $D(\nabla^6 + 4\nabla^2)$ instead of $D\nabla^2 \left(\nabla^2\right)' \left(\nabla^2\right)'$. However, this only has significant impacts on the degree one term, and therefore did not affect elastic thickness estimates for which the higher degrees are relevant.

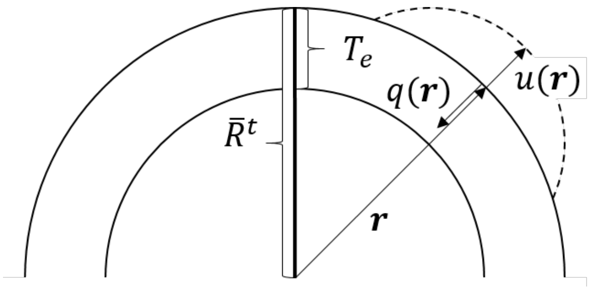

Figure 3.1: Thin elastic shell for $T_e \ll \bar{R}^t$. When a load is applied at position $\boldsymbol{r}$, the deflection $u(\boldsymbol{r})$ causes a loading pressure $q(\boldsymbol{r})$.

Transforming Equation 3.11 into the spherical harmonic domain and inserting Equation 1.1 gives

$$\left(\frac{E T_e^3}{12(1-\nu^2)}\left(-l^3(l+1)^3 + 4l^2(l+1)^2 - 4l(l+1)\right) + (\bar{R}^t)^2 E T_e(-l(l+1)+2)\right) u_{lm} = -(\bar{R}^t)^4(-l(l+1)+1-\nu) q_{lm}, \tag{3.12}$$

where u_{lm} and q_{lm} are the spherical harmonics coefficients of $u(\boldsymbol{r})$ and $q(\boldsymbol{r})$, respectively (Equation A.1). Defining the flexural parameters

$$\xi = \frac{ET_e^3}{12(\bar{R}^t)^4(1-\nu^2)} \tag{3.13a}$$

$$\tau = \frac{ET_e}{(\bar{R}^t)^2} \tag{3.13b}$$

and

$$f_1 = -l^3(l+1)^3 + 4l^2(l+1)^2 - 4l(l+1) \tag{3.14a}$$

$$f_2 = -l(l+1) + 2 \tag{3.14b}$$

$$f_3 = -(-l(l+1) + 1 - \nu)\,, \tag{3.14c}$$

Equation 3.12 can be written as

$$(\xi f_1 + \tau f_2)u = f_3 q \tag{3.15}$$

where the subscript lm was omitted for simplicity and because all further treatment will be in the spherical harmonic domain.

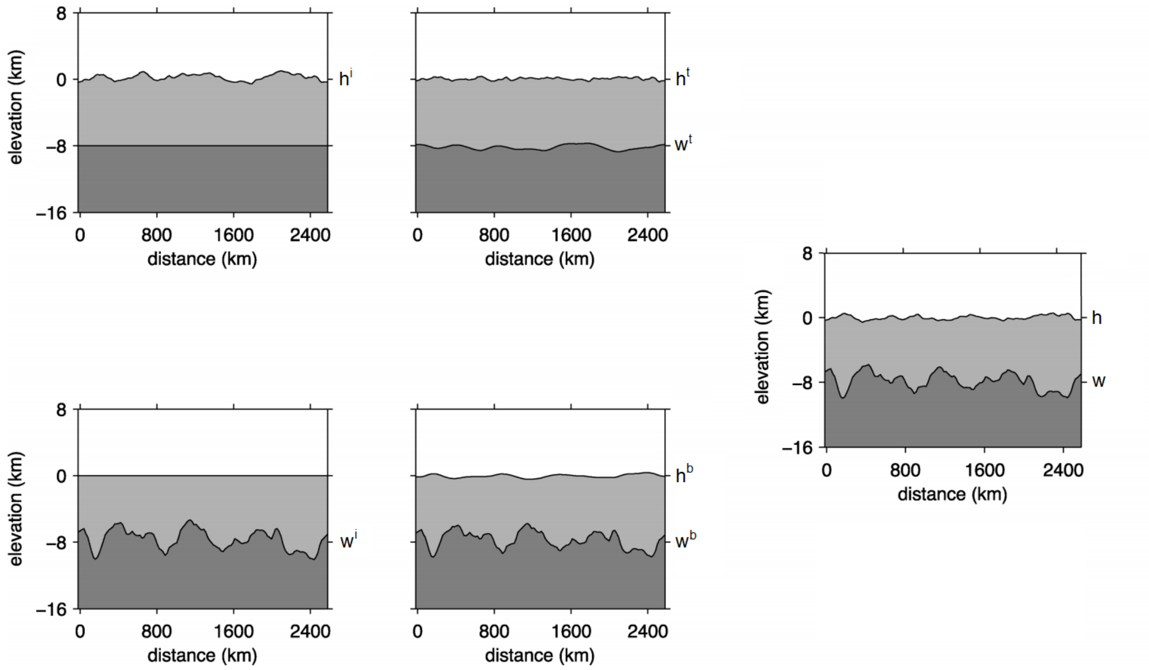

Figure 3.2: An initial surface topography h^i causes a subsurface deflection w^t and an equilibrium surface topography h^t (top left and middle). An initial subsurface topography w^i causes a surface deflection h^b and an equilibrium subsurface topography w^b (bottom left and middle). Note the smoothing effect of the upward and downward continuations. Surface and subsurface quantities from both sources are summed up to yield the final (observable) surface and subsurface topographies h and w (right). This figure is adapted from Simons and Olhede (2013) who simulated the values with the Matérn covariance function.

The model incorporates two density interfaces: the surface with a density contrast equal to the crustal density ρ_c, assuming the atmosphere a zero-density fluid; and the crust-mantle boundary with a density contrast $\Delta\rho = \rho_m - \rho_c$ where ρ_m is the mantle density. Loads can be emplaced on either or both of those density interfaces as undulations of their topography and cause, by compensation, a deflection of the respective other interface (Figure 3.2). Here, topography means a small deviation from an interface and generally refers to any surface or subsurface interface.

This model is a very simple approximation to reality. Other studies have used more than two density interfaces (Belleguic et al., 2005; McKenzie, 2003) and load densities that differ from crust and mantle densities (Belleguic et al., 2005; Beuthe et al., 2012; McGovern et al., 2002). The realistic modelling of phenomena like mantle plumes and high density intrusions requires such different load densities (Beuthe et al., 2012). Belleguic et al. (2005) also applied the loads and the compensation at different interfaces, whereas this study uses the assumption that the depth of loading and the depth of compensation are identical (Forsyth, 1985). All of these variations are trade-offs between keeping the model simple and making it more realistic, and come with additional unknown parameters that must be estimated, such as top and bottom load densities and the depths of the various interfaces. In this study, the model is kept as simple as possible while remaining realistic (Simons and Olhede, 2013), to keep the parameter optimization process feasible and to demonstrate the general applicability of the method.

3.2.2. SURFACE LOADING

For surface loads Equation 3.15 can be written as

$$(\xi f_1 + \tau f_2) w^t = f_3 q^t . \tag{3.16}$$

where q^t is the surface (top) loading pressure and w^t is the subsurface deflection caused by it. One contribution to the pressure is the weight of the load $g\rho_c h^t$ where g is the gravitational attraction and h^t is the surface topography in an equilibrium state which is reached after the initial load has been compensated. This weight also causes a downward displacement of the shell. Therefore, the crust-mantle boundary with density contrast $\Delta\rho$ generates an upward pressure $g\Delta\rho w^t$. This gives the equation

$$q^t = g\rho_c h^t + g\Delta\rho w^t \tag{3.17}$$

which assumes a homogeneous density structure both in lateral direction and within the two layers, a constant gravitational attraction,

$$g = \frac{GM}{(\bar{R}^t)^2}, \tag{3.18}$$

at the level of the mean planetary radius throughout the crust, and an unperturbed equipotential surface at the crust-mantle boundary (Belleguic et al., 2005). All these assumptions are critical for very large loads, as found for example in the Tharsis region, but cannot be implemented without using a much more complex model.

Inserting Equation 3.17 into Equation 3.16 gives

$$(\xi f_1 + \tau f_2) w^t = f_3 (g\rho_c h^t + g\Delta\rho w^t) \tag{3.19}$$

$$\Leftrightarrow w^t = \frac{\rho_c}{\Delta\rho} \frac{f_3}{\frac{\xi f_1}{g\Delta\rho} + \frac{\tau f_2}{g\Delta\rho} - f_3} h^t , \tag{3.20}$$

or

$$w^t = \alpha^t h^t , \tag{3.21}$$

where

$$\alpha^t = \frac{\rho_c}{\Delta\rho} \frac{f_3}{\frac{\xi f_1}{g\Delta\rho} + \frac{\tau f_2}{g\Delta\rho} - f_3} \tag{3.22}$$

can be regarded as the flexural filter of top loading.

3.2.3. SUBSURFACE LOADING

Processes which can cause density anomalies in the subsurface include igneous intrusions and magma chambers (Beuthe et al., 2012; Watts and Burov, 2003). Subsurface density anomalies caused by impact cratering are called mascons and rifting processes in Valles Marineris can cause crustal thinning (McGovern et al., 2002). For such subsurface loads Equation 3.15 can be written as

$$(\xi f_1 + \tau f_2) h^b = f_3 q^b . \tag{3.23}$$

where q^b is the subsurface (bottom) loading pressure and h^b is the surface deflection caused by it. Analogy to top loading gives the equation

$$q^b = g\Delta\rho w^b + g\rho_c h^b \tag{3.24}$$

which again underlies several assumptions and where w^b is the equilibrium subsurface topography. Inserting Equation 3.24 into Equation 3.23 gives

$$(\xi f_1 + \tau f_2)h^b = f_3(g\Delta\rho w^b + g\rho_c h^b) \tag{3.25}$$

$$\Leftrightarrow w^b = \frac{\rho_c}{\Delta\rho}\frac{\frac{\xi f_1}{g\rho_c} + \frac{\tau f_2}{g\rho_c} - f_3}{f_3}h^b, \tag{3.26}$$

or

$$w^b = \alpha^b h^b, \tag{3.27}$$

where

$$\alpha^b = \frac{\rho_c}{\Delta\rho}\frac{\frac{\xi f_1}{g\rho_c} + \frac{\tau f_2}{g\rho_c} - f_3}{f_3} \tag{3.28}$$

can be regarded as the flexural filter of bottom loading.
Note that in the derivations of Equations 3.22 and 3.28 of Audet (2014) there are several typos, but his final results for the flexural filters (his Equations B13 and B19) are nonetheless correct and identical to mine.

3.2.4. SUBSURFACE TOPOGRAPHY

For the geophysical model used in this study it is essential to know the subsurface topography. The only available data to probe the subsurface is the gravity, specifically the Bouguer anomaly which by design gives information only about the subsurface and not about the surface topography. Here it is assumed that the Bouguer anomaly is caused by subsurface topography on only one density interface which is the crust-mantle boundary. This means that the crust and mantle are both assumed to be completely homogeneous and the density anomalies resulting from all crust and mantle processes are merged into one density anomaly which is the bottom load and causes the Bouguer anomaly. Specifically, the higher density of the Tharsis volcanoes (McGovern et al., 2002), the lower density of the polar caps, and the effect of the hydrostatic flattening of the core-mantle boundary (Neumann et al., 2004) are known to cause deviations of the Bouguer anomaly from the homogeneous case. To unambiguously determine the subsurface topography using this method, the depth of the subsurface interface must be set to a fixed value at one location on Mars. Since, unlike for the Moon, there is no data available for such a constraint on Mars, I follow Zuber et al. (2000) and arbitrarily set the global minimum crustal thickness, which is located in the Isidis crater, to 3 km. It is in fact possible that the crustal thickness in Isidis is much larger (Wieczorek and Zuber, 2004), but the impact of this uncertainty is probably small for the estimation of the elastic thickness (Belleguic et al., 2005). Again, a more realistic model, including more density interfaces or a more complicated density structure, is renounced in favor of a simpler model. This approach is justified with the limited data situation on Mars (no interior structure through seismology) and the complexity of the parameter optimization.
The process of deriving subsurface gravity from surface gravity is called downward continuation (Blakely, 1996). Since the potential field becomes smoother with increasing distance, the input to the downward continuation is smoother than the output which causes the process to be unstable and to amplify noise (Blakely, 1996; Wieczorek and Phillips, 1998). In a wider sense, the term downward continuation is also used for the derivation of subsurface topography from surface gravity, thereby including the transition from subsurface gravity to subsurface topography. A simple downward continuation filter uses the Bouguer plate approximation (Section 2.2), but Wieczorek and Phillips (1998) provided a more robust approach by minimizing the relief along the subsurface interface. They give the subsurface topography as

$$w_{lm} = \chi_l \left(\frac{C^{\mathrm{BA}}_{lm} M(2l+1)}{4\pi\Delta\rho(\bar{R}^b)^2}\left(\frac{\bar{R}^t}{\bar{R}^b}\right)^l - \bar{R}^b \sum_{n=2}^{l+3} \frac{{}^n w_{lm}}{(\bar{R}^b)^n n!}\frac{\prod_{j=1}^{n}(l+4-j)}{l+3}\right) \tag{3.29}$$

where

$$\chi_l = \left(1 + \lambda\left(\frac{M(2l+1)}{4\pi\Delta\rho(\bar{R}^b)^2}\left(\frac{\bar{R}^t}{\bar{R}^b}\right)^l\right)^2\right)^{-1} \tag{3.30}$$

is the downward continuation filter, $\bar{R}^b$ is the mean radius of the subsurface interface, and λ is a Lagrange multiplier, which is in practice chosen so that $\chi_l = \frac{1}{2}$ for the maximum degree at which the potential spectrum shows resolution (Wieczorek and Phillips, 1998).

Equation 3.29 can be evaluated iteratively. An initial guess of the subsurface topography, which is related to the crustal thickness T_c by $w(\boldsymbol{r}) = \bar{R}^t - T_c(\boldsymbol{r})$ and referenced to the center of mass, is given in the spatial domain, for example a constant value for the whole planet. This field is then expanded to the n-th power for all $n < n_{\max}$. Evaluating the sum in Equation 3.29 until $l+3$ would be computationally expensive, but Wieczorek and Phillips (1998) found that for $n_{\max} = 5$ the resolution is sufficient. All the powers of the topography are then transformed into the spectral domain using a spherical harmonics analysis algorithm (Driscoll and Healy, 1994). The mean value of the subsurface topography is given as

$$\bar{R}^b = {}^1w_{00}\,. \tag{3.31}$$

The coefficients w_{lm} resulting this way from Equation 3.29 are then transformed back into the spatial domain by a spherical harmonics synthesis algorithm and used as the intitial values for the next iteration. In practice,

$$w^3_{lm} = \frac{1}{2}(w^1_{lm} + w^2_{lm}) \tag{3.32}$$

is used as the initial value for the third iteration to achieve increased stability (Wieczorek et al., 2015). The iteration is continued until convergence is reached.

3.2.5. COMBINED LOADING

The top and bottom loading processes are combined by superposition. This gives the final surface and subsurface topographies

$$h = h^t + h^b \tag{3.33}$$

$$w = w^t + w^b\,. \tag{3.34}$$

These are the observables of the model. h is observed directly and w is computed from the Bouguer anomalies. To the initial topographies, isostatic compensation applies (Watts, 2001). Surface heights are causing subsurface deflection and vice versa:

$$h^i = h^t - w^t \tag{3.35}$$

$$w^i = w^b - h^b\,. \tag{3.36}$$

Combining Equations 3.35 and 3.36 with Equation 3.33 gives

$$h = \frac{h^i h^t}{h^t - w^t} + \frac{w^i h^b}{w^b - h^b} = \frac{h^i}{1 - \frac{w^t}{h^t}} + \frac{w^i}{\frac{w^b}{h^b} - 1} \tag{3.37}$$

and combining Equations 3.35 and 3.36 with Equation 3.34 gives

$$w = \frac{h^i w^t}{h^t - w^t} + \frac{w^i w^b}{w^b - h^b} = \frac{h^i}{\frac{h^t}{w^t} - 1} + \frac{w^i}{1 - \frac{h^b}{w^b}}\,. \tag{3.38}$$

Inserting the loading filters (Equations 3.21 and 3.27) into Equations 3.37 and 3.38 gives

$$h = \frac{h^i}{1-\alpha^t} + \frac{w^i}{\alpha^b - 1} \tag{3.39}$$

$$w = \frac{\alpha^t h^i}{1-\alpha^t} + \frac{\alpha^b w^i}{\alpha^b - 1}\,, \tag{3.40}$$

or, in matrix notation

$$\begin{pmatrix} h \\ w \end{pmatrix} = \begin{pmatrix} (1-\alpha^t)^{-1} & (\alpha^b - 1)^{-1} \\ \alpha^t(1-\alpha^t)^{-1} & \alpha^b(\alpha^b-1)^{-1} \end{pmatrix} \begin{pmatrix} h^i \\ w^i \end{pmatrix} \tag{3.41}$$

Equations 3.41 are called the load deconvolution equations (Forsyth, 1985; Lowry and Smith, 1994) and can also be written as

$$\boldsymbol{h} = \boldsymbol{M}_{T_e} \boldsymbol{h}^i \tag{3.42}$$

where the matrix $\boldsymbol{M}_{T_e}$ contains all information about the geophysical model and depends only on the elastic thickness T_e.

3.2.6. INITIAL LOADS

When studying planetary gravity and topography, one has to distinguish between the random processes gravity and topography, and their realizations. Here, the fact that the subsurface topography is a derived quantity is ignored, and it is treated as a random process in its own right. For the spherical harmonics expansion of two zero mean random processes of topographies h_{lm} and w_{lm} one can write the spectral cross-covariance as a function of degree l as (Wieczorek and Simons, 2005)

$$S_{hw}(l) = \sum_{m=-l}^{l} h_{lm} w_{lm} . \tag{3.43}$$

The spectral cross-covariance matrix of final topographies is then given by

$$\boldsymbol{S_{hh}}(l) = \begin{pmatrix} S_{hh}(l) & S_{hw}(l) \\ S_{wh}(l) & S_{ww}(l) \end{pmatrix} . \tag{3.44}$$

Only one realization of the random processes of surface and subsurface topography can be observed, and this realization is blurred by a localization window as described in Section 3.1. The blurred spectral covariance is computed from this blurred realization of the random process topography and denoted as $\boldsymbol{\bar{S}_{hh}}(l)$.
The cross-covariance matrix of initial topographies is given by

$$\boldsymbol{S_{h^i h^i}}(l) = \begin{pmatrix} S_{h^i h^i}(l) & S_{h^i w^i}(l) \\ S_{w^i h^i}(l) & S_{w^i w^i}(l) \end{pmatrix} . \tag{3.45}$$

Then, applying error propagation to Equation 3.42, one can write

$$\boldsymbol{S_{hh}}(l) = \boldsymbol{M}_{T_e}(l) \boldsymbol{S_{h^i h^i}}(l) \boldsymbol{M}_{T_e}^{\top}(l) . \tag{3.46}$$

So, with knowledge of the geophysical model $\boldsymbol{M}_{T_e}$ and the covariance spectrum of the random process of initial topographies $\boldsymbol{S_{h^i h^i}}$, one can deduce the covariance spectrum of the random process of final topographies $\boldsymbol{S_{hh}}$, which will, after blurring, enter the objective function of the maximum likelihood estimation as $\boldsymbol{\bar{S}_{hh}}$ (see Section 3.3.2).
The goal is now to eliminate three of the four components of $\boldsymbol{S_{h^i h^i}}(l)$ by the assumptions of load correlation and load proportionality. First, note that because of isotropy

$$S_{h^i w^i}(l) = S_{w^i h^i}(l) . \tag{3.47}$$

Then, the coefficient

$$r = \frac{S_{h^i w^i}(l)}{\sqrt{S_{h^i h^i}(l) S_{w^i w^i}(l)}} \tag{3.48}$$

is introduced, which gives the correlation between the initial topographies, so that the covariance matrix (Equation 3.45) can be written as

$$\boldsymbol{S_{h^i h^i}}(l) = \begin{pmatrix} S_{h^i h^i}(l) & r\sqrt{S_{h^i h^i}(l) S_{w^i w^i}(l)} \\ r\sqrt{S_{h^i h^i}(l) S_{w^i w^i}(l)} & S_{w^i w^i}(l) \end{pmatrix} , \tag{3.49}$$

thereby eliminating the cross-covariance terms. In studies investigating the Earth's elastic thickness, the initial loads have often been assumed to be uncorrelated (e.g. Forsyth, 1985), which corresponds to a load correlation $r = 0$. In contrast, McGovern et al. (2002) assumed perfect correlation $r = 1$ for Mars' lithosphere. Recently, several studies have pointed out that the assumption of either perfectly correlated or perfectly uncorrelated initial loads can be a severe limitation for the correct estimation of the elastic thickness (Audet, 2014; Kirby and Swain, 2009; Simons and Olhede, 2013). Therefore, the load correlation is here estimated as an independent parameter together with the elastic thickness. However, it is assumed constant over all spherical harmonic degrees, to keep the number of parameters in the estimation at a minimum.
The bottom and top loads L^b and L^t are essentially pressures acting on the respective interfaces and resulting from the weight of the topography:

$$L^t = g\rho_c h^i \tag{3.50a}$$

$$L^b = g\Delta\rho w^i . \tag{3.50b}$$

A spherical harmonics equivalent of the loading fraction f^2 (Equation 1.6) defined by Forsyth (1985) the in the Fourier domain is

$$f^2(l) = \frac{\sum_{m=-l}^{l} L^b_{lm} L^b_{lm}}{\sum_{m=-l}^{l} L^t_{lm} L^t_{lm}} \tag{3.51}$$

which, using Equations 3.43 and 3.50, can be written as

$$f^2(l) = \frac{\Delta\rho^2 S_{w^i w^i}(l)}{\rho_c^2 S_{h^i h^i}(l)}. \tag{3.52}$$

The loading fraction can be used to eliminate the third component from the covariance matrix of initial loads (Equation 3.45) by writing

$$\boldsymbol{S}_{\boldsymbol{h}^i\boldsymbol{h}^i}(l) = S_{h^i h^i}(l) \begin{pmatrix} 1 & rf\frac{\rho_c}{\Delta\rho} \\ rf\frac{\rho_c}{\Delta\rho} & f^2\frac{\rho_c^2}{\Delta\rho^2} \end{pmatrix}. \tag{3.53}$$

By the assumption of such a loading fraction, the loads become proportional. Again, this study estimates the loading fraction as an independent parameter, but treats it as constant over all spherical harmonic degrees to keep the number of parameters small.
At this point it is worth to take a look back at the standard spectral estimation procedure for the elastic thickness in literature (e.g. Audet, 2014; Forsyth, 1985; Kirby and Swain, 2009; McGovern et al., 2002; McKenzie, 2003). Writing the spherical harmonics equivalent (Wieczorek and Simons, 2005) of the admittance and coherence (Equations 1.3 and 1.4) as

$$\bar{q}_l = \frac{S_{hg}(l)}{S_{hh}(l)} \tag{3.54}$$

$$\gamma_l^2 = \frac{S_{hg}^2(l)}{S_{hh}(l)S_{gg}(l)} \tag{3.55}$$

one can see that explicit expressions would become very complicated when considering the propagation from initial to final quantities (Equation 3.46). The final quantities are given for the much simpler planar case by Kirby and Swain (2009) and Simons and Olhede (2013) and show strong nonlinearity in all three parameters T_e, F, and r. McKenzie (2003) plotted misfit surfaces for the admittance as a function of T_e and f^2 which illustrate the ambiguity in the estimated results and McKenzie (2015) emphasized that in regions of incoherent gravity and topography both spectral ratios cannot estimate the elastic thickness, and instead provide over-estimates. By studying the admittance or coherence, one essentially takes ratios of elements of the matrix $\boldsymbol{S}_{\boldsymbol{hh}}$ which have unknown statistical distributions, and uses them to invert for the elastic thickness, whose statistics are therefore also unknown.

3.3. MAXIMUM LIKELIHOOD ESTIMATION

This study abstains from using admittance and coherence because of the aforementioned complications. Least-squares estimation is not a flexible estimation method because it always requires a normal distribution of the data that are supposed to be fit, which is not the case for admittance and coherence. Instead, in this study I apply an approach which is new to the field of elastic thickness estimation and uses maximum likelihood estimation. It has been proposed and tested on synthetic data by Simons and Olhede (2013). For maximum likelihood estimation, a statistical distribution of the input data must be assumed, but here, I invert for the parameters of that distribution, and thereby determine the statistical distribution in the same inversion process in which I also determine the geophysical parameters T_e, F, and r.

3.3.1. SPECTRAL COVARIANCE OF THE INITIAL TOPOGRAPHIES

The geophysical model depends on the parameter T_e, which is to be estimated, and the constants ρ_c, $\Delta\rho$, E, ν, g, and R. It is connected to the spectral representation of the unknown initial topographies $S_{h^i h^i}$ by load proportionality and load correlation. These concepts are represented by the parameters F and r which are also to be estimated. Here, in accordance to Simons and Olhede (2013), the Matérn isotropic class is used to parameterize the covariance of the initial topographies. The Matérn class of covariance functions has been introduced in the spatial domain as

$$M(||\boldsymbol{d}||) = \mathrm{Cov}(f(\boldsymbol{r}), f(\boldsymbol{r}+\boldsymbol{d})) = \frac{\sigma^2 2^{1-\nu}}{\Gamma(\nu)}(\alpha||\boldsymbol{d}||)^{\nu}\mathcal{K}_{\nu}(\alpha||\boldsymbol{d}||) \tag{3.56}$$

by Matérn (1960) and popularized by Handcock and Stein (1993). In Equation 3.56, $\sigma^2 > 0$ is the variance, $\alpha > 0$ is the scale parameter, $\nu > 0$ is the smoothness parameter (Guttorp and Gneiting, 2006), $\Gamma(x)$ is the gamma function,

$$\mathcal{K}_{\nu}(x) = \frac{\pi(\mathcal{I}_{-\nu}(x) - \mathcal{I}_{\nu}(x))}{2\sin(\nu\pi)} \tag{3.57}$$

is the modified Bessel function of the second kind, and

$$\mathcal{I}_{\nu}(x) = \sum_{m=0}^{\infty} \frac{1}{m!\Gamma(m+\nu+1)}\left(\frac{x}{2}\right)^{2m+\nu} \tag{3.58}$$

is the modified Bessel function of the first kind (Abramowitz and Stegun, 1964). The covariance M is isotropic because its value does not depend on the two points $\boldsymbol{r}$ and $\boldsymbol{r}+\boldsymbol{d}$, but only on the distance $||\boldsymbol{d}||$ between them (Stein, 1999). M will become smoother for increasing ν. Other covariance functions, like for example the spherical, the exponential, and the Gaussian covariance, do not have such a smoothness parameter. Therefore, they are not flexible enough to predict the local behavior which is typical for geo-spatial data (Stein, 1999). They may be able to model processes with known smoothness well, but usually, and so also in the case of planetary topography, the smoothness is not known in advance. Note also that the Gaussian covariance function is a liming case of the Matérn covariance for $\nu \to \infty$, and the exponential covariance function is a special case for $\nu = \frac{1}{2}$ (Guttorp and Gneiting, 2006). In fact, all functions of the type

$$M(||\boldsymbol{d}||) = \sigma^2(\alpha||\boldsymbol{d}||)^{\nu}\mathcal{K}_{\nu}(\alpha||\boldsymbol{d}||) \tag{3.59}$$

are valid isotropic covariance functions, even after dropping the term $(2^{\nu-1}\Gamma(\nu))^{-1}$ from Equation 3.56 (Stein, 1999). This term normalises the covariance so that $M(||\boldsymbol{d}||) \to \sigma^2$ for $x \to 0$, which gives the term σ^2 its practical interpretation as the variance.
Gneiting et al. (2013) showed that the Matérn covariance function can be expressed on the sphere as

$$M(\psi) = \frac{\sigma^2 2^{1-\nu}}{\Gamma(\nu)}\left(\alpha\psi\right)^{\nu}\mathcal{K}_{\nu}\left(\alpha\psi\right) \tag{3.60}$$

for great circle distances $\psi \in [0,\pi]$, $\sigma^2 > 0$, and $\alpha > 0$, and $0 < \nu \leq \frac{1}{2}$. Including the alternate parametrization (Stein, 1999)

$$\rho = \frac{2\sqrt{\nu}}{\alpha} \tag{3.61}$$

one can write the spherical Matérn covariance as

$$M(\psi) = \frac{\sigma^2 2^{1-\nu}}{\Gamma(\nu)}\left(\frac{2\sqrt{\nu}}{\rho}\psi\right)^{\nu}\mathcal{K}_{\nu}\left(\frac{2\sqrt{\nu}}{\rho}\psi\right) \tag{3.62}$$

for $\sigma^2 > 0$, $\rho > 0$, and $0 < \nu \leq \frac{1}{2}$. This parametrization has the advantage that all the parameters are interpretable without mutual couplings. σ^2 only signifies the value approached for $\psi \to 0$, ν indicates the smoothness around the origin, and ρ is the decorrelation distance, a measure for the decay of the covariance function with great circle distance, which is similar to the spatial range parameter in other covariance models (Stein, 1999). In parametrizations including the parameter α, the behavior of α changes depending on the values of ν.

The constraint $\nu \leq \frac{1}{2}$ of the spherical form of the Matérn covariance is critical for many applications because data fields generated with such a low ν are not smooth. This covariance function therefore should not be used to model smooth processes on the sphere and, compared to its planar equivalent, loses a lot of its

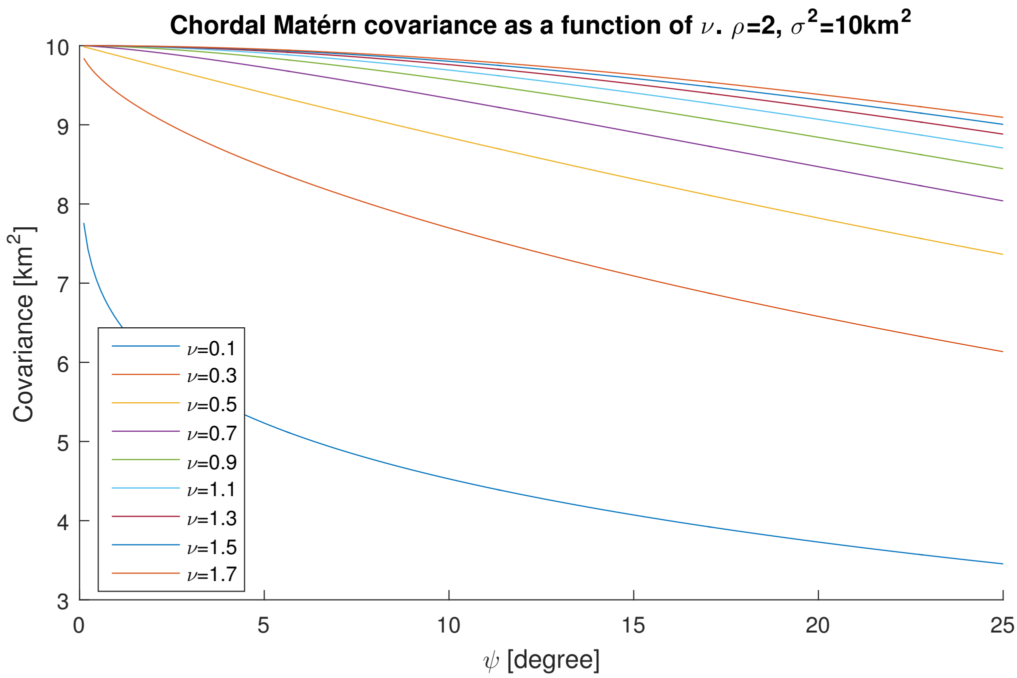

Figure 3.3: Chordal Matérn covariance function for various values of ν. ν mainly influences the smoothness around the origin and leaves the shape of the graph relatively unaffected, except for very small $\nu < 0.5$.

flexibility (Guinness and Fuentes, 2016; Jeong and Jun, 2015). Guinness and Fuentes (2016) discussed several workarounds for the problem of limited smoothness in the spherical case. One of them is the so-called chordal Matérn covariance function $M_c(\psi)$, which replaces the great circle distance ψ by the Euclidian distance $2\sin\frac{\psi}{2}$:

$$M_c(\psi) = \sigma^2 \left(2\alpha \sin\frac{\psi}{2}\right)^{\nu} \mathcal{K}_\nu \left(2\alpha \sin\frac{\psi}{2}\right) \tag{3.63}$$

Using the alternate parametrization of Equation 3.61 and including again the factor $(2^{\nu-1}\Gamma(\nu))^{-1}$, one can write the chordal Matérn covariance function as

$$M_c(\psi) = \frac{\sigma^2 2^{1-\nu}}{\Gamma(\nu)} \left(\frac{4\sqrt{\nu}}{\rho} \sin\frac{\psi}{2}\right)^{\nu} \mathcal{K}_\nu \left(\frac{4\sqrt{\nu}}{\rho} \sin\frac{\psi}{2}\right) \tag{3.64}$$

for $\sigma^2 > 0$, $\rho > 0$, and $\nu > 0$. The chordal Matérn covariance is plotted for various values of ρ and ν in Figures 3.3 and 3.4. It can be seen that the decorrelation distance ρ can be interpreted as the distance in radians, at which the covariance function reaches approximately the value $0.3\sigma^2$. For example, for $\rho = 0.1$, the value $0.3\sigma^2 = 3\,\mathrm{km}^2$ is reached approximately at $\psi = 0.1\,\mathrm{rad} = 5.7°$. Gneiting et al. (2013) deemed this model as potentially yielding unphysical results, but Guinness and Fuentes (2016) found practical evidence for the validity of its application.

For this study, a spectral representation of the covariance function on the sphere is needed, so I isotropically (see Equation 3.4) expand Equation 3.62 or 3.64 into spherical harmonics (Baran and Terdik, 2015)

$$M(\psi) = \sum_{l=0}^{\infty} M_l \bar{P}_{l0}(\cos\psi) \tag{3.65}$$

and define

$$S_{h^i h^i}(l) := M_l\,, \tag{3.66}$$

which finally, after exploiting the concepts of load correlation and proportionality and specifying a spectral form for the covariance of the topography fields, makes it possible to evaluate Equation 3.46 and compute the covariance spectrum of the random process of final topographies.

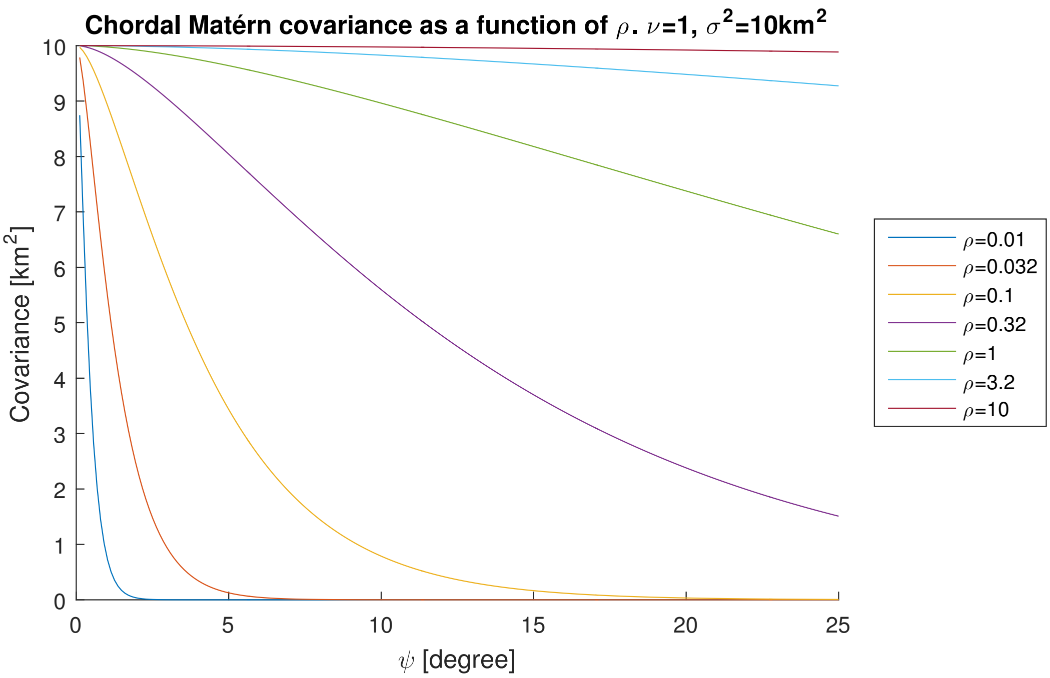

Figure 3.4: Chordal Matérn covariance function for various values of ρ. ρ influences the shape of the graph and the distance at which it becomes close to zero.

Another covariance function proposed by Guinness and Fuentes (2016) is what they call the Legendre-Matérn function

$$M_{\text{Legendre}}(\psi) = \sigma^2 \sum_{l=0}^{L} (\alpha^2 + l^2)^{-\nu-\frac{1}{2}} P_{l0}(\cos\psi) = \sigma^2 \sum_{l=0}^{L} \frac{(\alpha^2 + l^2)^{-\nu-\frac{1}{2}}}{\sqrt{2l+1}} \bar{P}_{l0}(\cos\psi) \tag{3.67}$$

for $\sigma^2 > 0$, $\alpha > 0$, and $\nu > 0$. It is again possible to apply a more useful parametrization

$$M_{\text{Legendre}}(\psi) = \sigma^2 \frac{\Gamma(\nu + \frac{1}{2})}{\sqrt{\pi}\Gamma(\nu)} \left(\frac{4\nu}{\rho^2}\right)^{\nu} \sum_{l=0}^{L} \left(\frac{4\nu}{\rho^2} + l^2\right)^{-\nu-\frac{1}{2}} \frac{1}{\sqrt{2l+1}} \bar{P}_{l0}(\cos\psi) \tag{3.68}$$

which decouples the meaning of the smoothness parameter ν and the decorrelation distance ρ. However, the parameter σ^2 is not the variance of the Legendre-Matérn covariance function, even though it does act as a factor that linearly scales the function. There is no way of scaling the function to have exactly σ^2 as its variance known to me.
This covariance function's spectral representation in the spherical harmonic domain is simply given by

$$M_l = \sigma^2 \frac{\Gamma(\nu + \frac{1}{2})}{\sqrt{\pi}\Gamma(\nu)} \left(\frac{4\nu}{\rho^2}\right)^{\nu} \left(\frac{4\nu}{\rho^2} + l^2\right)^{-\nu-\frac{1}{2}} \frac{1}{\sqrt{2l+1}} \tag{3.69}$$

so that the computation of its spectrum is very easy.

3.3.2. LIKELIHOOD FUNCTION

The probability density function $\mathscr{P}(\boldsymbol{x}|\boldsymbol{y})$ is the function that gives the probability of observing the data $\boldsymbol{x}$ given the parameter set $\boldsymbol{y}$. The likelihood function

$$\mathscr{L}(\boldsymbol{y}|\boldsymbol{x}) = \mathscr{P}(\boldsymbol{x}|\boldsymbol{y}) \tag{3.70}$$

is the reverse of the probability function in the sense that it gives the likelihood that the parameter set $\boldsymbol{y}$ has caused the observed data $\boldsymbol{x}$ (Myung, 2003). The 6-dimensional parameter space is sampled to obtain a variety of parameter sets

$$\boldsymbol{y} = \begin{pmatrix} T_e & F & r & \nu & \rho & \sigma^2 \end{pmatrix}^\top, \tag{3.71}$$

for each of which the likelihood is computed. The most likely parameter set is then accepted as the result. The log-likelihood is the natural logarithm of the likelihood and will give the same maximum as the likelihood, while being more easy to calculate. It is given by (Simons and Olhede, 2013)

$$\mathscr{L}(\boldsymbol{y}|\bar{\boldsymbol{h}}) = \frac{1}{L}\ln\prod_{l=0}^{L}\frac{\exp\left(-\bar{\boldsymbol{h}}^{\top}(l)\bar{\boldsymbol{S}}_{\boldsymbol{hh}}^{-1}(l,\boldsymbol{y})\bar{\boldsymbol{h}}(l)\right)}{\left|\bar{\boldsymbol{S}}_{\boldsymbol{hh}}(l,\boldsymbol{y})\right|} = -\frac{1}{L}\sum_{l=0}^{L}\left(\ln\left(\left|\bar{\boldsymbol{S}}_{\boldsymbol{hh}}(l,\boldsymbol{y})\right|\right)+\bar{\boldsymbol{h}}^{\top}(l)\bar{\boldsymbol{S}}_{\boldsymbol{hh}}^{-1}(l,\boldsymbol{y})\bar{\boldsymbol{h}}(l)\right), \tag{3.72}$$

where $\bar{\boldsymbol{h}}$ is the vector of windowed and localized topography, and $\bar{\boldsymbol{S}}_{\boldsymbol{hh}}$ is the blurred version of the spectral covariance of final topographies from Equation 3.46.

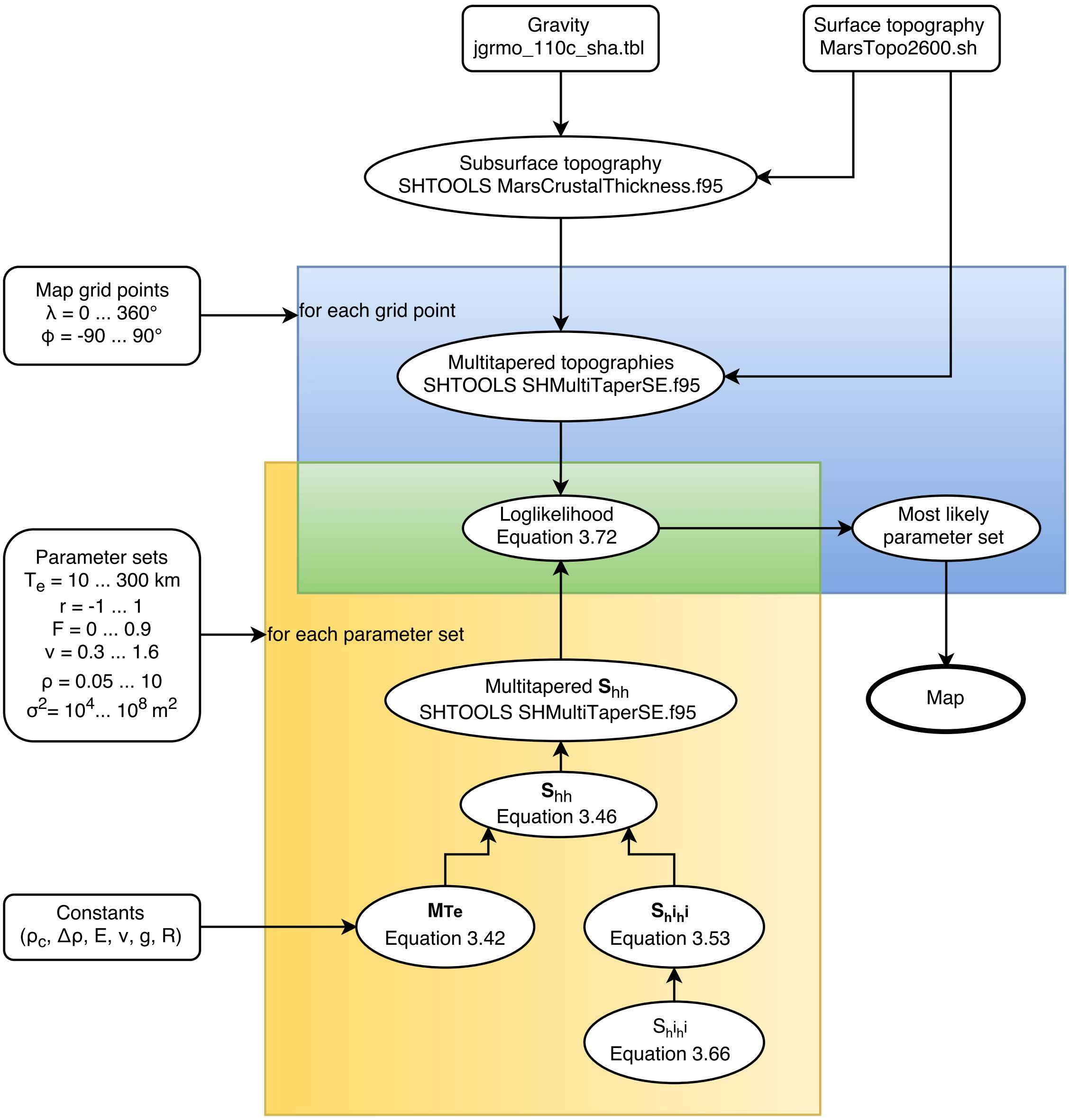

Figure 3.5: Processing scheme for the generation of a global elastic thickness map.

Figure 3.5 summarizes the processing steps described in this chapter which are necessary to compute a global map of the elastic thickness of Mars.

3.4. ERROR ESTIMATION

After determining the most likely parameter sets of geophysical and statistical parameters, Simons and Olhede (2013) go on in their methodology by exploring the statistics of the estimates and giving formulae for variances and confidence intervals. This is possible in the 2D planar case, because an analytic expression for the derivatives of the spectral form of the covariance exists, and might be possible in the 3D spherical case when using the Legendre-Matérn covariance function or a similar one whose spectrum has an analytical expression. I do not attempt this method, and instead use a Monte Carlo approach to determine the uncertainties on the parameters, which can also deal better with the problems introduced into the analytical derivations by blurring of the spectral covariance and small sample sizes (F. Simons, personal communication). When determining uncertainties of the estimated parameters analytically, it would be impossible to also include the effects of multitapering into the derivation of formal variances because there is no simple analytical expression for the multitapering.

First, synthetic planetary topographies are simulated using the maximum likelihood estimates of the six parameters T_e, F, r, ν, ρ, and σ^2. Then, these simulations are treated as new inputs for the geophysical model from which new most likely parameter estimates are generated. This process is repeated for many simulations to generate a large enough sample of most likely parameters generated from simulations. Finally, the standard deviation of the each simulated optimal parameter can be determined. These are the uncertainty estimates of the original most likely solution.

The actual input data, which is the topography and gravity of Mars, is not involved in the error estimation process. Two locations on Mars which happen to have exactly the same most likely solution in all parameters, will also have the same uncertainties attributed to them. For every parameter set and for each simulation created with them, the parameter optimization process has to be run, so that the computation time for the errors is much longer than the computation time of the original estimates. For this reason, I only create error estimates for certain locations on Mars, and not for the entire map.

It is necessary to simulate random fields of planetary topography using a specified set of parameters. Such a simulation of a random field on the sphere is performed using the field's desired power spectrum. First, I will define the power spectra of all topographies of interest.

The power spectrum of the initial surface topography is $S_{h^i h^i}$, as given by either Equation 3.66 for the case of the chordal Matérn covariance function or by Equation 3.69 for the Legendre-Matérn covariance function. The power spectrum of the initial subsurface topography can be obtained from Equation 3.52 as

$$S_{w^i w^i} = S_{h^i h^i} \frac{\rho_c^2}{\Delta\rho^2} f^2 \tag{3.73}$$

and the cross-spectrum of initial surface and subsurface topography can then be obtained over the load correlation (Equation 3.48) as

$$S_{h^i w^i} = r\sqrt{S_{h^i h^i} S_{w^i w^i}}\,. \tag{3.74}$$

While the initial topographies are interesting quantities to understand the flexure process, the final topographies are needed for the error estimation process. The spectra of the final topographies can be determined by Equation 3.46 and Equation 3.44. From the spectra of final surface and subsurface topography S_{hh} and S_{ww} and the cross-spectrum $S_{hw} = S_{wh}$ one can define a correlation coefficient between surface and subsurface as

$$r^f = \frac{S_{hw}}{\sqrt{S_{hh} S_{ww}}}\,. \tag{3.75}$$

A generic random field $f(\Omega)$ on the sphere can be simulated as (Lang and Schwab, 2015)

$$f(\Omega) = \sum_{l=0}^{\infty} \sum_{m=-l}^{l} \sqrt{\frac{S_{ff}}{\sqrt{2l+1}}} X_{lm} Y_{lm}(\Omega) \tag{3.76}$$

where S_{ff} is the field's power spectrum, and X_{lm} is a sequence of independent, real-valued, standard normally distributed random variables.

For the simulation of topography fields I set the degree zero term to zero, so that the resulting field can be interpreted as undulations on an interface with unspecified distance from the center of mass. Removing the degree zero term does not have any effect on the actual error estimation process, because in the multitapering the lowest degrees of all fields are removed, but it facilitates understanding of the simulated fields itself. The random field of initial surface topography is then given by

$$h^i(\Omega) = \sum_{l=1}^{\infty} \sqrt{\frac{S_{h^i h^i}(l)}{\sqrt{2l+1}}} \sum_{m=-l}^{l} X^1_{lm} Y_{lm}(\Omega). \tag{3.77}$$

In order to express load correlation in the initial subsurface topography, correlated random variables are generated as

$$X_{lm} = r X^1_{lm} + \sqrt{1-r^2} X^2_{lm} \tag{3.78}$$

where X^1_{lm} is the sequence of random variables used for the simulation of the initial surface topography, and X^2_{lm} is a new sequence of independent, real-valued, standard normally distributed random variables. Then, the simulated initial subsurface topography can be written as

$$w^i(\Omega) = \sum_{l=1}^{\infty} \sqrt{\frac{S_{w^i w^i}(l)}{\sqrt{2l+1}}} \sum_{m=-l}^{l} \left(r X^1_{lm} + \sqrt{1-r^2} X^2_{lm} \right) Y_{lm}(\Omega). \tag{3.79}$$

Analogously, for the final topographies one can write

$$h(\Omega) = \sum_{l=1}^{\infty} \sqrt{\frac{S_{hh}(l)}{\sqrt{2l+1}}} \sum_{m=-l}^{l} X^1_{lm} Y_{lm}(\Omega) \tag{3.80}$$

$$w(\Omega) = \sum_{l=1}^{\infty} \sqrt{\frac{S_{ww}(l)}{\sqrt{2l+1}}} \sum_{m=-l}^{l} \left(r^f X^1_{lm} + \sqrt{1-(r^f)^2} X^2_{lm} \right) Y_{lm}(\Omega) \tag{3.81}$$

where again X^1_{lm} and X^2_{lm} are sequences of independent, real-valued, standard normally distributed random variables.
The truncation error of the random field $f(\Omega)$ (Equation 3.76) is bounded if and only if its power spectral density decays algebraically with order $k > 2$, such that

$$\frac{S_{ff}}{\sqrt{2l+1}} \leq C l^{-k} \tag{3.82}$$

where C is a constant. Inserting the spectrum of the Legendre-Matérn covariance function (Equation 3.69) gives

$$\sigma^2 \frac{\Gamma(\nu+\frac{1}{2})}{\sqrt{\pi}\Gamma(\nu)} \left(\frac{4\nu}{\rho^2}\right)^{\nu} \left(\frac{4\nu}{\rho^2} + l^2\right)^{-\nu-\frac{1}{2}} \frac{1}{2l+1} \leq C l^{-k}. \tag{3.83}$$

It can be shown that for any value of $\nu > 0$, there is a $k > 2$, so that this inequality holds. For parametrizations of the Matérn covariance in the spatial domain is not straightforward to prove that the truncation error is bounded, but because they are only different parametrizations of the same covariance function, I conclude that this inequality is also valid.
The simulated random fields of surface topography $h(\Omega)$ and subsurface topography $w(\Omega)$ are generated using the most likely solutions of all the six parameters of our model: Elastic thickness T_e, load ratio F, load correlation r, smoothness ν, decorrelation distance ρ, and variance σ^2. Examples are given in Section 4.5. These simulated topographies are then used as an input of the same model again, they are tapered the same way as the original data, and compared with the modelled covariance spectra of topographies as in Equation 3.72 to determine the parameter set that is most likely to have caused these simulated topographies. Ideally, it would be expected that this is identical to the parameter set used for the simulation. All deviations from the input parameters are due to model failure and can therefore be used as an uncertainty estimation of the most likely solution.
Table C.1 gives an overview of all symbols and quantities used in this study.

4

RESULTS

4.1. SUBSURFACE TOPOGRAPHY

The two input quantities to the maximum likelihood estimation of the elastic thickness are the surface topography h and the subsurface topography w. While the surface topography is directly observable, the subsurface topography is not, and therefore it has to be computed beforehand from the surface topography and the gravity. This has been done in this study using the finite-amplitude correction method by Wieczorek and Phillips (1998) which has been summarized in Section 3.2.4.

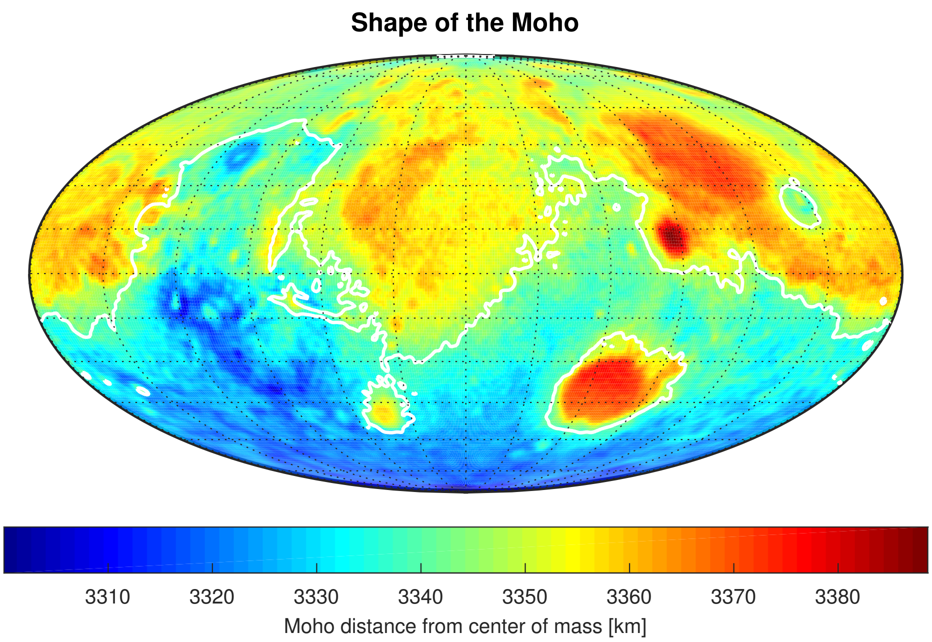

Figure 4.1: The subsurface topography of Mars at the Moho.

The minimum amplitude downward continuation filter χ_l (Equation 3.30) is used. It is adjustable over the Lagrange multiplier λ which determines how strongly the subsurface topography is smoothed in the filtering. For $\lambda = 0$, no smoothing is applied, which causes an unrealistically rough subsurface topography, and for increasing values of λ more short wavelength information is suppressed. I choose λ such that $\chi_l = \frac{1}{2}$ for $l = 70$ because this eliminates short wavelength noise sufficiently (see Figure 4.1). I calculate the subsurface topography up to $L = 110$ because spherical harmonic fields up to high degrees are needed for the multitapering (see Section 3.1) and evaluate the sum in Equation 3.29 up to $n_{\text{max}} = 6$. The calculation was carried out using the `MarsCrustalThickness.f95` script of Wieczorek et al. (2015) under usage of a minimum crustal

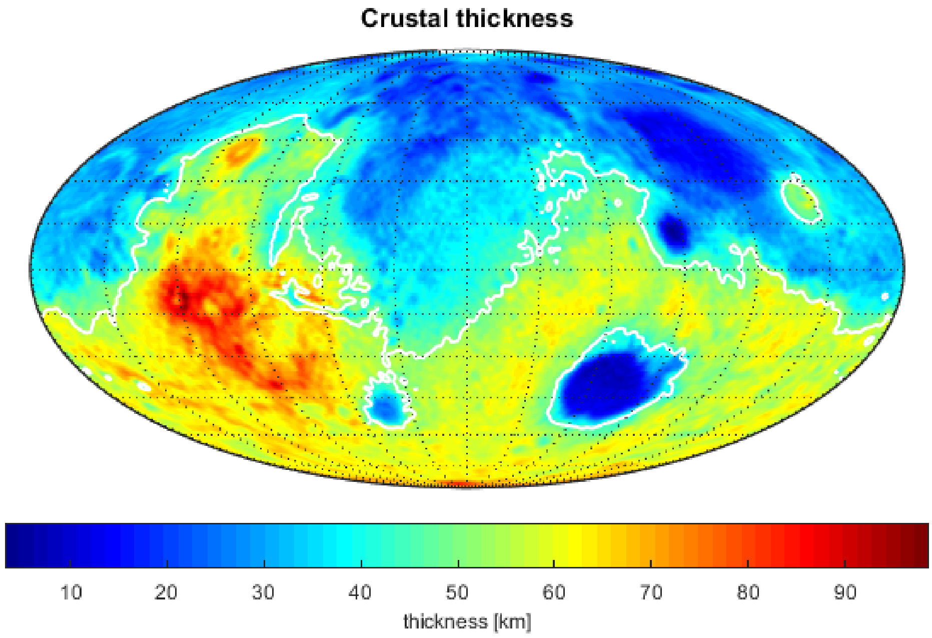

Figure 4.2: The crustal thickness of Mars.

thickness value of 3 km. The result is shown in Figure 4.1.
The crustal thickness can easily be computed as

$$T_c = h - w \tag{4.1}$$

and is plotted in Figure 4.2 for easier interpretability. It compares favourably to the results of Neumann et al. (2004) who used a very similar, but more sophisticated method.

4.2. Parameters of the Matérn covariance function

The log-likelihood equation (Equation 3.72) is used to calculate the likelihood of a certain parameter set to have caused the observed topographies. For each of the six parameters y_i a vector of n_{y_i} possible values is chosen, and then the log-likelihood equation is evaluated for all

$$n_{\text{tot}} = \prod_{i=1}^{6} n_{y_i} \tag{4.2}$$

combinations of those vectors. This method is a gridded sampling of the 6-dimensional parameter space. For each of the n_{tot} parameter sets, the spectral covariance of the final topographies $\boldsymbol{S_{hh}}$ has to be computed and multitapered. In fact, the multitapering is the bottleneck in the time complexity of the whole elastic thickness mapping algorithm (see also Figure 3.5). If one would apply an iterative algorithm, for example Newton's method, one could find a most likely solution for one map point (θ, λ) much faster and more precisely than with the grid sampling. However, this study focuses on the creation of a map, and therefore it is necessary to calculate the log-likelihood at each map grid point (θ, λ). An iterative algorithm would have to be initialized from zero or close to zero for each map grid point. Therefore, I believe that the grid sampling is an efficient approach for the problem treated in this study, and furthermore it is simple to implement.
The choice of values at which each parameter should be evaluated must be taken with care, both because of additional program run time caused by unnecessary values and because of the effect which unphysical parameters may have on the most likely solution. The parameters $T_e \lesssim 300\,\text{km}$, $0 \leq F < 1$, and $-1 \leq r \leq 1$ have obvious physical limitations, whereas the parameters of the Matérn covariance function have to be assessed more carefully. Using the parametrization from Equation 3.64, I compute an experimental covariance function from the shape of Mars to roughly find possible values of the parameters σ^2, ρ, and ν. Note, however, that the covariance function will in the end model the initial surface topography, while all experimental constraints can only be obtained from the final surface topography. This difference should not have any practical

impact when I assume that the initial and final surface topographies have very similar statistical properties. After a transformation of the shape field into the space domain, 1000 random points $\Omega = (\theta, \lambda)$ on the surface of Mars are chosen and an experimental variogram is computed. The dissimilarity between any two points at locations Ω and Ω' is

$$d(\Omega, \Omega') = \frac{(h(\Omega) - h(\Omega'))^2}{2} \tag{4.3}$$

and can be plotted against a lag distance in the form of the great circle distance $\psi(\Omega, \Omega')$ between the two points. Binning and averaging the results with respect to great circle distance gives the so-called experimental variogram.

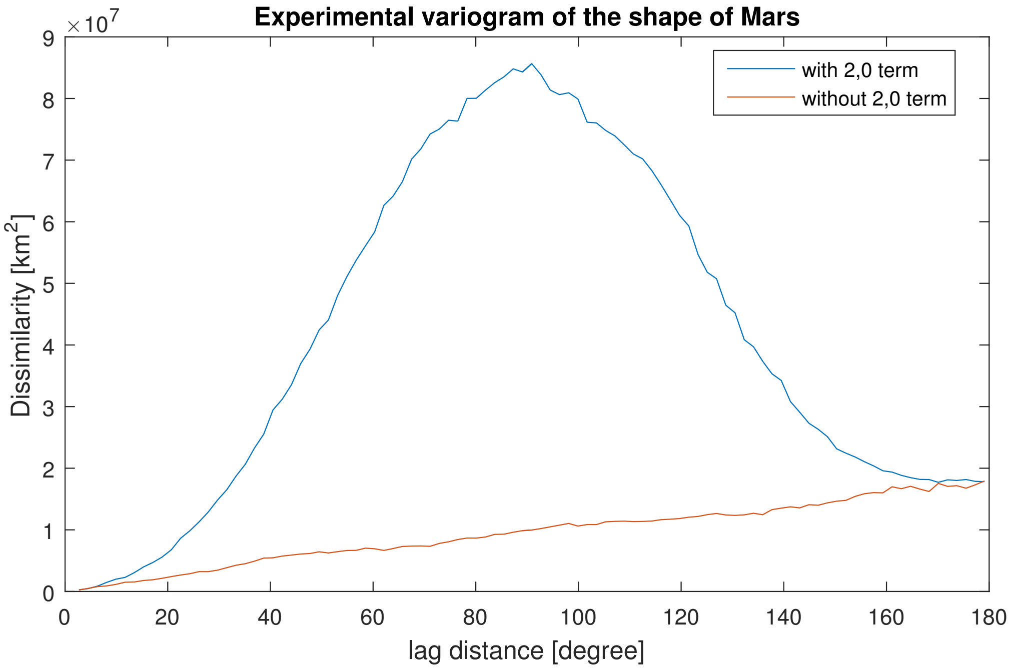

Figure 4.3: Experimental variogram of the shape of Mars with and without the $l = 2$, $m = 0$ coefficient.

The equatorial bulge is very visible in the variogram and is superposed to a linear trend which is visible when the variogram is computed after setting $h_{20} = 0$ (Figure 4.3). Variogram functions generally flatten off at a level σ^2 which is reached after a distance which is related to the parameter ρ. This behavior is not visible in the variogram of the Martian shape which implies some correlation even at very large distances. This leaves the variance σ^2 unconstrained and implies a large value for the decorrelation distance ρ. Because of this, the purpose of fitting a theoretical variogram function such as the Matérn variogram function $\sigma^2 - M$ is questionable.

A lower limit for the decorrelation distance ρ can be obtained by stating that a signal cannot decorrelate over a distance that is smaller than its spatial resolution. All data sets used in this study are truncated after degree $L = 100$, which has an equivalent Cartesian wavelength of $\lambda_l = 212\,\text{km}$ or about $3.6° = 0.06\,\text{rad}$. On the other limit, the experimental variogram of the shape of Mars shows that the decorrelation distance can be larger than the circumference of the planet. Therefore, I constrain the range parameter as $0.05 < \rho < 10$.

The effect of the limited resolution of the global fields to degree $L = 100$ can also be illustrated practically by investigating the truncation error. The chordal Matérn covariance function has its analytical expression given in the spatial domain as a function of great circle distance (Equation 3.64). It is transformed into the spherical harmonic domain because the covariance spectrum is needed for further analysis. In this transformation degrees larger than $L = 100$ are cut off, which results in a loss of high frequency signal. For low values of decorrelation distance (Figure 3.4) and smoothness (Figure 3.3), the covariance function is decreasing very quickly close to the origin. This is a high frequency signal, a lot of whose power is in the spherical harmonic degrees larger than $L = 100$ and is lost in the transformation. The truncation error can be assessed by retransforming the covariance spectrum into the spatial domain, and comparing this with the original covariance.

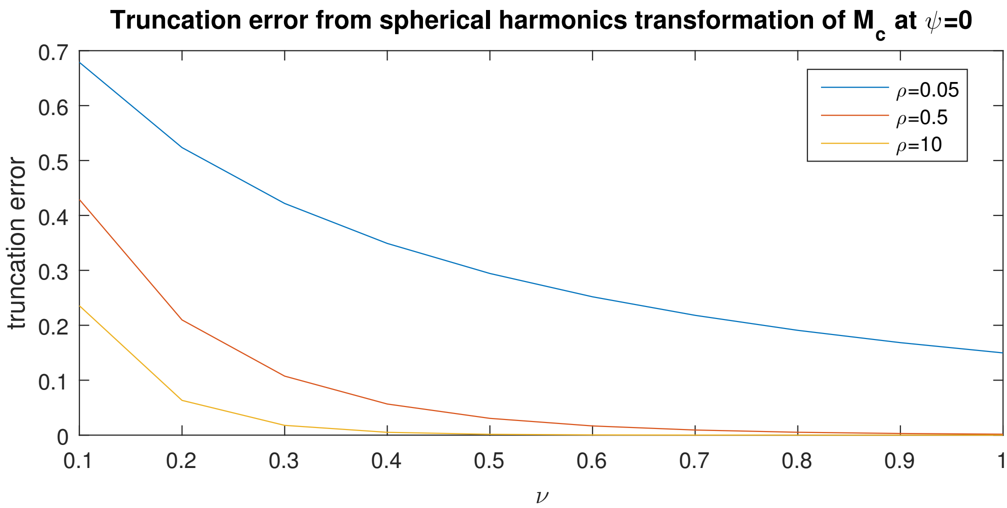

Figure 4.4: Truncation error introduced by spherical harmonics transformation into the chordal Matérn covariance function $M_c(0)$ at the origin for various values of smoothness ν and decorrelation distance ρ. Truncation error values relate to a true value of 1 at the origin.

It can be seen that the peak value close to the origin is cut off while the rest of the function is almost identical (see also Figure 4.14).
Therefore, I compare the values at $\psi = 0$ of the original and retransformed covariance functions. Their normalized difference is plotted in Figure 4.4. It can be seen that the truncation error decays with increasing ν and ρ. For $\nu = 0.1$ and $\rho = 0.05$ almost 70% of the signal is lost. For $\nu = 0.2$ at least 6% of the signal is lost, even for a very high $\rho = 10$. This means that topography of the available resolution cannot be modelled with such low smoothness values, simply because such a quick decay of the covariance function cannot occur because of the low resolution. Even if the topography between two neighboring pixels would be completely decorrelated, it does not decorrelate as fast as for such low smoothness values. Guinness and Fuentes (2016) found a value of $\nu = 1.5$ for the smoothness parameter for global temperature data. I assume shape data to be less or equally smooth and constrain therefore $0.3 \le \nu \le 1.6$. Still, within these limits, one has to be cautious about combinations of low smoothness and low decorrelation distance values.
The variance can be constrained by noting that it is essentially a function of the maximum topography difference between two points in the area of interest. I set constraining values as $0.1\,\text{km}^2 < \sigma^2 < 100\,\text{km}^2$.

Table 4.1: Overview of parameter constraints and sampling intervals.

Parameter	Lower limit	Interval	Upper limit	n_{y_i}
Elastic thickness T_e	10 km	10 km	300 km	30
Load ratio F	0	0.1	0.9	10
Load correlation r	-1	0.2	1	11
Smoothness parameter ν	0.3	0.325	1.6	5
Decorrelation distance ρ	0.05	Logarithmically spaced	10	5
Variance σ^2	$10^4\,\text{m}^2$	Logarithmically spaced	$10^8\,\text{m}^2$	5

My choices for parameter constraints are in general supported by the fact that the extreme values are not found to be the most likely ones very often. The parameter constraints and the sampling intervals used in this study are summarized in Table 4.1.

4.3. MAPPING THE ELASTIC THICKNESS

First, I present results obtained using only $K = 1$ taper. This allows to keep the window size at $\theta_0 = 10°$ with a bandwidth of $L_b = 35$, which leaves the spherical harmonic degrees 41 to 64 for the flexural analysis. A regular $4° \times 4°$ grid covering the entire globe has been used for the center points of the windows. The observed and modelled topographies have been localized to each of these windows. A most likely parameter set has been computed for each localization. The most likely elastic thickness values have been assigned to the central

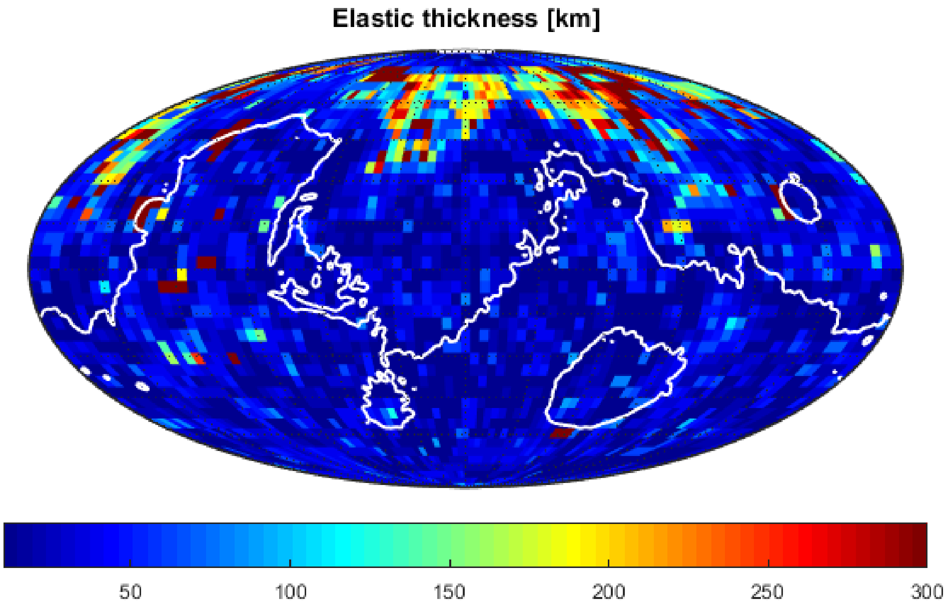

Figure 4.5: Map of the elastic thickness of Mars created using the chordal Matérn covariance function and tapering with $K = 1$ taper and a spherical cap size of $\theta_0 = 10°$. The white line is a contour at the level of the mean planetary radius of 3389.500 km and the same as in Figure 2.1.

points of their respective windows and are presented in a map (Figure 4.5).
T_e is generally lower than 60 km in the southern uplands, with many locations reaching 10 km, which is the minimum value allowed in this experiment (compare Table 4.1). Some single pixels in the Argyre basin and northeast of Hellas basin reach values of above 100 km, and south of Hellas even 300 km, which is the maximum value.
In the Tharsis region the general behavior is similar, with some locations in the proximity of the large volcanoes and Alba Patera reaching $T_e = 300$ km, but most of the remaining area staying below about 60 km. Notably, at the peak of Olympus Mons, the value is only 70 km, though, and 30 km at Ascraeus Mons. Also west of Elysium Mons, some locations reach 300 km, while the peak blends in with its surroundings at 20 km. Remarkably, there are often abrupt transitions between values of 300 km in one pixel and values of less than 60 km, in some cases even 10 km, in the next pixel. Intermediate values are rarely found in the volcanic regions. The center of the Isidis basin has an elastic thickness of around 200 km.
In the northern lowlands the T_e values are very mixed. There are some larger areas northeast of Elysium Mons and around the north pole with $T_e = 10$ km, but most of the central northern lowlands, especially between 30°N and 80°N and when far away from the highlands and volcanoes, reach at least 50 km. Values range up to 300 km and all intermediate values can be found, but the behavior is not very smooth, and areas with a difference of 250 km in elastic thickness bordering each other directly are common.
Such abrupt changes of elastic thickness over relatively small distances seem geophysically unlikely. The T_e value of each pixel of 4° represents the most likely elastic thickness value for a spherical cap of $\theta_0 = 10°$ which is centred around that location. Therefore, there is a big overlap between the spherical caps of two neighboring pixels. Completely different parameter values in two neighboring pixels indicate unconstrained parameter values.
Figure 4.6 shows maps of the most likely solutions for not only the elastic thickness, but also all other parameters, the most important trends of which I describe in the following paragraphs.
The load ratio in the southern uplands usually lies between 0.4 and 0.7, but exceptionally values between 0.1 and 0.9 are possible. Around Olympus Mons, Elysium Mons, the Tharsis Montes, and Valles Marineris, values below 0.3 are reached. The northern lowlands have a very high load ratio, peaking at 0.9 in most areas, which is the largest allowed value in this experiment. Exceptions from this are a large region around Elysium Mons and the north pole. While the load ratio is generally a lot smoother than the elastic thickness, there are still a lot of instances where transitions between high and low values are abrupt. The smallest sampled value $F = 0$

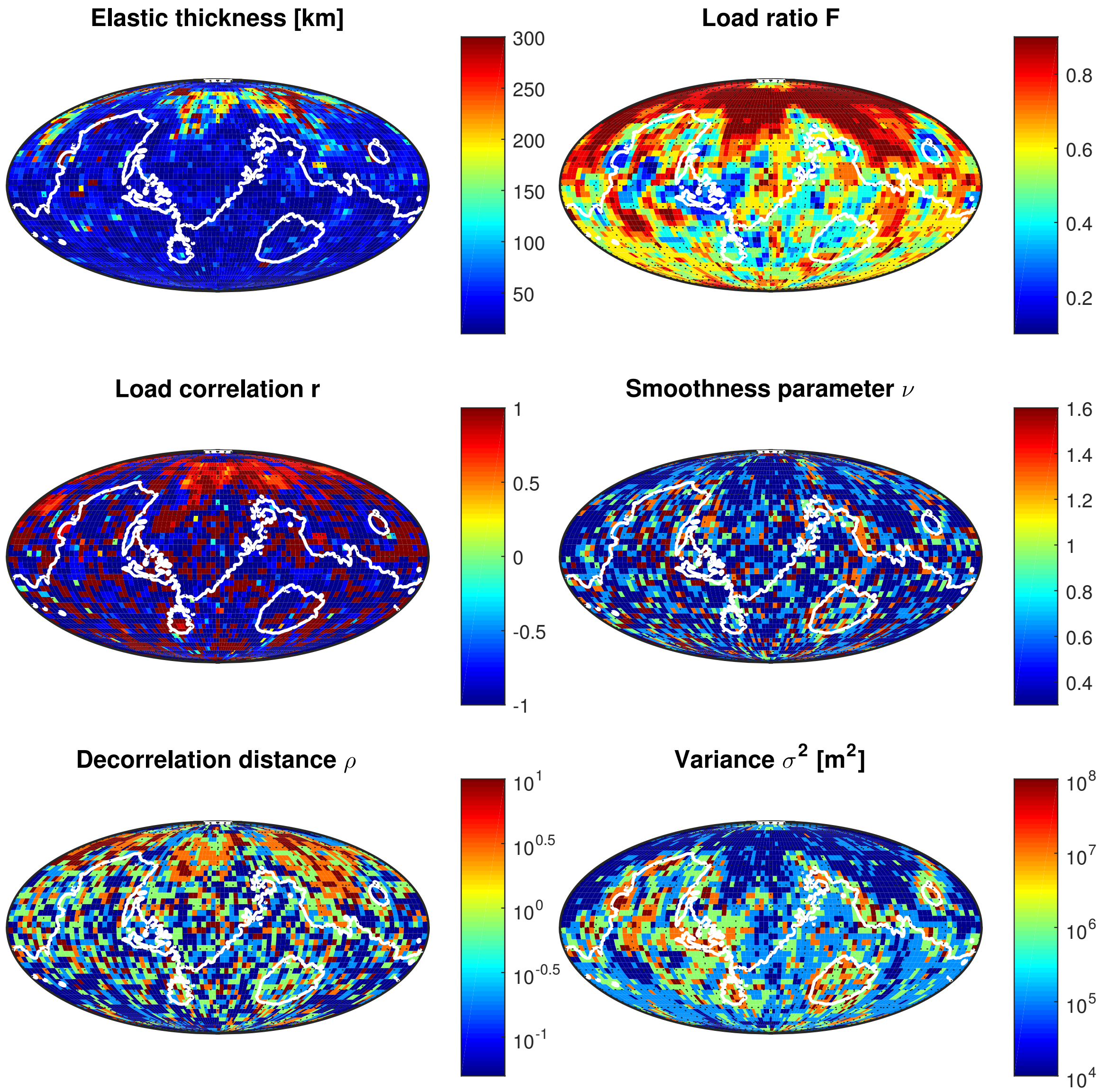

Figure 4.6: Maps of most likely solutions for the six estimation parameters created using the chordal Matérn covariance function and tapering with $K = 1$ taper and a spherical cap size of $\theta_0 = 10°$. The elastic thickness map is identical to the one in Figure 4.5, but plotted again for better comparison.

is not the most likely value for any pixel.

The load correlation is either lower than -0.8 or exactly 1 at almost all locations. The negative and positive extremes are arbitrarily mixed. Only in those areas of the northern lowlands where the most likely elastic thickness and load ratio estimates are high, there are also values of $r = 0.4$ to $r = 0.8$. Furthermore, there are some single pixels of intermediate load correlation values distributed over the globe in an indiscernible pattern. The mix between strong positive and negative correlation indicates that the model cannot distinguish well between these two kinds of correlation and rather only between strong and weak correlation. Remarkably, low correlation $r \approx 0$ practically does not occur.

All possible values of the smoothness parameter ν between 0.3 and 1.6 occur frequently and seemingly very randomly, with 0.3 the most common one. I recognize slightly lower smoothness in the northern lowlands and slightly higher averages in the Isidis and Hellas basins, but a reliable interpretation is very difficult due to

how scattered the map is.
The same issue holds for the decorrelation distance ρ. For this parameter, all values between 0.05 and 10 occur in a very scattered manner. In the northern lowlands, the value $\rho = 2.7$ is most common, whereas in the southern uplands and in the Tharsis region the average is lower than that.
The variance σ^2 is evidently correlated with the roughness of the shape of Mars. In the smooth northern lowlands the value $\sigma^2 = 10^4\,\mathrm{m}^2$ dominates, while in the cratered southern uplands the most common value is at $10^5\,\mathrm{m}^2$ slightly higher. The dichotomy boundary, the large basins, most of the Tharsis region, and the surroundings of Valles Marineris reach $\sigma^2 = 10^7\,\mathrm{m}^2$ and the highest peaks of Olympus and Elysium Mons reach the highest allowed value $10^8\,\mathrm{m}^2$. The relatively smooth southwestern part of Tharsis shows a low variance of $\sigma^2 = 10^4\,\mathrm{m}^2$, giving further evidence for a correlation between variance and roughness of the surface. However, there are also frequent pixels whose values are very different from their neighbors, like in the maps for the other parameters.
In conclusion, the maps of most likely parameters in Figure 4.6 have shown that there are some clearly visible trends and quite some correlation between the parameters themselves and between them and the main geological provinces of Mars. However, in an analysis with a spherical cap size of $\theta_0 = 10°$, there is also a lot of scatter in all the parameters.

4.4. INFLUENCE OF TAPERING PARAMETERS

The next experiment I present uses $K = 1$ taper again, but the spherical cap size is increased to $\theta_0 = 15°$. Accordingly, the bandwidth decreases to $L_b = 23$, which leaves the degrees 29 to 76 for the analysis.
In the southern uplands, T_e values (Figure 4.7) are generally lower than 40 km with most pixels having 10 km as their most likely solution and some isolated pixels ranging up to 180 km.

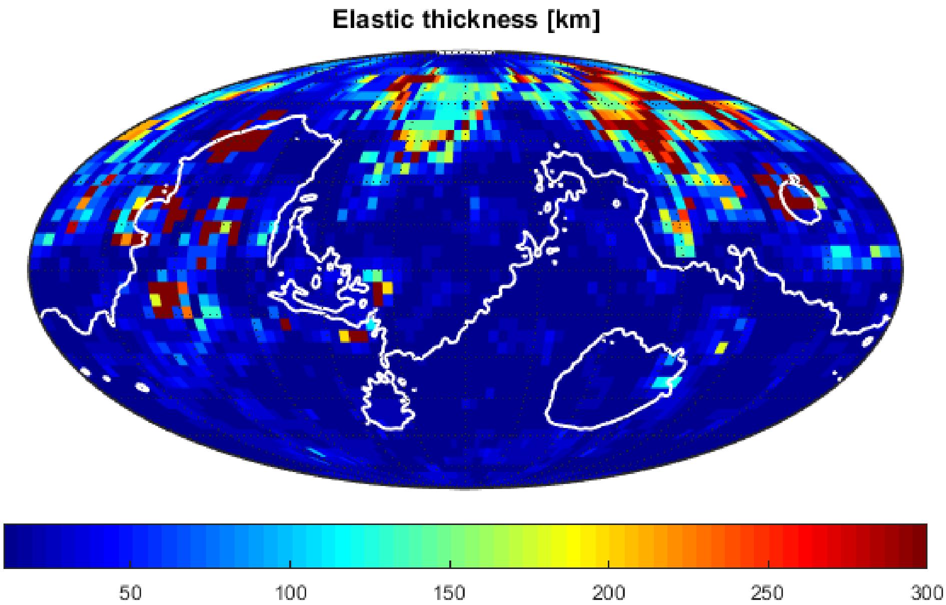

Figure 4.7: Map of the elastic thickness of Mars created using the chordal Matérn covariance function and tapering with $K = 1$ taper and a spherical cap size of $\theta_0 = 15°$.

In the Tharsis region, areas close to the large volcanoes and Alba Patera often reach the maximum value of $T_e = 300\,\mathrm{km}$, and values range down to 10 km in the other parts. The peak of Olympus Mons only reaches values of about 50 km, but is surrounded by a ring of high elastic thickness values of 300 km. The same behavior is observed at Elysium Mons, and to some extent also around Valles Marineris, although values there only reach 300 km in a few instances.
In the northern lowlands, all values between 10 km and 300 km are present, with large areas of low T_e close to Elysium Mons and the north pole, and a large area of high T_e northwest of Elysium Mons. Around longitude 15°W, there is a large area of $T_e \approx 120\,\mathrm{km}$ which seems to be surrounded by a belt of higher T_e up to 300 km.

In comparison with the cap size of $\theta_0 = 10°$, the map with $\theta_0 = 15°$ is slightly smoother. Around the largest elevation peaks (Olypus and Elysium Mons and Valles Marineris) rings of high T_e have become visible while the peaks themselves have low T_e. This feature was to some extent already visible around Olympus Mons for the map with smaller cap size, but here the ring has widened and is located further away from the central peak. This widening might be due to the increase in cap size; pixels further away from the peak now include information about it.

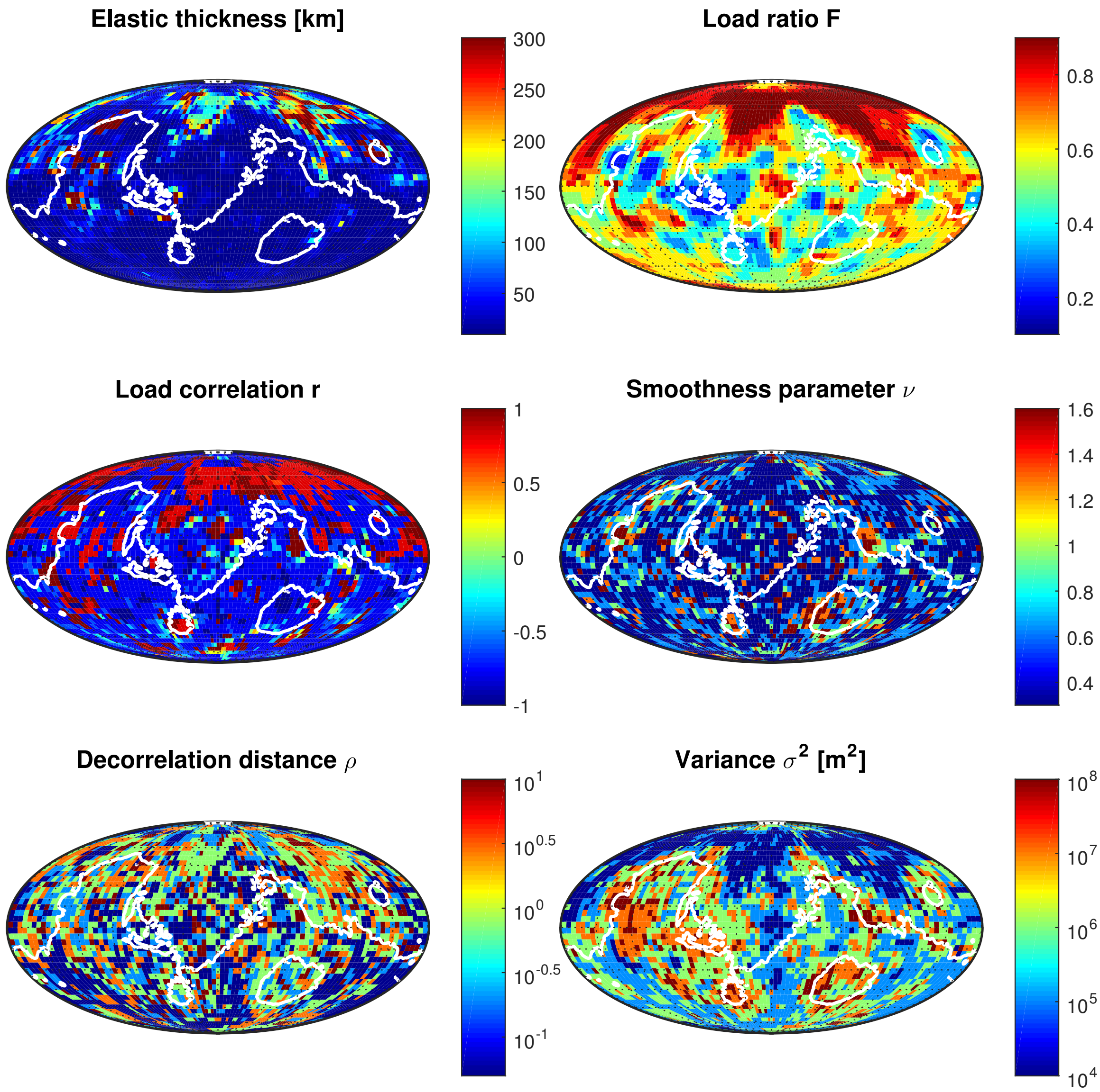

Figure 4.8: Maps of most likely solutions for the six estimation parameters created using the chordal Matérn covariance function and tapering with $K = 1$ taper and a spherical cap size of $\theta_0 = 15°$. The elastic thickness map is identical to the one in Figure 4.7, but plotted again for better comparison.

In the case of the load ratio F (Figure 4.8), a significant smoothing has taken place in comparison to the map with smaller cap size. This smoothing favors low and medium values, so that areas of $F = 0.9$ in the Tharsis region and in the northern lowlands have receded.
For the load correlation, $r = 0.8$ and $r = -0.8$ are now the most common occurrences. Previously small patches of high correlation or anti-correlation have changed into larger, more homogeneous patches. There

is a clear preference for strong positive correlation in the northern lowlands and for strong negative correlation in the southern uplands. Intermediate values are again quite rare, but there are some areas of low correlation in the southern uplands.
The smoothness ν reaches all values from 0.3 to 1.6, with 0.3 the most common value globally. The map for $\theta_0 = 15°$ is slightly less scattered than the map for $\theta_0 = 10°$. High smoothness values of 1.3 and higher are found in all three major impact basins and around Olympus Mons.
The decorrelation distance ρ also remains very scattered, with a slightly higher average in the northern highlands.
The behavior of the variance σ^2 for increasing cap size is similar to that of the load ratio F. Low variance regions in the northern lowlands and southwest of Tharsis recede to make room for more extended areas of high variance. This behavior seems obvious where a larger cap is more likely to include varied topography which increases the variance within that cap.
In conclusion, the most visible effect of a larger cap size of $\theta_0 = 15°$ compared to $\theta_0 = 10°$ is the smoothing in all parameters. The transitions between two zones of different topographies become larger which is obvious because also pixels further away from topographic features become influenced by them. Most strikingly this is visible in ring patterns around locations of extreme elevation.
The multitaper spectral estimate becomes statistically more representative with an increasing number of tapers. Therefore, in my next experiment, I increase the number of tapers to $K = 2$, while keeping the cap size at $\theta_0 = 15°$, so that the bandwidth is again $L_b = 35$.

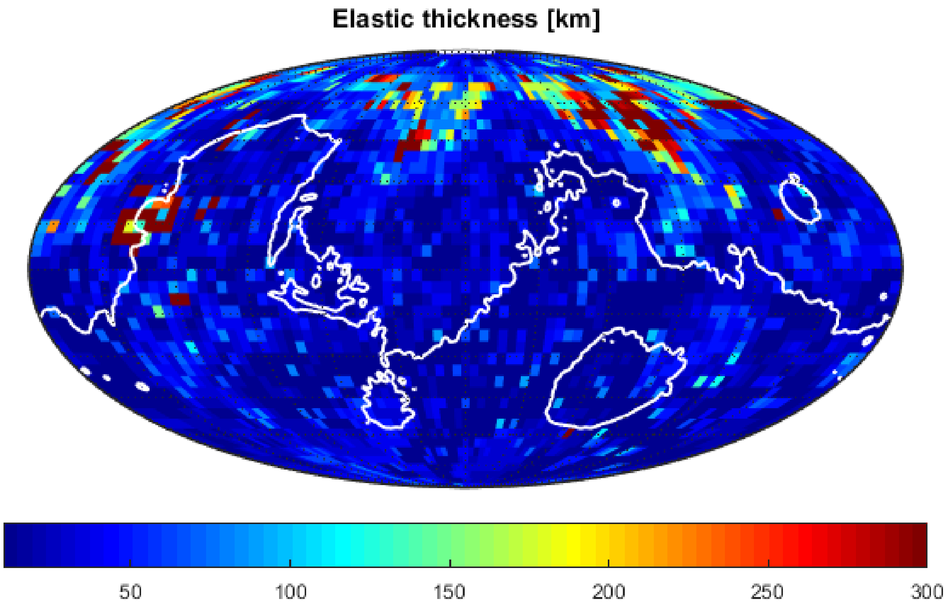

Figure 4.9: Map of the elastic thickness of Mars created using the chordal Matérn covariance function and tapering with $K = 2$ tapers and a spherical cap size of $\theta_0 = 15°$.

For the analysis with $K = 2$ tapers and a spherical cap size of $\theta_0 = 15°$, the elastic thickness in the southern uplands is generally lower than 50 km, with some pixels reaching up to 130 km, and one pixel on the south rim of Hellas at 300 km.
In the Tharsis region, the only large area with high elastic thickness values of up to 300 km is around Olympus Mons. Apart from that, there are only single pixels with high T_e. Elysium Mons is also barely distinguishable from its surroundings, with only one location reaching 130 km.
In the northern lowlands, values of 40 km to 70 km are very abundant, and only relatively small areas have a T_e larger than that, reaching up to 300 km in some locations.
In general, these results are much more reminiscent of the experiment with $K = 1$ taper and $\theta_0 = 10°$ than of the one with $\theta_0 = 15°$.
In the maps of the remaining parameters (Figure 4.10) no new trends can be clearly identified, but they can in general be regarded as intermediate between the solutions for $K = 1$ taper and $\theta_0 = 10°$ and $\theta_0 = 15°$, re-

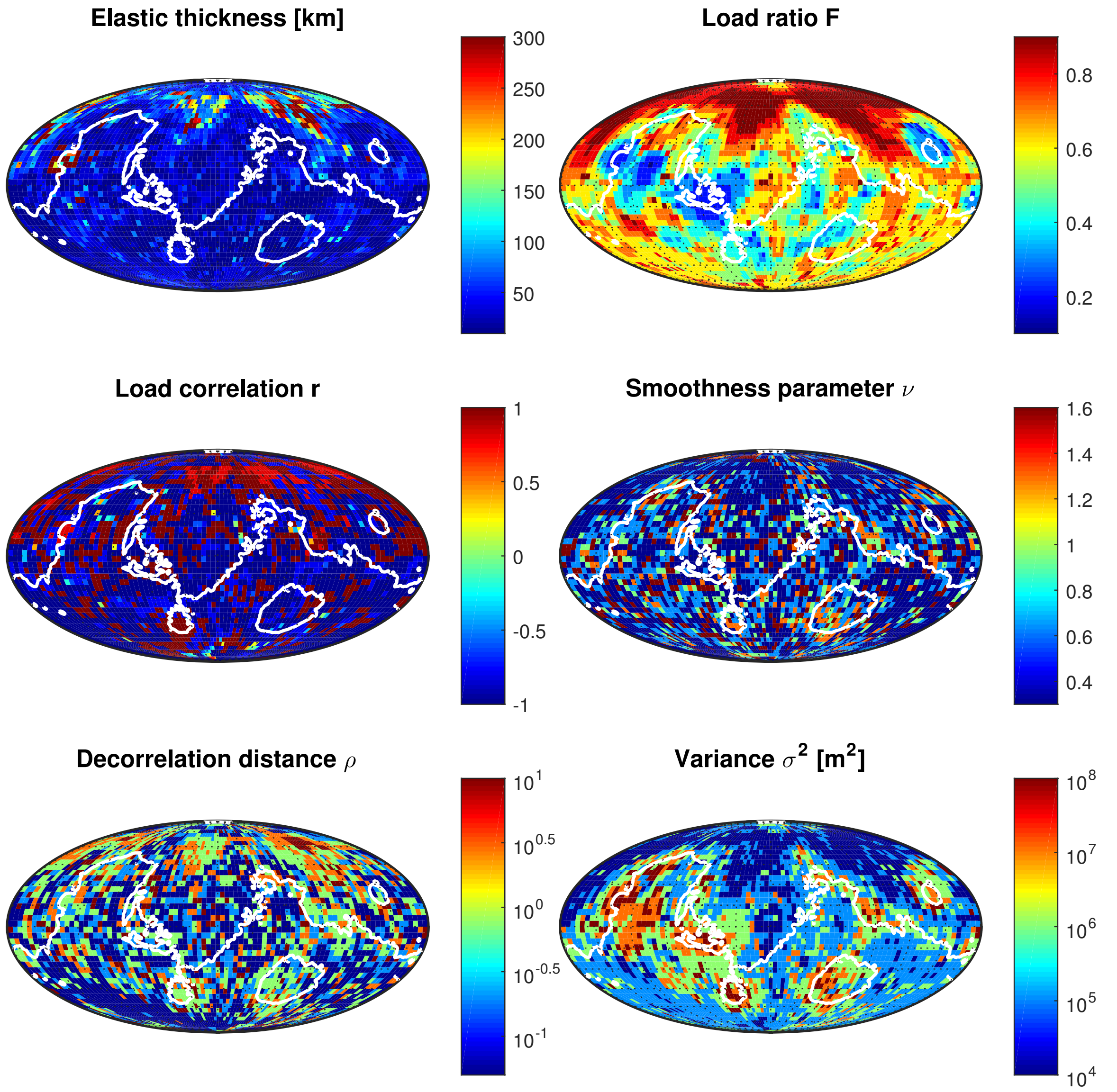

Figure 4.10: Maps of most likely solutions for the six estimation parameters created using the chordal Matérn covariance function and tapering with $K = 2$ tapers and a spherical cap size of $\theta_0 = 15°$. The elastic thickness map is identical to the one in Figure 4.9, but plotted again for better comparison.

spectively. They are less smooth than the results of the experiment with $\theta_0 = 15°$, but more smooth than the results for $\theta_0 = 10°$. The reason for this decreased smoothness with respect to the same cap size and one less taper is unclear. When using two tapers instead of one, the results of the two tapers are averaged and should therefore be more statistically significant and contain less outliers. The downside is that the bandwidth which is usable for analysis decreases which might be the dominant effect in this case.

Next, I study very large spherical caps of $\theta_0 = 30°$ and increase the number of tapers to $K = 3$ because the resulting bandwidth $L_b = 24$ is still quite small.

This experiment (Figure 4.11) results in very low T_e values in the southern uplands, where T_e is almost everywhere 10 km.

Olympus Mons reaches 300 km at its peak and is surrounded by a region of high T_e values, which has a radius of approximately 30°. Values in this area reach from 100 km to 300 km and are distributed unevenly. Some

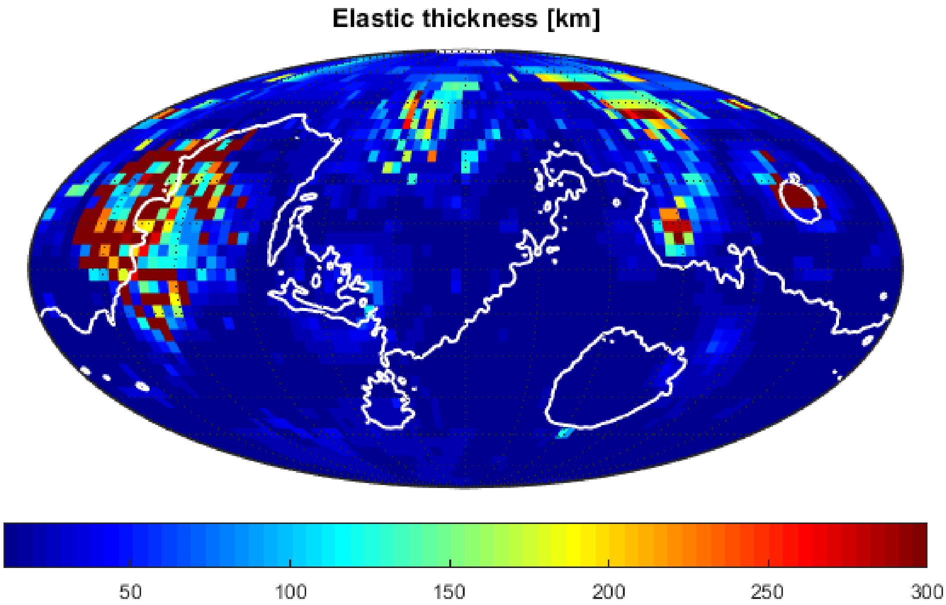

Figure 4.11: Map of the elastic thickness of Mars created using the chordal Matérn covariance function and tapering with $K = 3$ tapers and a spherical cap size of $\theta_0 = 30°$.

locations further south of this area also have high T_e values of up to 300 km. These areas are in the proximity of the Tharsis Montes, and specifically Arsia Mons. Valles Marineris itself has a very low T_e of 20 km, but it is surrounded by an annulus of higher T_e values ranging from 30 km in the west to 110 km in the east. At Elysium Mons, the exact opposite can be observed: The peak reaches 300 km, and is surrounded by a ring of locations with $T_e = 10$ km at about 25° distance from the peak. In between, there are intermediate values of mostly around 40 km. These annular features are very reminiscent of those observed in the experiment with $K = 1$ taper and $\theta_0 = 15°$, but their size has approximately doubled, as has the cap size.

In the northern lowlands values range from 30 km to 300 km, but only few locations surpass 150 km. The spatial distribution is similar as in the previous experiments. In the Isidis basin, there is a quite pronounced peak reaching up to 300 km in the center of the basin.

In conclusion, this experiment serves as further evidence that large cap sizes indeed make the resulting maps more smooth. However, all solutions for locations within a 30° proximity of prominent elevation features, such as Olympus Mons, Elysium Mons, and Valles Marineris, should be treated cautiously. Due to the large cap size, these solutions include signal from those features which may strongly bias the estimation.

This is also visible in the estimates of the load ratio F (Figure 4.12) which is 0.3 and lower in large circular regions around Valles Marineris, Olympus Mons, and the Tharsis Montes, and 0.4 around Elysium Mons. There is a very smooth transition from those low values to higher values of about 0.6 in the southern uplands and about 0.8 in the northern lowlands.

The load correlation is -0.8 on most of the planet, but there are some exceptions. For example, an area around the Tharsis volcanoes has $r = 0.8$. Furthermore, large parts of the northern lowlands which also showed a strong positive correlation in the previous experiments have $r = 1$. Some areas close to the south pole have a relatively weak correlation of around 0.4. The latter is a feature which had not been observable in the previous experiments. Apart from that, the results for the load correlation mostly show an increased smoothing, as for the other parameters.

For the smoothness parameter ν, values below 0.7 are the most common. There are areas of $\nu = 1.3$ in the Argyre and Hellas basins, but most strikingly a large patch of $\nu = 1.6$ east and southeast of Hellas basin which is not associated with any particular topographic or crustal features.

The decorrelation distance ρ is also a lot smoother than in previous experiments. The southern uplands generally have a higher ρ than the rest of the planet, with many locations reaching the minimum value of $\rho = 0.05$. The variance σ^2 is significantly higher than for smaller cap sizes. This confirms the interpretation of the variance as a function of the maximum topographic difference between any two points within the localization

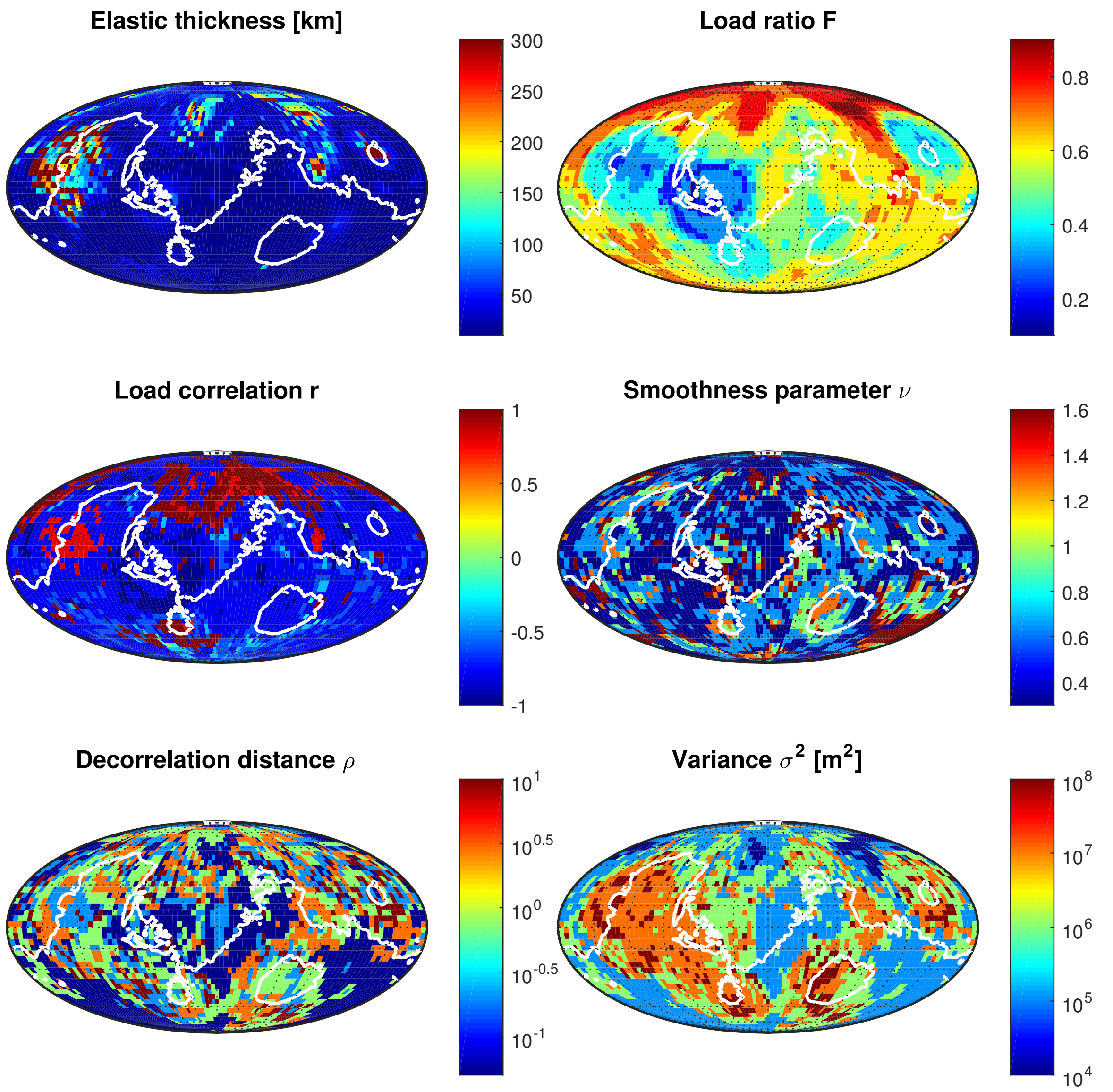

Figure 4.12: Maps of most likely solutions for the six estimation parameters created using the chordal Matérn covariance function and tapering with $K = 3$ tapers and a spherical cap size of $\theta_0 = 30°$. The elastic thickness map is identical to the one in Figure 4.11, but plotted again for better comparison.

window. Since the windows are much bigger with $\theta_0 = 30°$, the variance must also be bigger on average. The regions with the highest σ^2 are Tharsis, Elysium Mons, and all the large impact basins.

After describing the results for all the model parameters for the case of $K = 3$ tapers and a spherical cap size of $\theta_0 = 30°$, the conclusions drawn from the analysis of the elastic thickness results still hold. The large window makes the result significantly more smooth than previous experiments, but this also creates problems when placing the spherical cap on an area in which assumptions of homogeneity do not hold any more.

In total, the smoothing effect of the spherical cap size has become evident by analyzing results of different experiments. The impact of a change of the bandwidth is less clear, but a smaller bandwidth is definitely beneficial. For the interpretation of the results (Chapter 5) I will use two experiments: one with the smallest spherical cap size $\theta_0 = 10°$ and a bandwidth of $L_b = 35$ (Figure 4.6) and one with the largest spherical cap size $\theta_0 = 30°$ and a bandwidth of $L_b = 23$ (Figure 4.12). The former provides the most localized solutions, which is important in geologically inhomogeneous areas, such as in the vicinity of volcanoes, impact basins, and close to the dichotomy boundary. The latter provides the smoothest solution, which is beneficial in large homogeneous areas such as the northern lowlands and the southern uplands.

4.5. SIMULATION OF RANDOM FIELDS OF PLANETARY TOPOGRAPHY

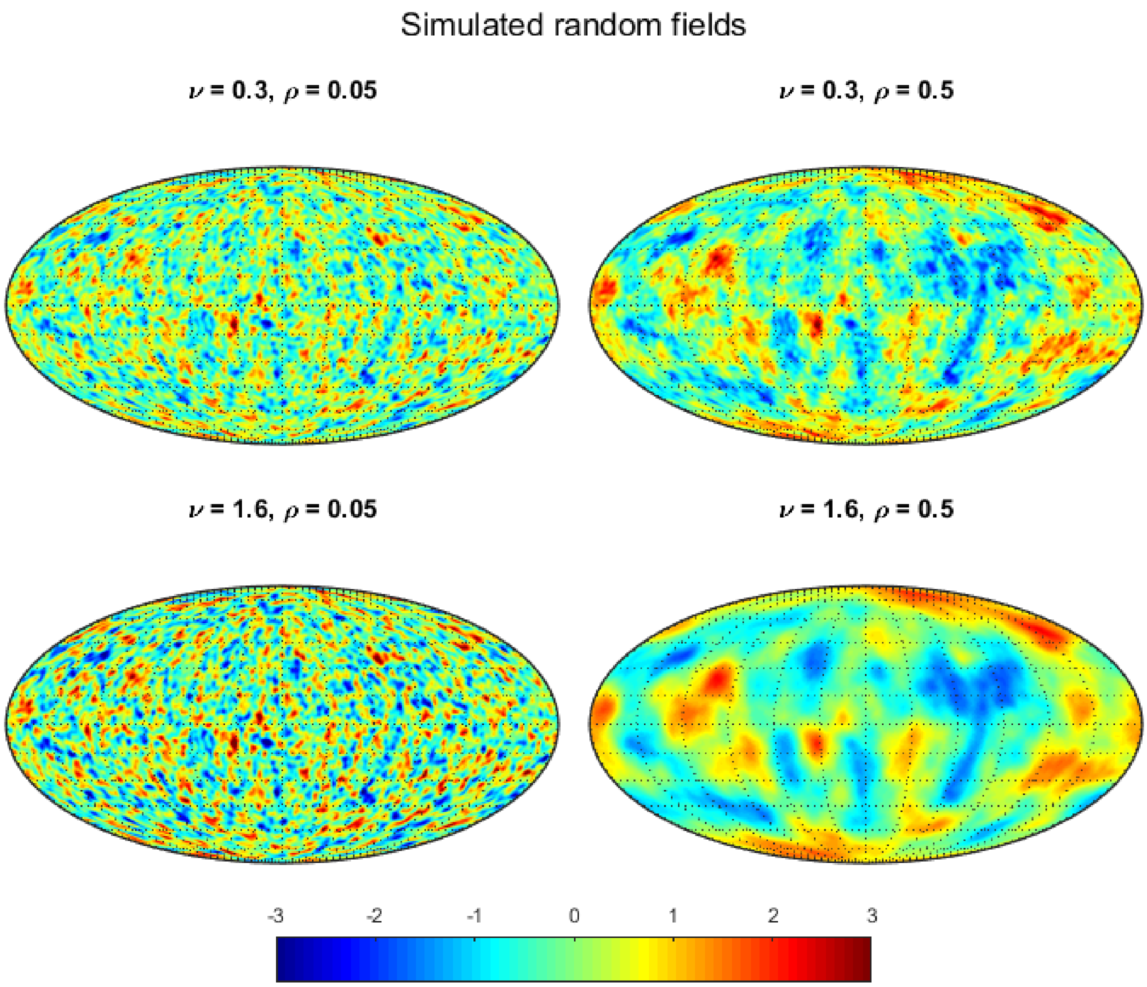

Figure 4.13: Simulated random fields for different values of smoothness ν and decorrelation distance ρ generated with the same set of random numbers. These fields are generated using the chordal Matérn covariance function and the variance is normalized to $\sigma^2 = 1$.

For the estimation of uncertainties of the six parameters which are output of the geophysical model, this study uses Monte Carlo simulation. The input for the Monte Carlo simulation are synthetically generated random fields of final surface and subsurface topography, which substitute the real observed and derived topographies. Before simulating random fields of final topography, I begin by simulating initial topographies to explore how well these match the behavior prescribed by the input parameters.
The initial surface topography is a function of the Matérn parameters smoothness ν, decorrelation distance ρ, and variance σ^2. The chordal Matérn covariance function as a function of great circle distance $M(\psi)$ (see Equation 3.64) is transformed in the spherical harmonic domain to give the covariance spectrum as a function of spherical harmonic degree and denominated as $S_{h^i h^i}(l)$. This covariance spectrum is used to generate random fields of initial surface topography according to Equation 3.77, and depends on the three Matérn parameters. Figure 4.13 shows that random fields with higher smoothness ν are indeed more smooth, and random fields with higher decorrelation distance ρ have larger distances between extreme values. I do not plot random fields for different values of the variance σ^2 because it simply acts as a factor.
It is expected that the experimental variogram of the simulated random field should approximate the chordal

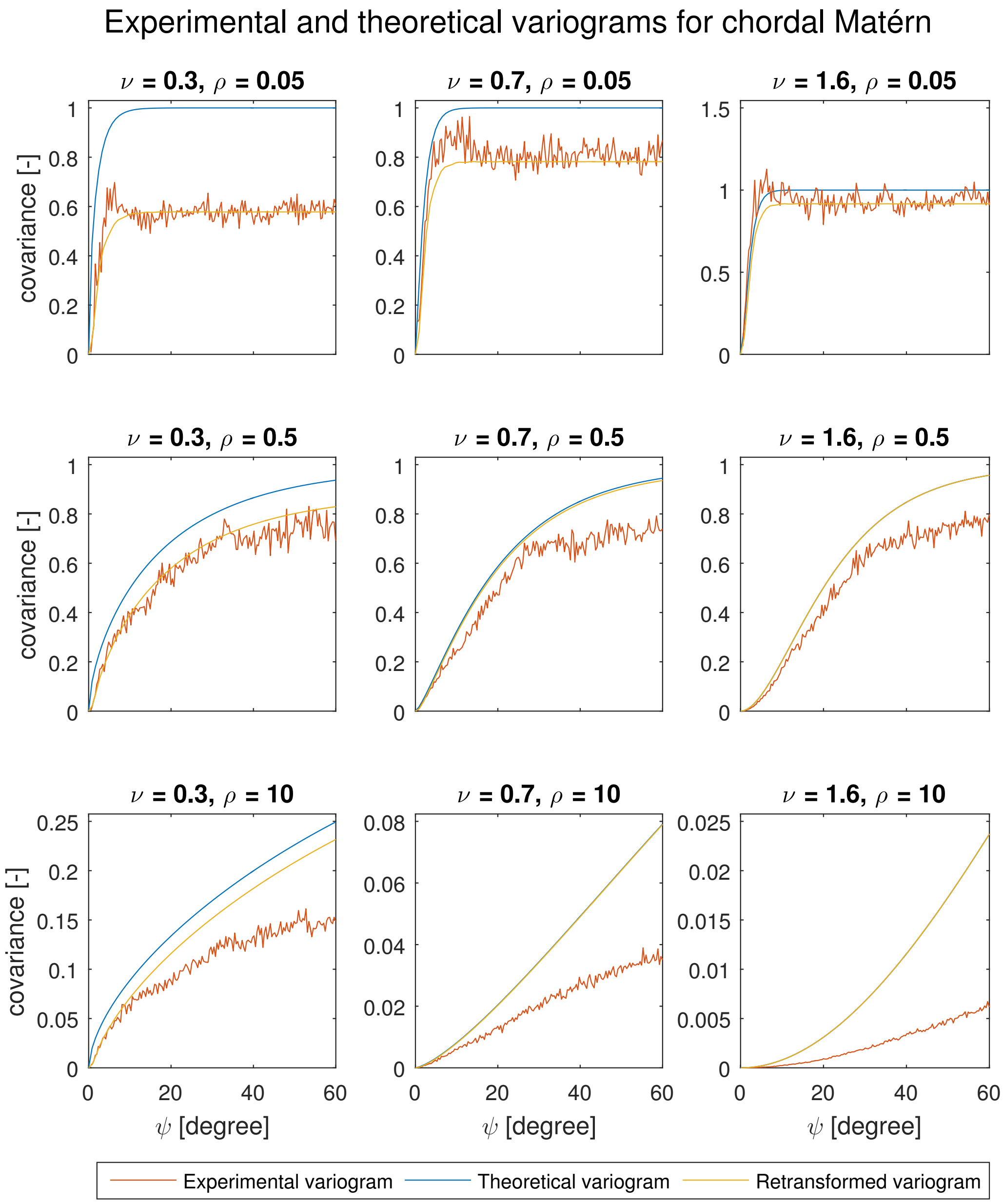

Figure 4.14: Comparison of theoretical variograms of the chordal Matérn covariance function with experimental variograms from simulated topography. The experimental variograms originate from topography which is simulated using the same parameters as for the plot of the theoretical variogram. The theoretical variograms are computed in the spatial domain. For the simulation of topographies spectral densities of the covariance are needed, so the variogram is transformed into the spherical harmonics domain. It is then also retransformed into the spatial domain and plotted here to show the loss of high frequency signal associated with this transformation. Plots represent various values of ν and ρ and are covariances normalized to $\sigma^2 = 1$. The theoretical and retransformed variograms are visually indistinguishable in the three plots in the lower right corner.

Matérn variogram with that specific set of parameters. Experimental variograms are created using the procedure described in Section 4.2 and the theoretical variogram of the chordal Matérn covariance function is just $\sigma^2 - M(\psi)$.

In some cases the experimental and theoretical variograms do not match well (Figure 4.14). For small values of smoothness and decorrelation distance ($\nu = 0.3$, $\rho = 0.05$; $\nu = 0.3$, $\rho = 0.5$; $\nu = 0.7$, $\rho = 0.05$) the experimental variogram, which is retrieved from the simulated topography, is significantly lower than the theoretical variogram. This is largely due to the necessary transformation of the covariance function into the spherical harmonics domain. The analytical form of the chordal Matérn covariance function, which can be evaluated

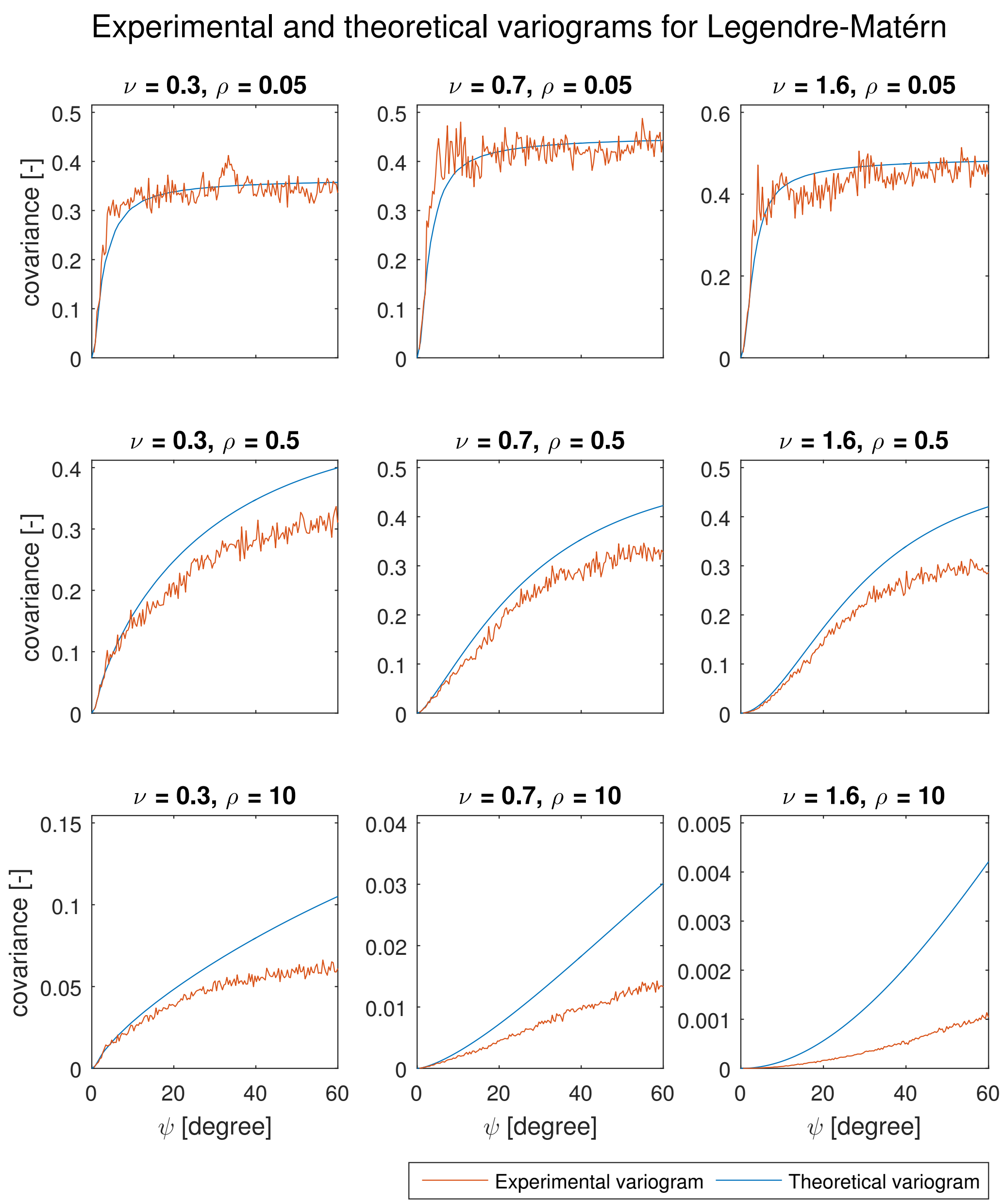

Figure 4.15: Comparison of theoretical variograms of the Legendre-Matérn covariance function with experimental variograms from simulated topography. The experimental variograms originate from topography which is simulated using the same parameters as for the plot of the theoretical variogram. The theoretical variograms are computed by transforming its spectral density into the spatial domain. Plots reprsent various values of ν and ρ and covariances are normalized to $\sigma^2 = 1$.

at different parameter values, is given in the spatial domain, but for the simulation of random fields its spectrum is required. It is therefore transformed into the spherical harmonics domain and coefficients up to degree $L = 100$ are evaluated, because this is also the degree to which real data exists in sufficient quality. A truncation error is induced through this truncation of the infinite sum of spherical harmonic coefficients (see also Section 4.2). For low values of smoothness and decorrelation distance, the variogram increases already close to the origin. This high frequency signal with a lot of power in the spherical harmonic degrees larger than $L = 100$ is lost in the transformation. When transforming the covariance spectrum back into the spatial domain, the peak at the origin of the resulting covariance is cut off. When the retransformed covariance is $M_{c,r}$, its variogram can be computed as $\max(M_{c,r}) - M_{c,r}$. This retransformed variogram is parallel to the true variogram with an offset equal to the truncation error shown in Figure 4.4. The experimental variograms match such retransformed variograms much better for a combination of low ν and ρ values (Figure 4.14), indicating that the actual simulation process performs well. Increasing the amount of evaluated spherical harmonics decreases the gap between theoretical and empirical variograms, but only at a very slow rate compared to the additionally needed computational expenses.

The quality of the fit generally becomes worse for increasing decorrelation distances ρ. For low decorrelation distance ($\rho = 0.05$) the experimental variogram generally fits the retransformed one very well. For $\rho = 0.5$, the experimental variogram is slightly lower than the retransformed one, but still generally a good fit, especially at small distances. For high decorrelation distances ($\rho = 10$), the fit is quite bad, although for low and moderate smoothness ($\nu = 0.3$, $\nu = 0.7$) it is still comparable up to a great circle distance of about 20°, which is the maximum value of relevance for all analyses that use a filter cap size of 10°. One should also note that the covariance generally rises very slowly for high values of ρ, especially in the case of $\rho = 10$, $\nu = 1.6$. This means that the topography signal only decorrelates very slowly, so that a mismatch between theoretical and experimental variogram might not be very relevant.

In conclusion, the simulation of random fields using the chordal Matérn covariance function with specified parameters causes problems for, firstly, a combination of low smoothness values and low decorrelation distances, and, secondly, for high decorrelation distances, which is why I go on to explore also the Legendre-Matérn covariance function.

When using the Legendre-Matérn covariance function to simulate the initial surface topography, there is no transformation to the spherical harmonic domain necessary, because its analytical form is already given in that domain. Accordingly, there are also no issues simulating topographies from variograms which have a low smoothness (Figure 4.15), and the experimental and theoretical variogram match very well for low decorrelation distance ρ. This behavior is because the theoretical variogram itself is an approximation, obtained by truncating the covariance spectrum at degree $L = 100$.

For higher values of the decorrelation distance an increasing mismatch, especially at large distances, is observed, and in this way the behavior of chordal and Legendre-Matérn covariance functions is very similar. Furthermore, the Legendre-Matérn variogram does not approach its variance σ^2 at large distances, which makes it harder to interpret (see Section 3.3). Still, I am going to use both covariance functions for the local error estimation procedure which follows to gain practical insights in the difference between their behavior.

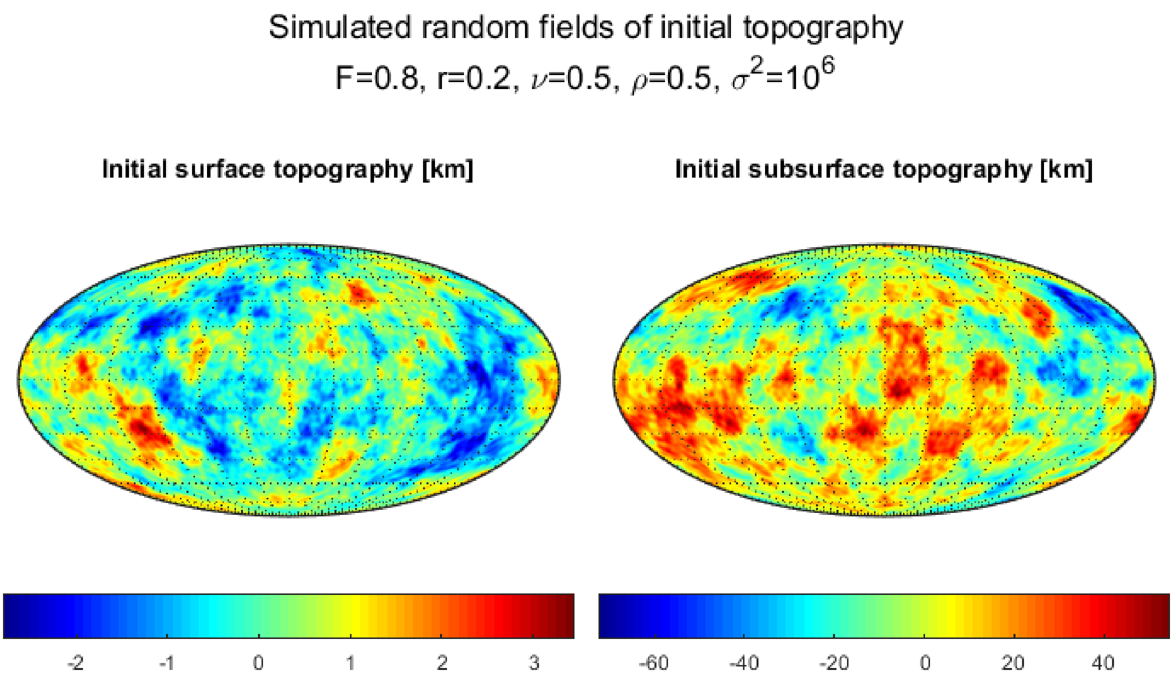

Figure 4.16: Simulated initial topographies with load ratio $F = 0.8$ and load correlation $r = 0.2$.

I have shown that synthetic random fields on the sphere can be generated whose behavior is governed by a covariance function of the chordal Matérn type. These function as initial surface topographies in my geophysical model of Mars. I now go on to investigate the simulation of a set of surface and subsurface topographies.

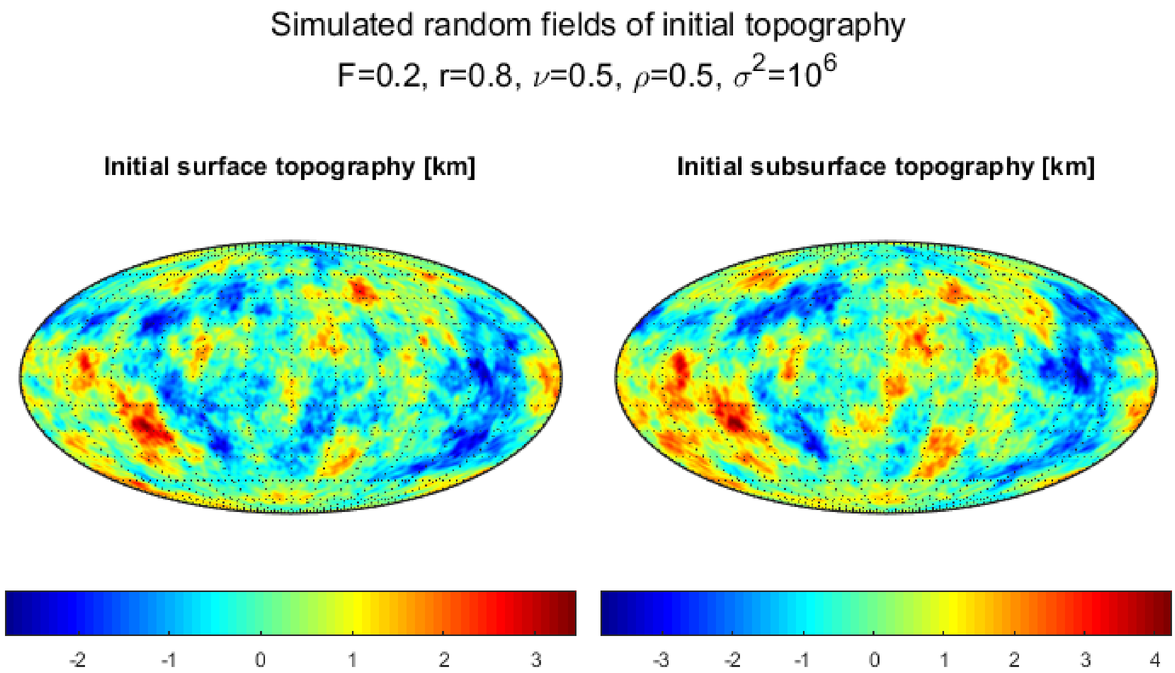

Figure 4.17: Simulated initial topographies with load ratio $F = 0.2$ and load correlation $r = 0.8$.

Random fields of initial subsurface topography can be generated using Equations 3.73 and 3.79. Figures 4.16 and 4.17 shows simulations of surface and subsurface topographies generated using the chordal Matérn covariance function. The load ratio F determines the amplitude of the subsurface topography. For low values most of the load is on the surface and the subsurface topography has a low amplitude. For high values most of the load is in the subsurface and the subsurface topography has a high amplitude. The load correlation r determines how correlated surface and subsurface topography are.

Not only the power spectra of the synthetic surface and subsurface topographies must match $S_{h^i h^i}$ and $S_{w^i w^i}$, respectively, but also the cross-power spectrum (Equation 3.43) of the simulated fields must correspond to its theoretical counterpart (Equation 3.74). Figure 4.18 compares the power spectrum densities and the cross-power spectrum density of simulated surface and subsurface topographies to curves generated from these equations and shows that they are indeed properly modelled.

So far, I have shown simulations of initial topographies and illustrated how the choice of model parameters influences the simulation results. However, for the Monte Carlo simulation of estimates of the model parameters, final topographies are needed as inputs, which have been generated using a specified set of parameters. These final topographies can be simulated using Equations 3.80 and 3.81, when their power spectrum is specified by the parameter set. Figure 4.19 shows simulated final surface and subsurface topographies which result from a flexural model with $T_e = 10\,\text{km}$. Such a low elastic thickness is equivalent to a very high degree of isostatic compensation. For this reason the two fields are almost perfectly anti-correlated. The difference in amplitude between surface and subsurface signal is closely related to crust and mantle densities.

Figure 4.20 shows simulated final surface and subsurface topographies which result from a flexural model with $T_e = 200\,\text{km}$. This value corresponds to a low degree of isostatic compensation. Neither surface nor subsurface topography are strongly influenced by any compensation process and after flexure they continue to be mostly uncorrelated.

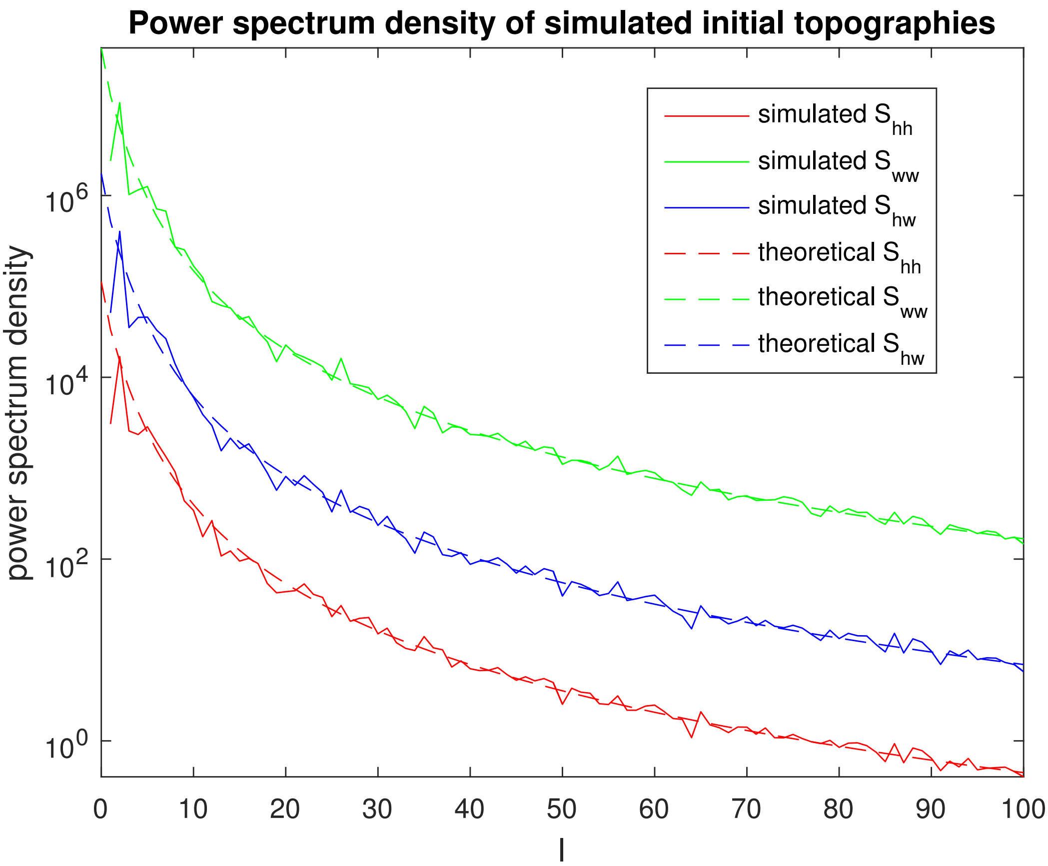

Figure 4.18: Power spectrum density of the simulated random fields of initial surface and subsurface topography and cross-spectrum density (solid lines) and the theoretical power spectrum densities (dashed lines). $r = 0.8$, $F = 0.8$.

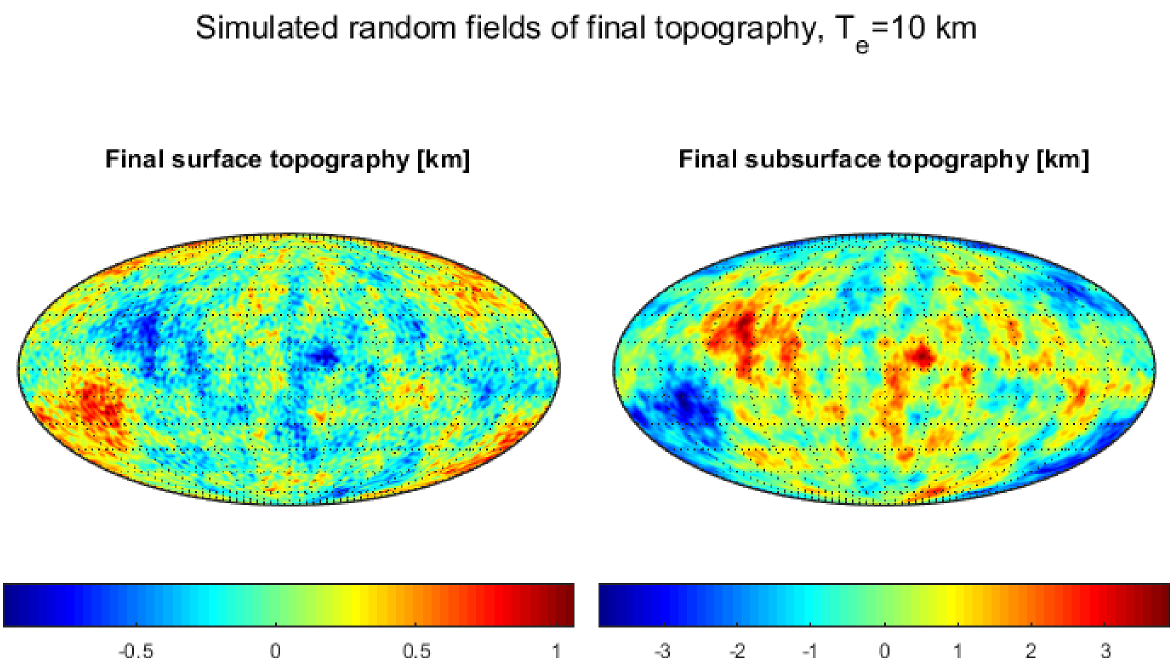

Figure 4.19: Simulated final topographies with elastic thickness $T_e = 10\,\text{km}$, initial load ratio $F = 0.2$, initial load correlation $r = 0.2$, and the chordal Matérn covariance parameters $\nu = 0.5$, $\rho = 0.5$, $\sigma^2 = 1\,\text{km}^2$.

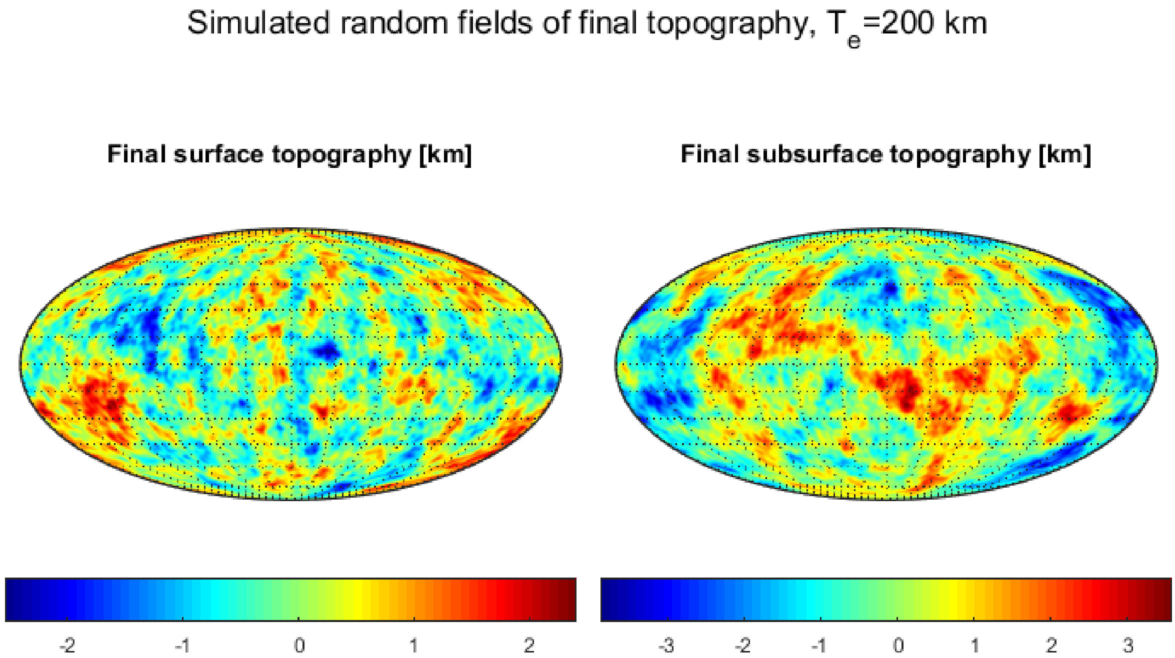

Figure 4.20: Simulated final topographies with elastic thickness $T_e = 200\,\text{km}$, initial load ratio $F = 0.2$, initial load correlation $r = 0.2$, and the chordal Matérn covariance parameters $\nu = 0.5$, $\rho = 0.5$, $\sigma^2 = 1\,\text{km}^2$.

4.6. LOCAL ANALYSIS OF THE ELASTIC THICKNESS

In Section 4.5, the results of simulations of planetary topography have been presented. It has been shown that planetary surface and subsurface topographies can be generated using a specific parameter set $\boldsymbol{y}$, although for certain combinations of the decorrelation distance ρ and the smoothness ν the results can be biased, especially at larger great circle distances. This is mainly a problem when applying tapers with large window sizes, for example $\theta_0 = 30°$, to the simulated topographies.

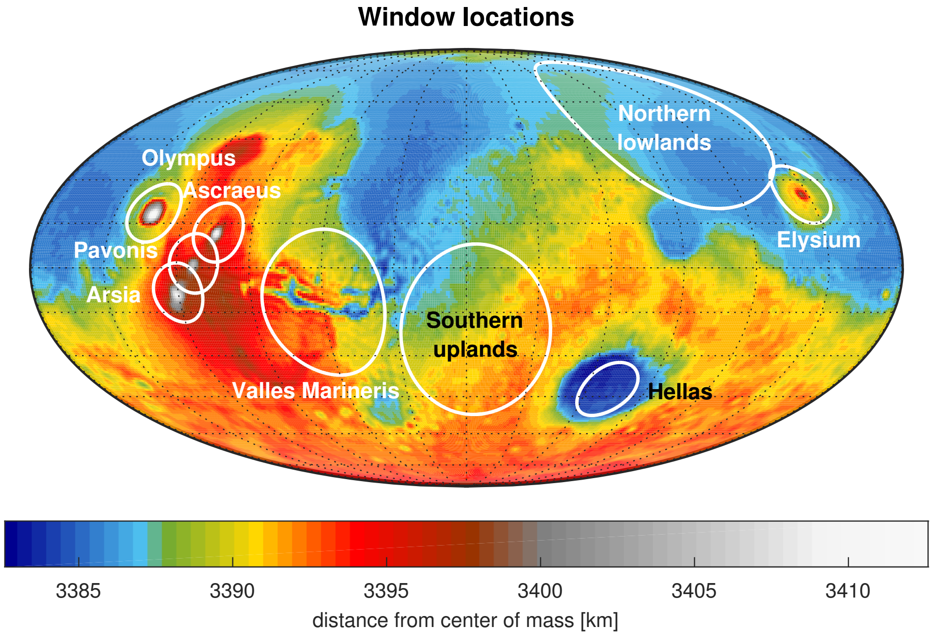

Figure 4.21: Position and size of the tapering windows used in this section superimposed on a map of the shape of Mars (see Figure 2.1).

The simulated topographies are needed for a Monte Carlo approach of determining the uncertainties in the estimated parameters, as described in Section 3.4. For a specific location a most likely parameter set is determined, which is then used to simulate 100 sets of synthetic topographies. Multitapering has to be applied to all of these 100 sets, thereby treating them the same way as the real data. Because of this, the error estimation procedure is computationally expensive. Therefore, I only apply it to several specific locations on Mars, namely the major Martian volcanoes (Olympus, Elysium, Ascraeus, Pavonis, and Arsia Montes), Hellas basin, Valles Marineris, and representative areas of the northern lowlands and southern uplands (see Figure 4.21 and Table 4.2).

Table 4.2: Overview of center points and radii of localization windows used in this study.

Location	Latitude ϕ	Longitude λ	θ_0	K	L_b
Olympus Mons	18.65°N	133.8°W	10	1	35
Elysium Mons	25.02°N	147.21°E	10	1	35
Ascraeus Mons	11.92°N	104.08°W	10	1	35
Pavonis Mons	1.48°N	112.96°W	10	1	35
Arsia Mons	8.35°S	120.09°W	10	1	35
Hellas basin	42.4°S	70.5°E	10	1	35
Valles Marineris	12°S	60°W	25	2	22
Northern lowlands	50°N	108°E	30	3	23
Southern uplands	22°S	4°E	30	3	23

In this section, I will treat these specific locations in the following way: First, I analyze the log-likelihoods of input parameter sets. Calculating the log-likelihood for every allowed combination of parameters (see Table 4.1) makes it possible to determine the most likely parameter set for any given location on Mars. In total,

n_{tot} = 412500 log-likelihood values are evaluated for each location. I only analyze planes in the six dimensional parameter space because I cannot analyze all the combinations of parameters in a rigorous manner. This method furthermore does not have much statistical significance. Second, I calculate for each location the formal error estimates from 100 sets of simulated topographies, as described in Section 3.4.

4.6.1. OLYMPUS MONS

The histogram of the log-likelihood values is given in Figure 4.22 for Olympus Mons. The highest log-likelihood value reached is -13.1. Over 50000 of the n_{tot} parameter sets have log-likelihoods above -20, concentrating about one eighth of the parameter sets in a very small range. Below -20, The number of values per bin declines quickly with decreasing log-likelihood. The lowest reached log-likelihood (not in the Figure) is in the order of -10^{30}. The histograms of all locations which have been investigated in this study show the same general trend. A significant part of the values is concentrated very close to the most likely value and the remaining values are widely spread out over the entire domain.

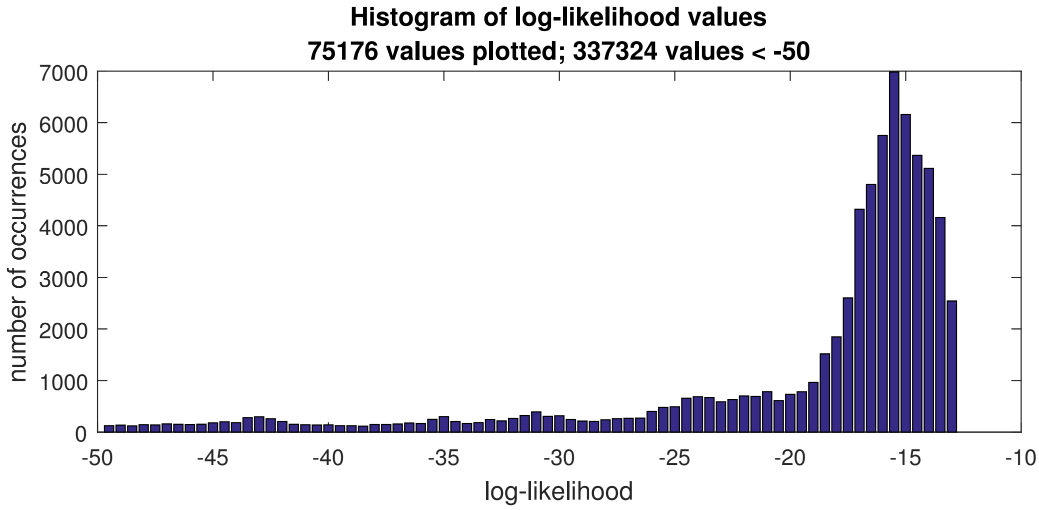

Figure 4.22: Histogram showing the distribution of log-likelihood values. Depicted are the log-likelihoods resulting from a localization to Olympus Mons with $K = 1$ taper and $\theta_0 = 10°$ using the chordal Matérn covariance function. The total number of log-likelihood values is $n_{tot} = 412500$, but only those with $\mathscr{L} > -50$ are depicted.

From this distribution of log-likelihood values, I conclude that many parameter sets are almost equally likely to have caused the observed topographies. Figure 4.23 shows how these very likely parameter sets are distributed, which allows to make some conclusions about how constrained the solution is. Blue color indicates combinations of parameters whose log-likelihood is not close to the maximum log-likelihood, and increasingly bright yellow color indicates increasingly more likely parameter sets. There is one value at $F = 0.5$, $r = -1$, which has white color. No value for this pixel could be determined because the multitapered covariance spectrum of final topographies $\bar{\boldsymbol{S}}_{\boldsymbol{hh}}(l, \boldsymbol{y})$ could not be inverted for at least one spherical harmonic degree l in the calculation of the log-likelihood (Equation 3.72) for this specific parameter set $\boldsymbol{y}$. This sometimes occurs for certain parameter sets and is a numerical artifact of the multitapering. The impact of these failures to invert the covariance spectrum is very limited because of the rarity of these events and because they apparently occur only for parameter sets which are unlikely in the first place.

At Olympus Mons, some parameters are quite well constrained: The load ratio $F = 0.2$, the decorrelation distance $\rho = 0.188$, and the variance $\sigma^2 = 10^8\,\mathrm{m}^2$, although ρ might also take lower, and F might also take higher values. The smoothness is less constrained. $\nu = 1.6$ is the most likely value, but all values of ν can be reached with $\mathscr{L} > -14$, which is very close to the maximum log-likelihood. T_e and r are even less constrained, with almost all values being able to reach log-likelihoods that are in Figure 4.23 indistinguishable from the maximum log-likelihood. Furthermore, there is some correlation between parameters. For example, a high value of ρ and a low value of ν can be just as likely as an intermediate value of ρ and a high value of ν. A similar correlation is visible between ρ and σ^2. This behavior is not surprising because it has been shown that different parameter sets can cause similar Matérn covariance curves, and also not concerning, because ultimately, I am not interested in an independent resolution of the Matérn parameters, but rather the elastic thickness.

It is very important to note that these findings are mere indications. From the log-likelihood, one can only

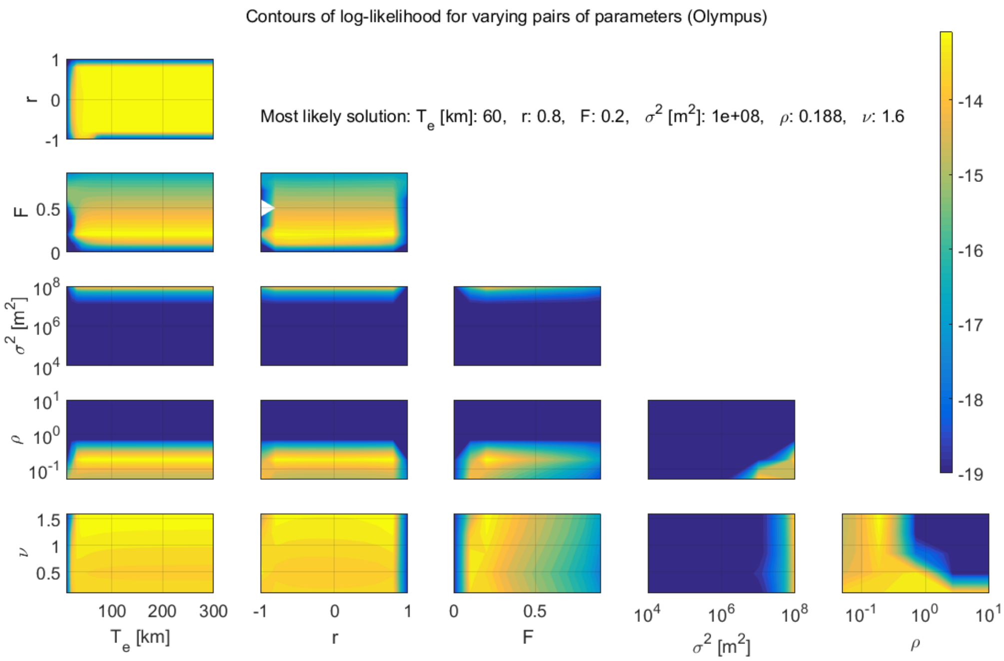

Figure 4.23: Contours of the log-likelihood $\mathscr{L}$ for varying pairs of parameters. Depicted are the log-likelihoods resulting from a localization to Olympus Mons with $K = 1$ taper and $\theta_0 = 10°$ using the chordal Matérn covariance function. Each plot is a slice though the six dimensional parameter space, holding four parameters fixed at their most likely value and varying the other two. The log-likelihood is cut off at -19 for better visibility, and because this is where the large peak in the histogram begins (see Figure 4.22).

draw conclusions about the relative likelihood of certain parameter sets, that is which parameter set is the most likely and if one parameter set is more or less likely than another. But with this simple analysis it is impossible to quantitatively evaluate the absolute likelihood of any parameter set, that is how much less likely than the most likely parameter set another specific parameter set is. Therefore, error estimates have been generated in a Monte Carlo process from synthetically generated topographies. These error estimates are not related to the observations, but are instead solely based on the specific parameter set which is used as an input. They therefore only describe the model behavior for that parameter set. I give both the contours of log-likelihood and the results of the Monte Carlo simulation because they complement each other. The contours of log-likelihood do not give formal errors and the Monte Carlo simulation does not work with the actual input data.

Table 4.3: Results of Monte Carlo error estimation using the most likely parameter set for Olympus Mons as an input (see Figure 4.23). 100 sets of final topographies are simulated, used as input for the maximum likelihood estimation procedure, and the mean and standard deviations of the 100 resulting most likely parameter sets are computed.

Parameter	Input	Mean	Standard deviation
Elastic thickness T_e [km]	60	70	89
Load ratio F	0.2	0.19	0.039
Load correlation r	0.8	-0.28	0.92
Smoothness parameter ν	1.6	0.69	0.47
Decorrelation distance ρ	0.188	0.59	1.5
Variance σ^2 [m^2]	10^8	$3.8 \cdot 10^7$	$4.2 \cdot 10^7$

Generating error estimates for the parameter set $\boldsymbol{y}$ which is most likely at Olympus Mons reveals significant bias in the model. The mean of the most likely T_e values is 10 km larger than the input value of 60 km. The three most common solutions are 30 km, 20 km, and 300 km, indicating a very badly constrained solution. Intermediate values barely occur in the 100 simulations. Out of the other parameters, only F could be reconstructed well. For the load correlation, there are no values of $-0.8 < r < 0.8$ in the 100 solutions, so that the mean is a bad representation of the actual distribution. Taking the mean and the standard deviation of the

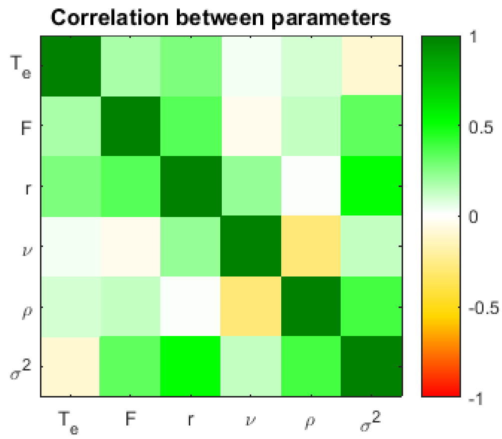

Figure 4.24: Correlations between the most likely parameter sets generated from 100 Monte Carlo simulations using the most likely parameter set for Olympus Mons (see Figure 4.23) as an input.

absolute value yields results which are much more constrained and less biased.
The smoothness is not constrained at all which was also indicated by the likelihood space (Figure 4.23). For the decorrelation distance, 0.188 is the value which occurs most often, but the mean value is much higher because of single occurrences of the highest value $\rho = 10$. The logarithmic spacing of the points at which the parameter space is sampled is heavily biasing the estimation. The same holds to an extent for the variance. All simulations either return the input value $\sigma = 10^8\,\mathrm{m}^2$ or the next lower value $\sigma^2 = 10^7\,\mathrm{m}^2$. A denser sampling would probably decrease the spread in this case.
The generation of 100 most likely parameter sets also allows the analysis of correlations between them (Figure 4.24). It confirms moderate correlations between ρ and the two other Matérn parameters, and uncovers a strong correlation between r and σ^2, while the correlation between the Matérn parameters and the other parameters is generally low. There are also moderate correlations between r and F and between r and T_e which might be concerning because an independent resolution of these parameters is important.
In conclusion, the error estimation confirms what has been shown by the likelihood contour plots: F, ρ and σ^2 are constrained considerably better than the other parameters. I attribute the large uncertainties of the error to three causes: firstly, the bias in the simulated topographies, which do not properly reflect their input parameters for very high ρ and for combinations of low ν and low ρ; secondly, the lack of constraint in the maximum likelihood estimation itself, which is caused by imperfections in the multitapering and the geophysical model; and thirdly, the coarse sampling of the parameter space, especially for the Matérn parameters.

4.6.2. Elysium Mons

At Elysium Mons (Figure 4.25), the elastic thickness is quite well constrained at 20 km and the Monte Carlo error estimation gives a value of 22 ± 4.3 km. Only when the load correlation r is not very strong, also higher elastic thicknesses are possible. The load ratio F is also well constrained at around 0.3, but slightly higher or lower values seem possible. The Monte Carlo simulation gives $F = 0.3 \pm 0.01$, indicating a very well constrained solution. The load correlation r is somewhat constrained to a strong correlation, but without a clear preference for positive or negative correlation. The Monte Carlo simulation always results in either $r = 1$ or $r = -1$.
The smoothness ν is quite constrained to the lowest value $\nu = 0.3$, except if ρ is low. There is a strong correlation between ρ and ν. Since ρ is also very unconstrained, the most likely parameter sets from the Monte Carlo simulation can take any values of ν and ρ. From the contours of log-likelihood, the variance seems very constrained to $\sigma^2 = 10^8\,\mathrm{m}^2$, but the Monte Carlo simulation gives an average of less than $10^7\,\mathrm{m}^2$, indicating large bias and uncertainty.
In conclusion, the elastic thickness and load ratio are low and quite constrained at Elysium Mons, but few meaningful statements can be made about the other parameters. The formal error estimation gives additional insights to what can be seen in the log-likelihood space.

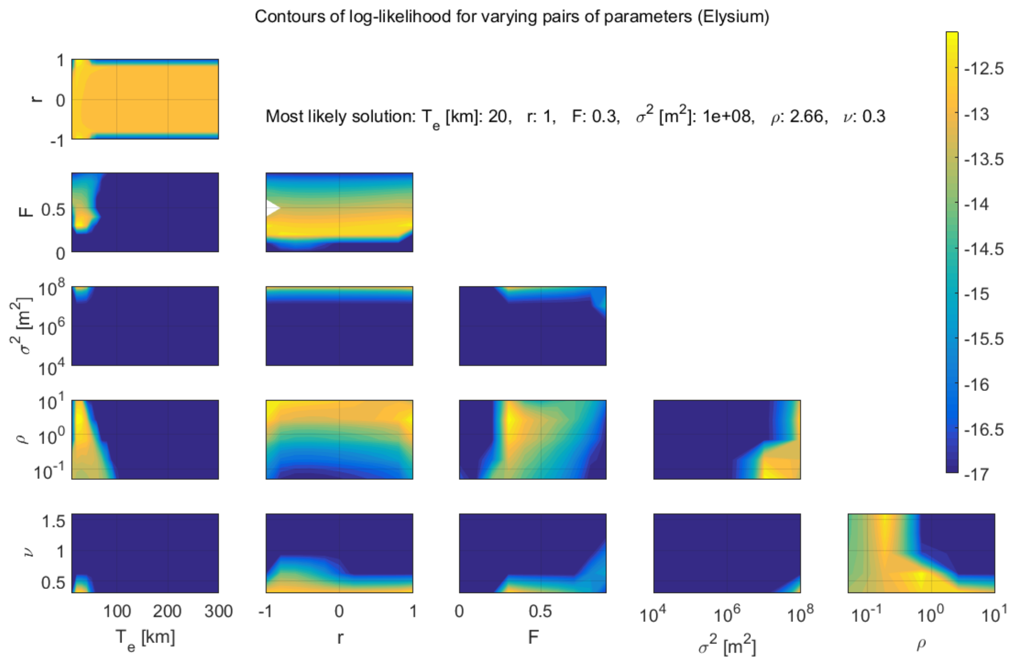

Figure 4.25: Contours of the log-likelihood $\mathscr{L}$ for varying pairs of parameters. Depicted are the log-likelihoods resulting from a localization to Elysium Mons with $K = 1$ taper and $\theta_0 = 10°$ using the chordal Matérn covariance function. Each plot is a slice though the six dimensional parameter space, holding four parameters fixed at their most likely value and varying the other two. The log-likelihood is cut off at -17 for better visibility.

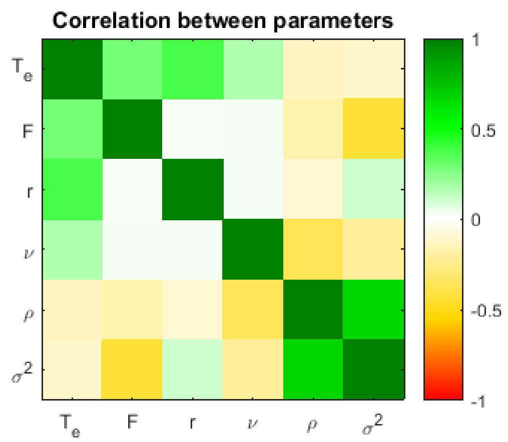

Figure 4.26: Correlations between the most likely parameter sets generated from 100 Monte Carlo simulations using the most likely parameter set for Elysium Mons (see Figure 4.25) as an input.

4.6.3. ASCRAEUS MONS

The most likely elastic thickness at Ascraeus Mons is $T_e = 30\,\text{km}$ (Figure 4.27). The Monte Carlo simulation gives $T_e = 41 \pm 13\,\text{km}$, indicating a rather constrained solution. In general the solution is very similar to the one for Elysium Mons. The load ratio is very well constrained with all of the 100 simulations resulting in the maximum likelihood solution $F = 0.1$. The other parameters are again very unconstrained. Interestingly, Figure 4.28 reveals that there are very little correlations between the geophysical parameters themselves and between the geophysical and the Matérn parameters. An exception from this is a strong correlation between r and ν.

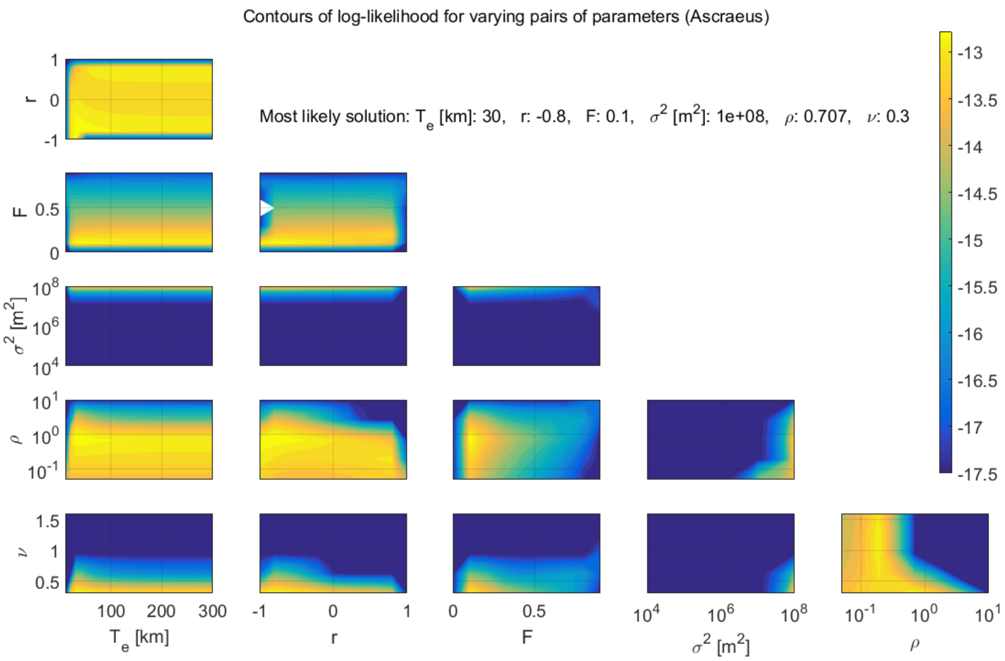

Figure 4.27: Contours of the log-likelihood $\mathscr{L}$ for varying pairs of parameters. Depicted are the log-likelihoods resulting from a localization to Ascraeus Mons with $K = 1$ taper and $\theta_0 = 10°$ using the chordal Matérn covariance function. Each plot is a slice though the six dimensional parameter space, holding four parameters fixed at their most likely value and varying the other two. The log-likelihood is cut off at -17.5 for better visibility.

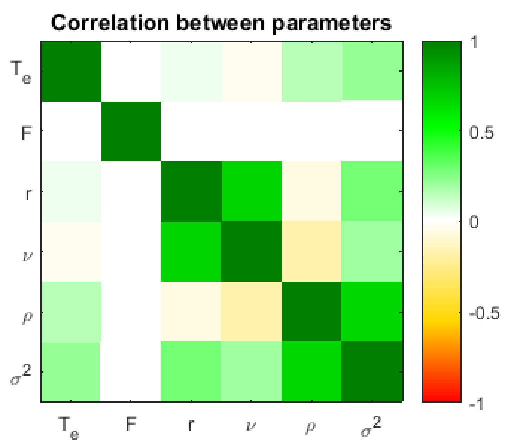

Figure 4.28: Correlations between the most likely parameter sets generated from 100 Monte Carlo simulations using the most likely parameter set for Ascraeus Mons (see Figure 4.27) as an input.

4.6.4. PAVONIS MONS

The most likely elastic thickness at Pavonis Mons is $T_e = 30$ km (Figure 4.29). The Monte Carlo simulation gives $T_e = 33 \pm 37$ km, indicating a moderately constrained solution. The load ratio is well constrained to 0.2 and the load correlation is strong, but it is unclear if the load correlation is positive or negative. The decorrelation distance is smaller than $\rho = 0.7$, and the variance larger than $\sigma^2 = 10^7\,\mathrm{m}^2$. The contours of the log-likelihood are not very clear on the smoothness, but the Monte Carlo simulation indicates that it is quite well constrained at $\nu = 0.3$.
The correlation is generally quite low at Pavonis Mons, so that the solution for this window is one of the most constrained ones.

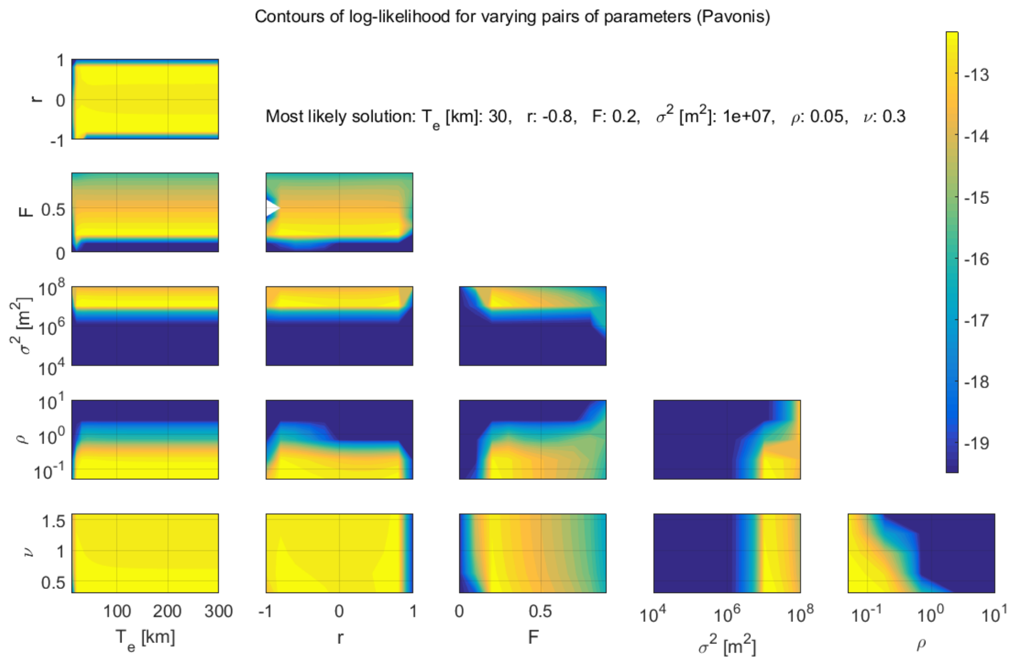

Figure 4.29: Contours of the log-likelihood $\mathscr{L}$ for varying pairs of parameters. Depicted are the log-likelihoods resulting from a localization to Pavonis Mons with $K = 1$ taper and $\theta_0 = 10°$ using the chordal Matérn covariance function. Each plot is a slice though the six dimensional parameter space, holding four parameters fixed at their most likely value and varying the other two. The log-likelihood is cut off at -19.5 for better visibility.

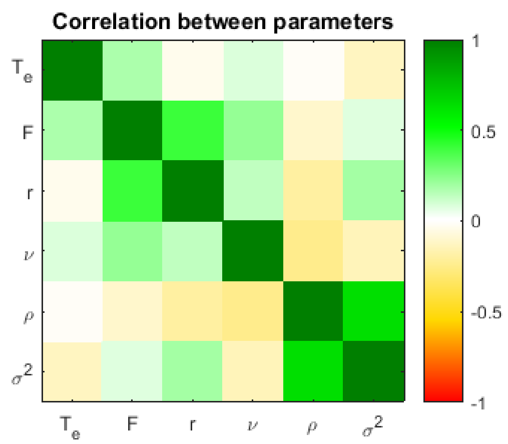

Figure 4.30: Correlations between the most likely parameter sets generated from 100 Monte Carlo simulations using the most likely parameter set for Pavonis Mons (see Figure 4.29) as an input.

4.6.5. ARSIA MONS

The most likely elastic thickness at Arsia Mons is $T_e = 40$ km (Figure 4.31). The Monte Carlo simulation gives $T_e = 36 \pm 49$ km, indicating a somewhat unconstrained solution. The most likely value for the load ratio is 0.3 and the Monte Carlo simulation gives $F = 0.25 \pm 0.06$. The load correlation is well constrained to strong correlation, but it is unclear if it is positive or negative. All the Matérn parameters are well constrained to their respective most likely values, although there is a significant correlation between ρ and σ^2 (Figure 4.32).

4.6.6. VALLES MARINERIS

For the analysis of Valles Marineris a considerably larger window was used than for the volcanoes. This is necessary because of the size of this feature which is barely completely included in this window of $\theta_0 = 25°$. The windows which were used to localize the Martian volcanoes were all focused on the peak and include

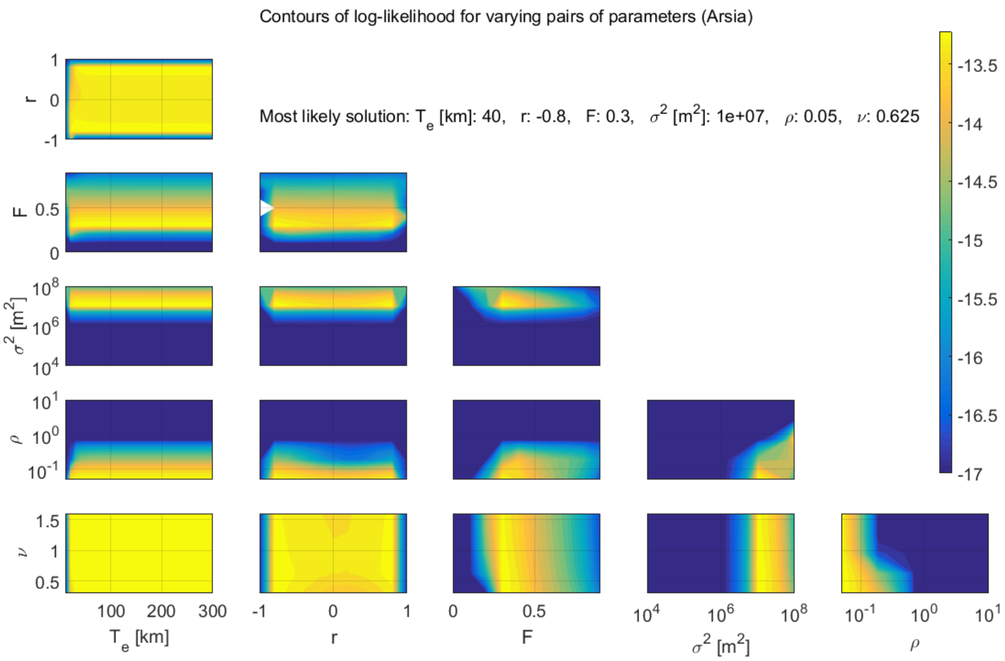

Figure 4.31: Contours of the log-likelihood $\mathscr{L}$ for varying pairs of parameters. Depicted are the log-likelihoods resulting from a localization to Arsia Mons with $K = 1$ taper and $\theta_0 = 10°$ using the chordal Matérn covariance function. Each plot is a slice though the six dimensional parameter space, holding four parameters fixed at their most likely value and varying the other two. The log-likelihood is cut off at -17 for better visibility.

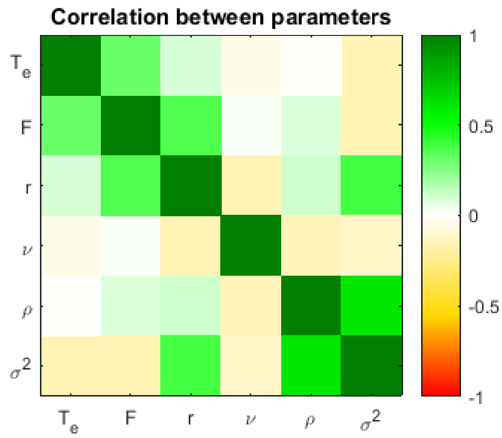

Figure 4.32: Correlations between the most likely parameter sets generated from 100 Monte Carlo simulations using the most likely parameter set for Arsia Mons (see Figure 4.31) as an input.

the volcano and some relatively homogeneous surrounding area. For the Tharsis Montes, the windows partly include parts of the neighboring volcanoes, and for Olympus Mons, some of the surrounding belongs to the northern lowlands, while other parts are in the Tharsis region. For Valles Marineris, it is not possible to focus the window on a peak because of the elongated shape of the feature. This shape is generally problematic because the model used in this study is isotropic and therefore cannot recognize elongated features as such. I use $K = 2$ tapers to receive a taper bandwidth $L_b = 22$ which is slightly lower than for all other windows applied in this study.
The most likely elastic thickness at Valles Marineris is 20 ± 3.7 km and the most likely load ratio is 0.2 ± 0.01 (Figure 4.33). The other values are similarly to the Martian volcanoes very unconstrained.

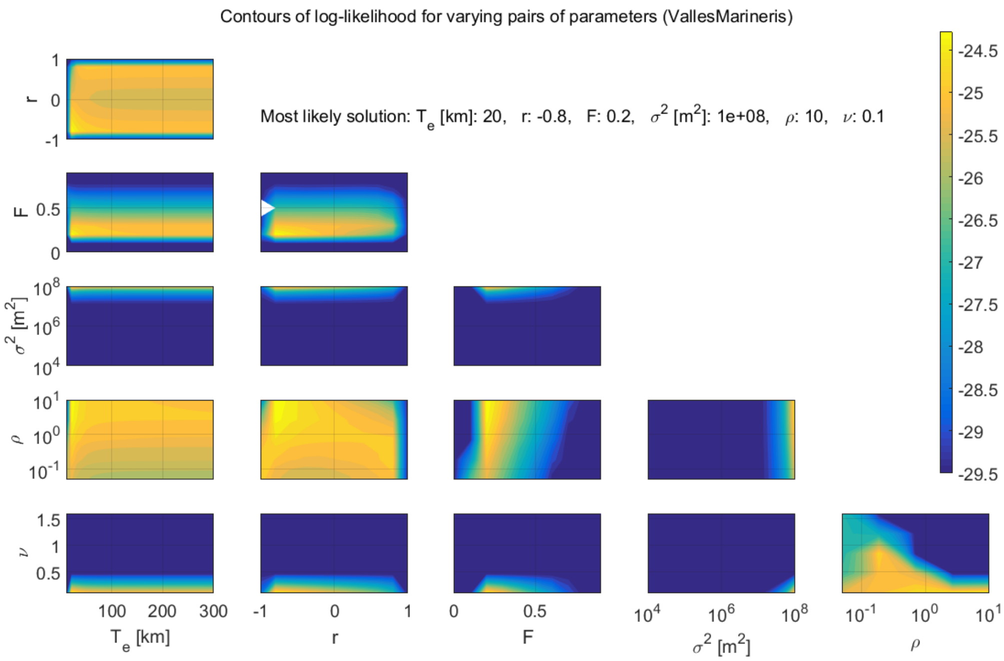

Figure 4.33: Contours of the log-likelihood $\mathscr{L}$ for varying pairs of parameters. Depicted are the log-likelihoods resulting from a localization to Valles Marineris with $K = 1$ taper and $\theta_0 = 10°$ using the chordal Matérn covariance function. Each plot is a slice though the six dimensional parameter space, holding four parameters fixed at their most likely value and varying the other two. The log-likelihood is cut off at -29.5 for better visibility.

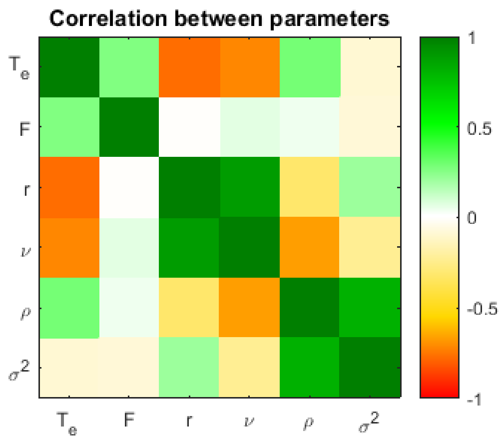

Figure 4.34: Correlations between the most likely parameter sets generated from 100 Monte Carlo simulations using the most likely parameter set for Valles Marineris (see Figure 4.33) as an input.

4.6.7. HELLAS BASIN

In the Hellas basin the elastic thickness is very low, with $T_e = 10$ km the most likely solution. The average of 100 Monte Carlo simulations is 14 ± 12 km. The load ratio is very well constrained, like for the other locations. r is also well constrained as a strong negative correlation. For ν, ρ, and σ^2, the lowest values are the most common ones retrieved from the Monte Carlo simulation, contrary to the likelihood space, which sees them unconstrained and favors intermediate values for ρ and σ^2, as does the most likely solution.

4.6.8. NORTHERN LOWLANDS

In this study, the northern lowlands are studied by applying a window to a representative region. A region has been chosen that is as homogeneous as possible and as large as possible at the same time. This region borders the dichotomy boundary in the south west, Elysium Mons in the south east, and the polar cap in the

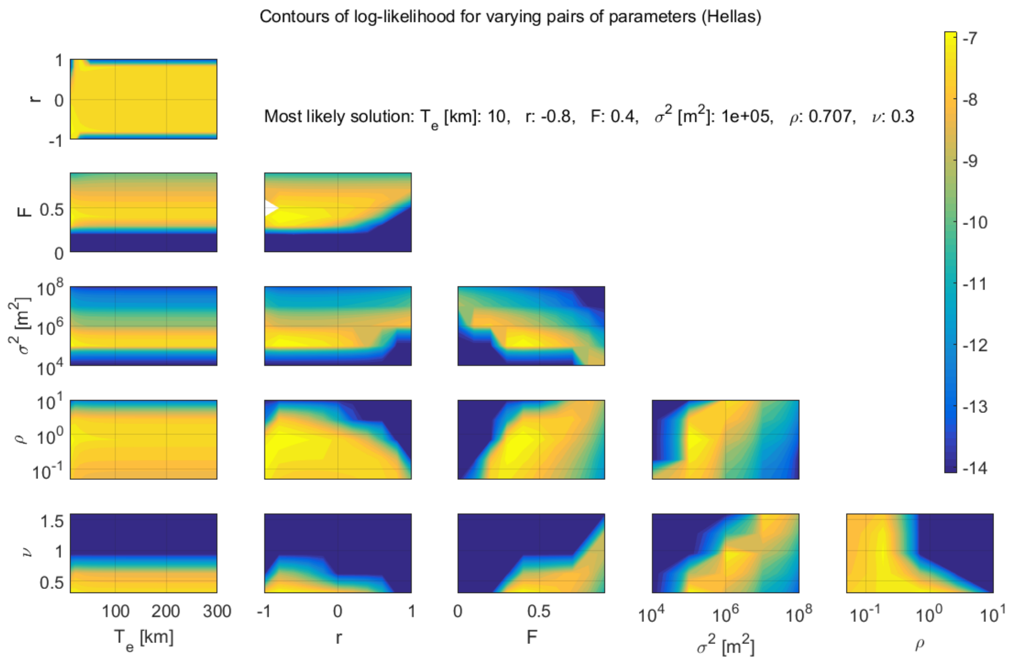

Figure 4.35: Contours of the log-likelihood $\mathscr{L}$ for varying pairs of parameters. Depicted are the log-likelihoods resulting from a localization to Hellas basin with $K = 1$ taper and $\theta_0 = 10°$ using the chordal Matérn covariance function. Each plot is a slice though the six dimensional parameter space, holding four parameters fixed at their most likely value and varying the other two. The log-likelihood is cut off at -14.1 for better visibility.

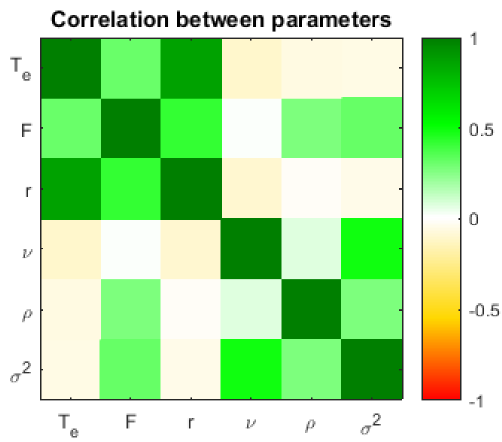

Figure 4.36: Correlations between the most likely parameter sets generated from 100 Monte Carlo simulations using the most likely parameter set for Hellas basin (see Figure 4.35) as an input.

north. The spherical cap size $\theta_0 = 30°$ allows for a bandwidth of $L_b = 23$ when $K = 3$ tapers are used. Other windows could have been chosen, for example between Elysium Mons and Tharsis or east of Tharsis, but the present one is the largest mostly homogeneous region.

The most likely elastic thickness value for this window is $T_e = 210$ km, which seems to be constrained only on the lower end for much lower values (Figure 4.37). The most likely T_e values from 100 simulations are bimodally distributed, the most common values are 60 km and 300 km. This leads to a formal error of 110 km which is very large. The load ratio is very constrained at $F = 0.9$ and r can be strongly positively or negatively correlated.

The smoothness and the variance are relatively constrained to $\nu = 0.3$ and $\sigma^2 = 10^4\,\mathrm{m}^2$, respectively, whereas the decorrelation distance ρ is unconstrained.

In the simulated most likely solutions, there is a strong correlation between all Matérn parameters, and es-

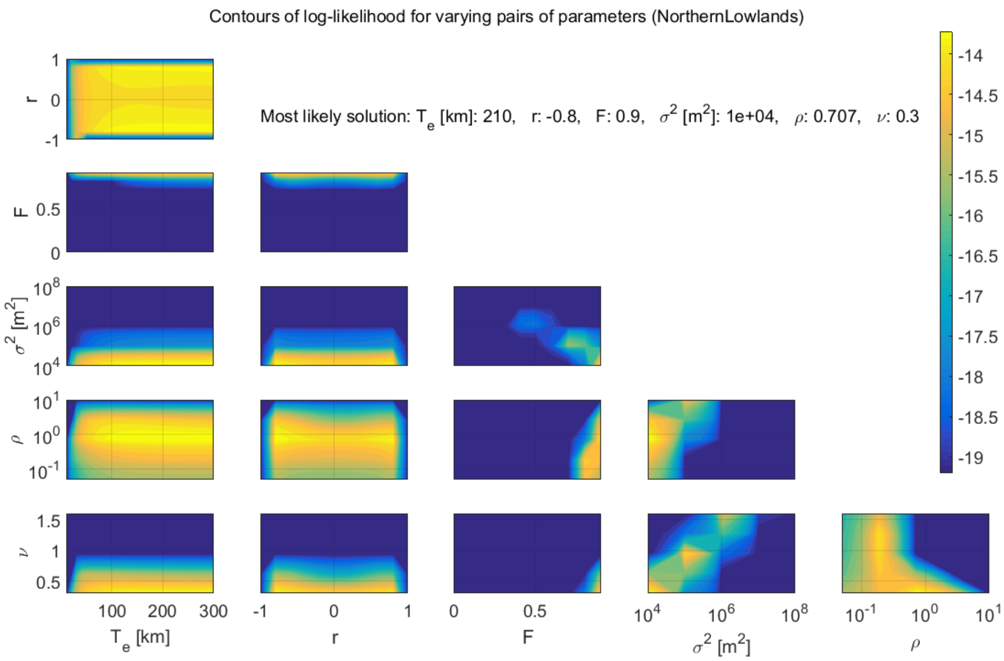

Figure 4.37: Contours of the log-likelihood $\mathscr{L}$ for varying pairs of parameters. Depicted are the log-likelihoods resulting from a localization to the northern lowlands with $K = 3$ tapers and $\theta_0 = 30°$ using the chordal Matérn covariance function. Each plot is a slice though the six dimensional parameter space, holding four parameters fixed at their most likely value and varying the other two. The log-likelihood is cut off at -19.2 for better visibility.

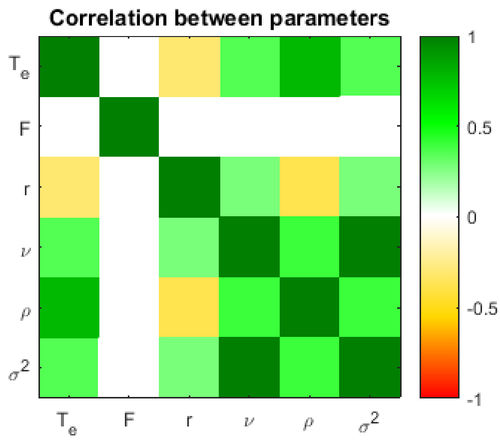

Figure 4.38: Correlations between the most likely parameter sets generated from 100 Monte Carlo simulations using the most likely parameter set for the northern lowlands (see Figure 4.37) as an input.

pecially between ν and σ^2, which are perfectly correlated. Strong correlations which are not indicated by the log-likelihood contours also exist between the elastic thickness and the Matérn parameters.

4.6.9. SOUTHERN UPLANDS

To study the southern uplands, a window was applied which borders Hellas basin in the south east, Argyre basin in the south west, and Valles Marineris in the north west. Again, different windows could have been chosen, but this is a large and homogeneous region which is sufficiently representative of the southern uplands.

The most likely elastic thickness value for this window is $T_e = 10\,\text{km}$ (Figure 4.39). The Monte Carlo simulation results in an estimation of $15 \pm 13\,\text{km}$, which indicates quite a good constraint. The load ratio is well constrained at $F = 0.5$. r is clearly constrained as a strong negative correlation.

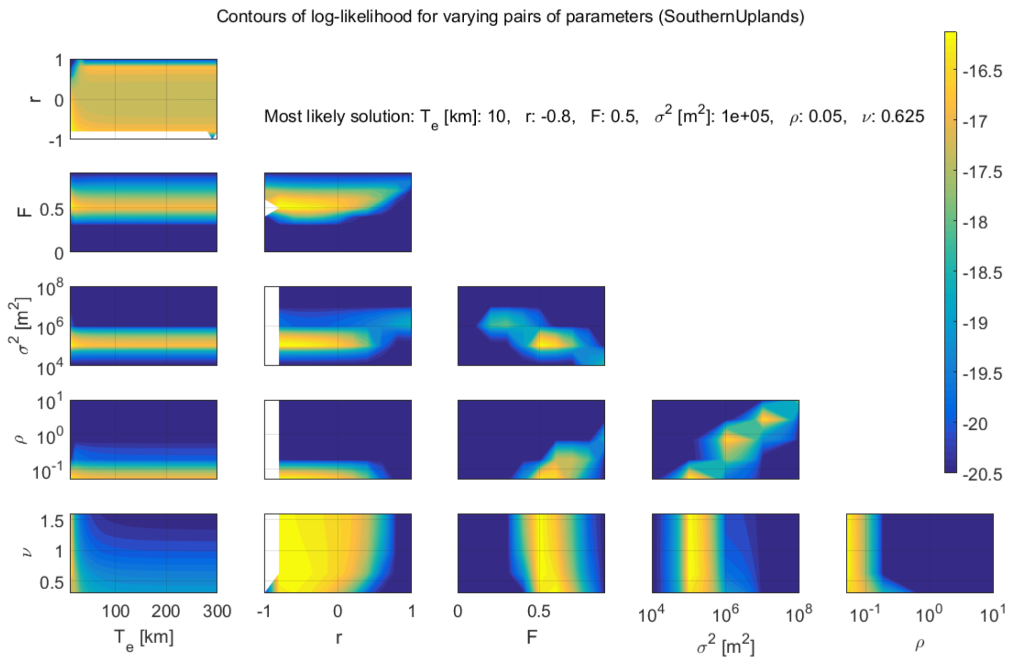

Figure 4.39: Contours of the log-likelihood $\mathscr{L}$ for varying pairs of parameters. Depicted are the log-likelihoods resulting from a localization to the southern uplands with $K = 3$ tapers and $\theta_0 = 30°$ using the chordal Matérn covariance function. Each plot is a slice though the six dimensional parameter space, holding four parameters fixed at their most likely value and varying the other two. The log-likelihood is cut off at -20.5 for better visibility.

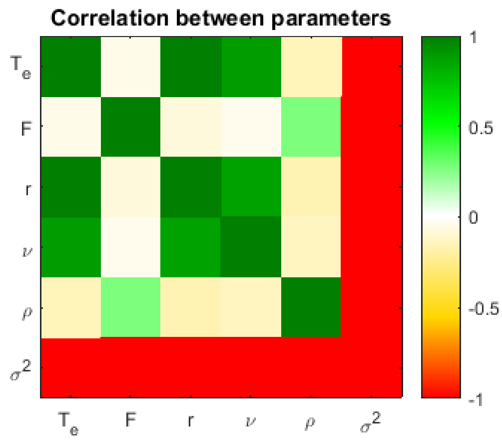

Figure 4.40: Correlations between the most likely parameter sets generated from 100 Monte Carlo simulations using the most likely parameter set for the southern uplands (see Figure 4.39) as an input.

All Matérn parameters are quite well constrained too, but there are are strong correlations between the smoothness, the elastic thickness, and the load correlation (Figure 4.40). The variance shows up as having perfect negative correlations with all other parameters because all 100 Monte Carlo simulations give $\sigma^2 = 10^5\,\text{m}^2$.

4.6.10. CONCLUSIONS

In this section, I have given the parameter sets which are most likely to have caused the observed surface and subsurface topographies for localizations to nine windows representing specific geologic features of Mars. Furthermore, I have for each window analyzed the distribution of log-likelihoods in the six dimensional parameter space, and compared the findings to the results of 100 Monte Carlo simulations which used the most likely parameter set as an input.

An overview of the results for the geophysical parameters is given in Table 4.4. The elastic thickness could

Table 4.4: Summary of most likely solutions for elastic thickness, load ratio, and load correlation for the nine windows analyzed in this study. Accuracies are not given for r because of its bimodal distribution in the Monte Carlo simulations.

Location	Elastic thickness T_e[km]		Load ratio F		Load correlation r
	Most likely value	Error	Most likely value	Error	Most likely value
Olympus Mons	60	89	0.2	0.04	0.8
Elysium Mons	20	4.3	0.3	0.01	1
Ascraeus Mons	30	13	0.1	0	-0.8
Pavonis Mons	30	37	0.2	0.04	-0.8
Arsia Mons	40	49	0.3	0.06	-0.8
Valles Marineris	20	3.7	0.2	0.01	-0.8
Hellas basin	10	12	0.4	0.04	-0.8
Northern lowlands	210	110	0.9	0	-0.8
Southern uplands	10	13	0.5	0.01	-0.8

be constrained well for several locations: Elysium Mons, Ascraeus Mons, Valles Marineris, Hellas basin, and the southern uplands. In all of these locations, the most likely elastic thickness is 30 km or lower. T_e is most unconstrained in the windows of Olympus Mons and the northern lowlands, which also have the highest T_e estimates.

The load ratio F is extremely well constrained for all locations.

The estimation of r is problematic because the model fails to distinguish between positive and negative correlation. When simulating topographies from a certain parameter set with given strong positive load correlation r, the most likely load correlation retrieved from these topographies is about equally likely to be positive or negative, and vice versa. The log-likelihoods of strong positive and negative load correlation are also almost the same.

The Matérn parameters are usually not constrained well. This is not a problem as long as it is a cause of strong mutual correlations rather than strong correlations with the other parameters because determining the Matérn parameters is not the goal of this study.

However, sometimes there are significant mutual correlations between the geophysical parameters and correlations between the geophysical and the Matérn parameters. Such correlations are problematic because they indicate that the parameters of interest are not independently resolvable.

4.7. THE LEGENDRE-MATÉRN COVARIANCE MODEL

All previous experiments have used the chordal Matérn covariance function (Equation 3.64) to determine a most likely parameter set for each location on Mars. For comparison, I also investigate the performance of the Legendre-Matérn covariance function (Equation 3.69) for $K = 1$ taper and a spherical cap size of $\theta_0 = 10°$. These tapering parameters are the same as the ones used in Section 4.3 and should therefore produce very similar results.

Figure 4.41 shows that this is indeed the case. The general trends are the same as in Figure 4.5. However, the values of individual locations can differ a lot. This is especially visible in the high T_e areas in the northern lowlands where both maps show a similar distribution of values ranging from 50 km to 300 km, but single pixels can differ by 250 km and more between the two experiments. This is a further indication of poorly constrained solutions in those areas. All the significant trends described previously for the solution using the chordal Matérn covariance function still fully hold.

The same is also true for the F, r, and ν parameters (Figure 4.42), with a very slight increase in noise when using the Legendre-Matérn as opposed to the chordal Matérn covariance function.

The behavior is different for the decorrelation distance. In the experiment using the Legendre-Matérn covariance function, values of ρ ranging from 0.05 to 10 are scattered over the whole map, with no clear regional differences visible.

The map of σ^2 shows globally higher values by about half a power of ten compared to the chordal Matérn map. I interpret the differences in ρ and σ as results of the different parametrizations.

To illustrate the differences which occur between the solutions from the two covariance function, the localized results for Olympus Mons are compared. Contours of the log-likelihood generated from the Legendre-Matérn covariance function are given in Figure 4.43. The general pattern of the log-likelihood surfaces is

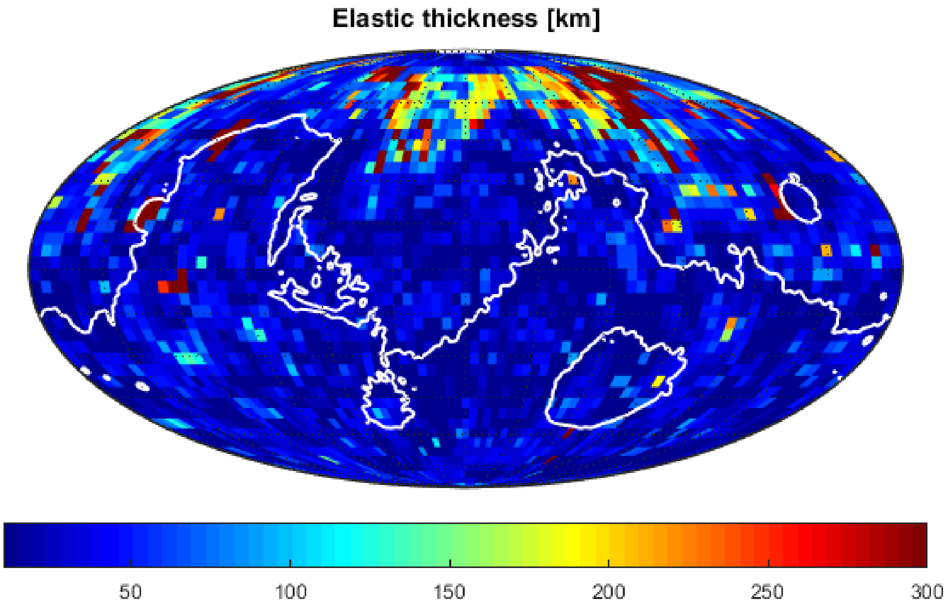

Figure 4.41: Map of the elastic thickness of Mars created using the Legendre-Matérn covariance function and tapering with $K = 1$ tapers and a spherical cap size of $\theta_0 = 10°$.

very similar to the one for the chordal Matérn covariance function (Figure 4.23). The most likely solution, however, is quite different, finding $T_e = 300$ km as the most likely value, while the other parameters are the same, except for ν, which is most likely to be 1.6 using the chordal Matérn covariance function and 0.85 using the Legendre-Matérn covariance function. The Monte Carlo simulations give almost the same result for both covariance functions: 70 ± 89 km for the chordal Matérn covariance function, and 64 ± 85 km for the Legendre-Matérn covariance function. The latter result indicates a very unconstrained solution once again. Even when entering $T_e = 300$ km as an input to the Monte Carlo simulations, the average of 100 solutions is only 64 km. This bias is caused by a large number of most likely solutions which are around 30 km.

The correlations between the Matérn parameters are higher when using the Legendre-Matérn covariance function (see Figures 4.44 and 4.24). This corresponds to the observation of more scattered most likely solutions in the map of Matérn parameters (Figure 4.42) and is an argument in favor of using the chordal Matérn covariance function.

In conclusion, the principal parameters of interest, T_e, F, and r, are not meaningfully affected by the choice of covariance function, indicating that both are valid options for modelling the initial surface topography. This holds true even though large local differences can be encountered for the most likely solution of the elastic thickness because these differences are within the normal uncertainty of the solutions, which is found when applying either of the covariance functions. I continue to focus my investigations on the chordal Matérn covariance function because of its better interpretability and for consistency.

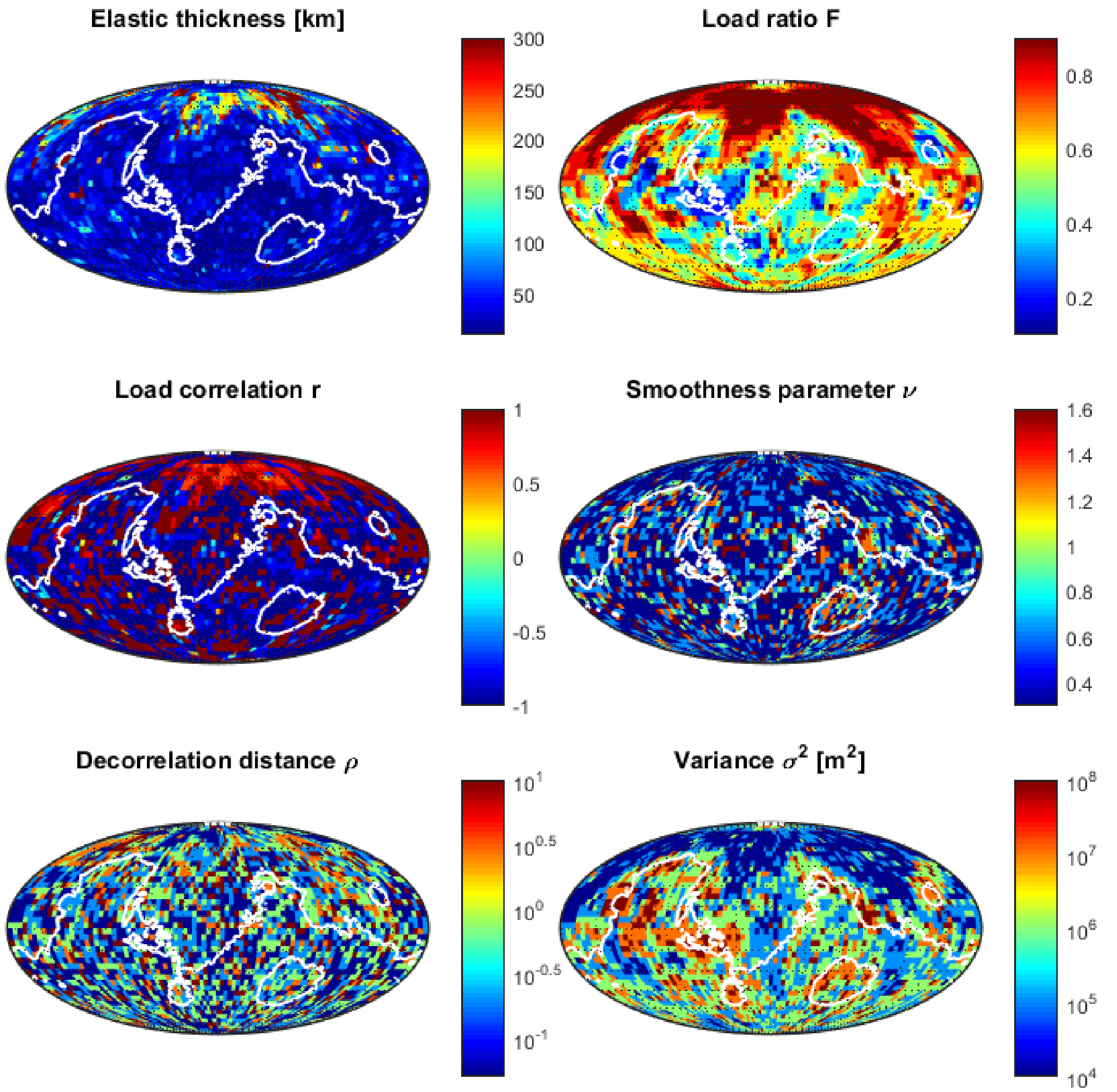

Figure 4.42: Maps of most likely solutions for the six estimation parameters created using the Legendre-Matérn covariance function and tapering with $K = 1$ tapers and a spherical cap size of $\theta_0 = 10°$. The elastic thickness map is identical to the one in Figure 4.41, but plotted again for better comparison.

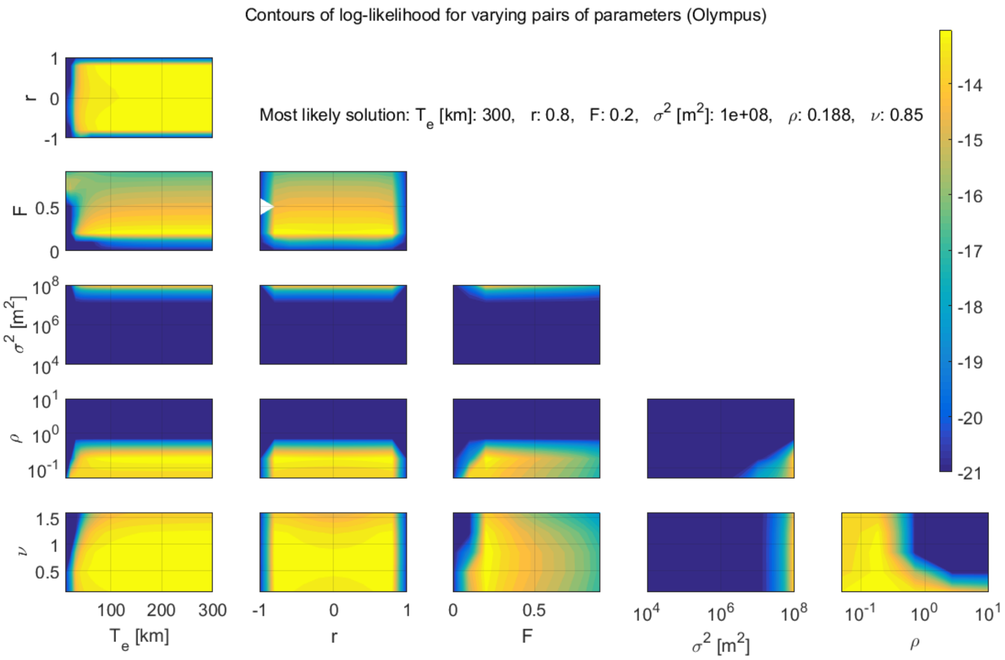

Figure 4.43: Contours of the log-likelihood $\mathscr{L}$ for varying pairs of parameters. Depicted are the log-likelihoods resulting from a localization to Olympus Mons with $K = 1$ taper and $\theta_0 = 10°$ using the Legendre-Matérn covariance function. Each plot is a slice though the six dimensional parameter space, holding four parameters fixed at their most likely value and varying the other two. The log-likelihood is cut off at -21 for better visibility.

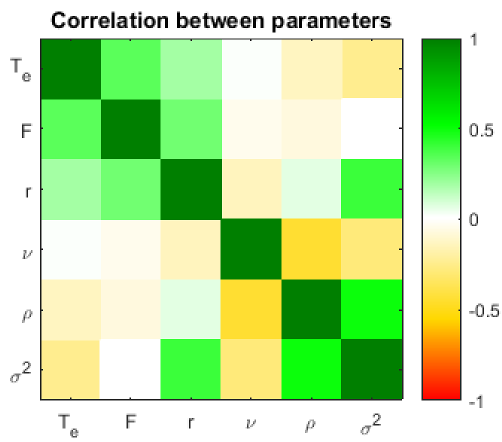

Figure 4.44: Correlations between the most likely parameter sets generated from 100 Monte Carlo simulations using the most likely parameter set for Olympus Mons (see Figure 4.43) as an input and the Legendre-Matérn covariance function.

5

Discussion

Maps of the elastic thickness, initial load ratio, initial load correlation, and the Matérn parameters have been presented which demonstrate that estimating these parameters on a global scale is generally possible. The resulting low elastic thickness in the southern uplands and high elastic thickness at the major volcanoes and in the northern lowlands correspond to the findings of previous studies (e.g. Audet, 2014; Belleguic et al., 2005; McGovern et al., 2004; Zuber et al., 2000). For many locations on Mars, however, the results are very unconstrained.

Nevertheless, this is a remarkable result, because it has been achieved using a novel method: maximum likelihood estimation in the framework proposed by Simons and Olhede (2013). This study on real data could not confirm all the conclusions made by Simons and Olhede (2013) on synthetic data. Especially for high values of T_e, the solutions are not well constrained, and significant correlations between the parameters exist, making it sometimes impossible to resolve them individually.

In this chapter, I will first discuss the geological implications from my results and compare them to previous results. I will then continue to analyze the implications which my results have for the methodology of maximum likelihood estimation of the elastic thickness.

5.1. Southern uplands and Hellas basin

In the southern uplands, the surface is heavily cratered (Figure 2.1) and strongly negatively correlated with the subsurface topography (Figure 4.1). This already indicates a high degree of isostatic compensation which is confirmed by the low elastic thickness values of 10 km in this area (Figure 4.11, Table 4.4). The large amount of craters also implies Noachian and Hesperian surface ages in the southern uplands. At 2.9 to 4.1 Ga, these are in fact the oldest surfaces on Mars (Carr and Head, 2010; Zuber et al., 2000). The crust stabilized early in the history of Mars when the upper layers of Mars were still very hot and could not support big loads, which also supports the observation of a low elastic thickness. Even though the Hellas and Argyre basins are very significant surface features, these conclusions also hold there, including the very low elastic thickness estimates.

The initial load ratio F and initial load correlation r give the properties of the distribution of top and bottom loads before flexure. In the southern uplands, F has most likely values of about 0.5, which corresponds to the current load ratio. The value 0.5 means that top and bottom loads are equal which is the case in full isostatic compensation. Also r, which is -0.8 at most locations, indicates negative correlation, which is currently the case. This is a general problem of the model. For high degrees of isostatic compensation, the initial state of the lithosphere before flexure becomes very hard to retrieve. For $T_e = 0\,\text{km}$, there will always be a perfect local equilibrium between top and bottom loads regardless of the load ratio and load correlation.

The most likely elastic thickness values compare favorably with the results of previous studies. Zuber et al. (2000) obtained a best fit elastic thickness of 0 to 20 km for the southern uplands and Hellas basin from forward modelling. McKenzie et al. (2002) found a best-fit value $T_e = 14.5\,\text{km}$ from measurements of line of sight velocity. Audet (2014) obtained best fit elastic thickness values with his spherical wavelet method that are generally below 45 km in the southern uplands, although no solutions could be obtained for large regions around Hellas basin. His results for using free-air or Bouguer admittance and coherence do not differ much.

While these results are significantly higher than those found in this study and in previous studies, they are the lowest values on the planet he retrieved. He also solved for the load ratio, which takes values between 0.2 and 0.4 in the southern uplands. It is noteworthy that he finds a significant increase in T_e around the Argyre basin, a feature which does not stand out in this study. The discrepancies between the results of Audet (2014) and this study might be explained by the different models. Apart from using a wavelet approach, Audet (2014) also used a fixed $r = 0$ and did not properly take into account finite-amplitude effects. McGovern et al. (2004) generally obtained values below 20 km for this region with models that do not include bottom loading. At one location at 64°S, 66°E in Malea Planum, which they denominate as the southern Hellas rim, they find high T_e values of up to 120 km when including some bottom loading up to $f = 0.4$, which is equivalent to $F = 0.3$ (see Equation 1.5). While this study's most likely solution for this location exhibits the same low elastic thickness as in the rest of the southern uplands, there are some pixels very close at 60°S, 60°E in Malea Planum whose most likely elastic thickness values are 300 km for $\theta_0 = 10°$ (Figure 4.5) or 90 to 120 km for $\theta_0 = 30°$ (Figure 4.11).

5.2. NORTHERN LOWLANDS

The $\theta_0 = 30°$ window applied to a representative location at 50°N 108°E in the northern lowlands gives a most likely elastic thickness of 210 km. There are several indications that this value is very unconstrained. The log-likelihood contours (Figure 4.37) show that all values above 80 km have very similar log-likelihoods. Also, the Monte Carlo simulations have resulted in a formal standard deviation of 100 km and the spatial distribution of most likely T_e values (Figure 4.11) is quite inhomogeneous in the area, with elastic thickness values varying between 50 km and 300 km. Furthermore, only the central areas of the northern lowlands reach such high values whereas most areas in the vicinity of the dichotomy boundary exhibit very low elastic thickness values similar to those in the southern uplands. I attribute this observation at least partly to the multitapering because the distance from the southern uplands at which higher elastic thickness values occur increases with increasing spherical cap size θ_0 of the taper and the multitapering assumes an isotropic distribution in the window.

Nevertheless, one can clearly conclude that T_e is higher in the northern lowlands than in the southern uplands. The strong gravity signal and the smooth topography indicate buried loads below the surface. The fact that these subsurface loads are not represented in the surface topography suggests that the lithosphere must be quite rigid. A high elastic thickness would be expected even though the crust is thin. This also corresponds to the observation that the northern lowlands are a relatively young surface. At the time when the current surface formed and loading occurred, Mars had already had more time to cool down than when the southern uplands formed, which is why the lithosphere was less elastic at the time of loading.

The load ratio in the northern lowlands is at 0.7 to 0.9 very high. This means that the amplitude of the bottom load was much higher than the amplitude of the top load before flexure and is also what is observed today. Such a low amplitude topography can be caused by sedimentation and erosion processes which bury the original topography under a new layer and could for example have been caused by an ocean in the Northern Hemisphere at some point in the history of Mars (Di Achille and Hynek, 2010; Head et al., 1999). This hypothesis is contradicted by the load correlation, which is either strongly positive or strongly negative in the entire northern lowlands and in fact on most of the planet. Sedimentation and erosion are processes which only directly affect the surface and therefore decorrelate surface and subsurface topographies. A value around $r = 0$ would be expected. The actual value of $r = -0.8$ indicates a loading process which has affected both surface and subsurface. This contradiction can be explained when the sedimentation or erosion process which eradicated the surface topography is not the dominant loading process (Hoogenboom and Smrekar, 2006). The sedimentation or erosion process may have occurred at a much later point when the lithosphere was already much more rigid and a thin layer of sediments could not cause significant flexure any more. The original surface before sedimentation and erosion may have had more correlation with the subsurface. The high elastic thickness then reveals that the lithosphere has already been quite rigid when the buried original surface of the northern lowlands formed, although that may have been significantly earlier than when its current surface was generated.

Another way of explaining the high elastic thickness in the northern lowlands is by questioning the assumption on crustal density. This study has assumed a crustal density of $\rho_c = 2900\,\frac{\mathrm{kg}}{\mathrm{m}^3}$ globally for simplicity and to keep the number of estimated parameters small. Since the crusts of northern lowlands and southern uplands have different formation histories, different densities are not unlikely. A higher density in the northern low-

lands would require a lower elastic thickness which might be in between those of the southern highlands and the volcanic regions. This hypothesis would be more in line with a formation process which occurred before the creation of the large volcanoes (Zuber et al., 2000).
McGovern et al. (2002) found that there are no simple models which fit the data of the northern lowlands well in their conventional spectral modelling approach. Instead, they propose forward modelling as a more suitable technique. Using forward modelling, Zuber et al. (2000) found values of $T_e = 100$ km at the Utopia basin, which is also contained in the area investigated in this study (Section 4.6.8). Hoogenboom and Smrekar (2006) modelled the elastic thickness in the northern lowlands using four 2D Cartesian windows and obtained results between 10 and 25 km. By using Cartesian windows they ignored membrane stresses (Turcotte et al., 1981) and finite-amplitude effects Wieczorek and Phillips (1998), and induced projection errors. Their four windows were chosen because their topographic power was comparable to that in the southern uplands. This seems questionable as the low topographic power is a pervasive feature of the northern lowlands. Finally, Audet (2014) also modelled the northern lowlands in their global map. They found $T_e = 90$ km in most areas and load ratios around 0.7. These values correspond quite well with the values of this study and the spatial distribution is also very similar, with areas of lower elastic thickness north of Elysium Mons and Alba Patera.

5.3. THARSIS REGION

Applying small windows ($\theta_0 = 10°$) to the volcanoes Olympus Mons, Ascraeus Mons, Pavonis Mons and Arsia Mons reveals most likely elastic thickness values which lie between 30 and 60 km. These values indicate a moderately rigid lithosphere at the time of loading. Observing these values in the context of their spatial surroundings reveals that they are strictly confirmed by a global map of the elastic thickness obtained using the same tapering parameters (Figure 4.5). Notably, however, there are locations of very high T_e, reaching the highest sampled value of 300 km, in the vicinity of every one of the volcanoes: on the western flank of Olympus Mons, slightly north of Ascraeus Mons and Arsia Mons, and east of Pavonis Mons. Apart from these locations, the remaining area of the Tharsis province is best modelled by values between 10 and 60 km. This result from modelling with a very localized window of $\theta_0 = 10°$ stands in contrast to the results for $\theta_0 = 30°$. A large area centered around Olympus Mons and including the other Tharsis volcanoes has very high elastic thicknesses, but the parts of the Tharsis region which lie east and south of that are best modelled by $T_e = 10$ km. This contrast indicates a lack of homogeneity in the whole region which causes the results to depend strongly on the multitaper window size. The best conclusion that can be drawn from these very unconstrained results is that the elastic thickness of the shield of Tharsis has the same order of magnitude as the elastic thickness of the volcanoes, between 30 and 60 km. This allows the interpretation that the Tharsis province formed at a time when the crust was already cooled down more than during the formation of the southern uplands and Elysium Mons. Olympus Mons formed later than the Tharsis Montes.
The load ratio at the large volcanoes is small, whereas the other regions of Tharsis reach high values up to 0.9 (Figure 4.6). This can indicate a depleted mantle or dense intrusive materials in the crust. The local differences in the initial load ratio can then result from the different surface topographies, even if the subsurface topographies are similar in the whole Tharsis region.
McKenzie et al. (2002) used line of sight velocities from radio science tracking in a large window encompassing almost the entire Tharsis region to obtain one best fit value for the entire region and found the elastic thickness to be 70 km. This value is best compared with the results obtained in this study when using a window size of 30° (Figure 4.11) which also indicates higher, but very unconstrained values in the Tharsis region in general. Audet (2014) found $T_e = 150$ km in a large area centered around Olympus Mons and including the other Tharsis volcanoes which is also very similar to the area of high T_e values in that experiment. Correspondingly, they then found lower values in the southern and eastern part of Tharsis.
Other studies used localized windows to investigate the volcanoes in the Tharsis province. Zuber et al. (2000) used 2D multitaper coherence methods to find that the elastic thickness at Olympus Mons and the Tharsis Montes should be larger than 100 km. McGovern et al. (2002) and McGovern et al. (2004) computed the admittance from shape and finite amplitude corrected gravity to infer on the elastic thickness. In their geophysical model, the surface and subsurface loads are modelled individually and not as undulations on the respective interface, as is done in this study. They also possess densities which can be different from crustal and mantle densities. This makes their model more elaborate, but also more complicated than the model used in this study, and they leave additional parameters free. In a model without bottom loading, they constrained T_e to be larger than 70 km at Olympus Mons, between 2 and 80 km at Ascraeus Mons, smaller than 100 km at

Pavonis Mons, and larger than 20 km at Arsia Mons. These values agree with the results of this study within their respective uncertainties.
Belleguic et al. (2005) applied a model which is quite similar to the one used by McGovern et al. (2002), but they use a more rigorous method to calculate the gravity anomalies caused by the various interfaces and the loads resulting from them. In a model without subsurface loading, they found an elastic thickness of 93 ± 40 km for Olympus Mons, 105 ± 40 km for Ascraeus Mons, more than 50 km for Pavonis Mons, and less than 30 km for Arsia Mons. In a model which includes subsurface loading they found an elastic thickness of more than 70 km for Olympus Mons, more than 50 km for Ascraeus and Pavonis Montes, and less than 35 km for Arsia Mons. The inclusion of subsurface loads significantly improves their model, especially at Arsia Mons, but also at Olympus Mons, indicating the importance of subsurface loading. The values of Belleguic et al. (2005) are somewhat higher than the most likely solutions obtained in this study which emphasizes the importance of correctly modelling the gravity signal.
Beuthe et al. (2012) applied two models to retrieve the elastic thickness from admittance comparisons. Using models including top and bottom loads, similar to the one used by McGovern et al. (2002), they found an elastic thickness of more than 110 km for Olympus Mons, between 20 and 60 km for Ascraeus Mons, and less than 10 km for Arsia Mons. No model could be fit to the observed admittance signature of Pavonis Mons. Another model assumes two loading processes at different points in time. First, the Tharsis rise developed, at a time of lower elastic thickness. Then, the large volcanic shields developed on top of the Tharsis basement at a later time, when the elastic thickness was already higher. The results of these loading history models generally agree with the conventional model including surface and subsurface loads.
In conclusion, the elastic thicknesses resulting from localized admittance studies for Olympus Mons and the Tharsis Montes as presented by McGovern et al. (2002), Belleguic et al. (2005), and Beuthe et al. (2012) tend to be slightly higher than the results of this study. An interesting difference is the low elastic thickness which all of these studies obtain for Arsia Mons whereas this study finds the highest elastic thickness values out of all Tharsis Montes there.

5.4. ELYSIUM MONS

The most likely elastic thickness for Elysium Mons is 20 km. This means that there must have been a high heat flow at the time of loading, although not as high as for the southern uplands. There is, however, an area on the western flank, where the most likely value is 300 km which indicates some lack of constraint which is not visible in the contours of log-likelihood for Elysium Mons (Figure 4.25). The load ratio at Elysium Mons is at 0.3 relatively small, but significantly different from zero. This indicates a lower density in the upper mantle which could be caused by either a mantle plume or a depleted mantle composition (Belleguic et al., 2005).
McGovern et al. (2004) found a value of 15 to 45 km, but they also solve for a load density, for which they obtain a best fit value of $3250 \frac{\text{kg}}{\text{m}^3}$. By solving for the load density, they consider that the crustal material close to volcanoes may have a different density than that found in other parts of the crust. This higher load density leads to larger elastic thickness estimates which would explain why McGovern et al. (2004) found a slightly higher value than this study with a relatively similar geophysical model. In their conventional model using top and bottom loads, Beuthe et al. (2012) found an elastic thickness of less than 30 km at Elysium Mons. Their new model which considers the loading history revealed that the volcanic basement of the Elysium rise essentially reached isostatic equilibrium. Then, the volcanic shield of Elysium Mons developed at a later time, and they found the elastic thickness for this second step to be 20 km, thereby well agreeing in both models with this study. McKenzie et al. (2002) found a value of 29 km using line of sight velocities which is also comparable to the result of this study. Belleguic et al. (2005) found a significantly higher value of 56 ± 20 km with a similar, but more refined model and similar load density as McGovern et al. (2004). Both studies found that bottom loads are not necessary, but can improve the fit. Audet (2014) found even higher elastic thickness values of around 90 km with his wavelet method, but agreed on the low load ratio.

5.5. VALLES MARINERIS

This study finds as the most likely elastic thickness for Valles Marineris 20 km, a value which is quite constrained and associated with a load ratio of 0.2. This solution indicates a formation when the lithosphere was quite hot, significantly earlier than when the Tharsis region formed.
McKenzie et al. (2002) used admittances from line of sight velocity measurements in a rectangular window around Valles Marineris to find a best fit solution of $T_e = 53$ km. Audet (2014) received values of 80 km and higher in the area around Valles Marineris from his wavelet transform of free-air and Bouguer coherence and

admittance. McGovern et al. (2004) applied several small windows to some of the major chasmata and analyzed the admittance signatures with top and bottom loading models. They found elastic thicknesses greater than 60 km in all windows when using a load density of 2900 $\frac{\mathrm{kg}}{\mathrm{m}^3}$ and bottom loading, and slightly lower values for models without bottom loading which include the load density as a free parameter. In the latter case, they found significantly lower load densities, but McGovern et al. (2002) state that these are unlikely, and the scenario including bottom loads, which could be caused by crustal thinning, seems more likely. Beuthe et al. (2012) also applied small windows to several regions of Valles Marineris, but also used a large window including the entire system. They received values larger than 70 km in all cases, and significant load ratios when they modelled bottom loads.

In conclusion, all previous studies found much higher elastic thickness values than this study. These indicate a formation of Valles Marineris after the Tharsis region. The large discrepancy may be due to the lack of flexibility with regard to density variations in this study, or due to problems with the inhomogeneous terrain in the large window which was used.

5.6. IMPLICATIONS FOR THE METHODOLOGY

In this study, the maximum likelihood estimation framework for the determination of the effective elastic thickness of the lithosphere, first proposed by Simons and Olhede (2013), has for the first time been applied to real data. Most previous studies had used spectral ratios to estimate the elastic thickness. The admittance and coherence are derived quantities from the observed global fields of gravity and topography. Even if the observed data possess a Gaussian distribution, functions of these data do not generally do so. This makes it impossible to assess if the currently widely used least squares curve fitting of admittance and coherence is even statistically significant (Simons and Olhede, 2013).

Furthermore, the inversion problem is losing degrees of freedom when the two-dimensional data are reduced to spectral ratios which only depend on the wavelength or spherical harmonic degree. Maximum likelihood estimation is avoiding these two problems by estimating the most likely solution directly from the observations.

The main components of the estimation framework are the input data, the flexural model (Equation 3.42), the concepts of proportionality and correlation of the initial loads (Equation 3.53), and the isotropic covariance function of the Matérn type. Several assumptions had to be made to combine these components into a tractable form for maximum likelihood estimation.

First, the log-likelihood Equation 3.72 uses the surface and subsurface topography as inputs, even though the actual observations are the surface topography and the gravity. The derivation of the subsurface topography from the gravity is only possible under several simplifying assumptions. There are only two interfaces, the crust-mantle boundary and the surface, and crust and mantle densities are assumed to be globally homogeneous and known. There is, however, general agreement that the densities are different both on the largest scale, which is the Martian dichotomy, and on small scales. It is therefore important to regard the subsurface topography rather as a translation of the observed gravity signal into a topography which is given in units of height. During this conversion, all processes which cause density differences, such as intrusions and mantle depletion, are combined into one global topography field. As Belleguic et al. (2005) found, the crustal thickness is not a parameter which has a very strong impact on elastic thickness estimation. In this study, the crustal thickness estimation is completely separated from the elastic thickness estimation, but an inclusion of the gravity field into the maximum likelihood estimation framework does not seem feasible at this point.

Second, the actual flexural model also uses only two interfaces, and both loading and compensation occur only at those interfaces. This is a simplification which several previous studies have overcome (e.g. Belleguic et al., 2005; McKenzie, 2003). The goal of this study has been to keep the model as simple as possible which also helps to apply it globally without having to readjust the model for different locations. For certain features, for example volcanoes, it is very reasonable to assume more complex models because justifications for such models from different sources exist. For example, the inclusion of a load density is useful because the volcanic shield consists of different materials than the crust, based on their formation history. The results of this study are not constrained very well for many volcanoes, indicating that another more sophisticated model might be needed. This includes modelling topographies as individual layers rather than as small perturbations on the interfaces. Belleguic et al. (2005) showed also here that a significant difference exists between those two methods. The model should however not contain too many degrees of freedom.

Third, the flexural model used in this study is based on the concept of the effective elastic thickness. The lithosphere is assumed to be perfectly elastic, integrating ductile and brittle strength. This is an assumption that neglects tectonic and viscoelastic effects. While a change of the model to incorporate such effects would without doubt be interesting, these assumptions are quite reasonable.

Fourth, the model used in this study also neglects elastic anisotropy by treating the entire flexural process isotropically. It has been shown that anisotropy is very relevant on Mars (Audet, 2011; Beuthe et al., 2012). Flexure models which account for anisotropy exist (Kirby and Swain, 2009; Simons et al., 2000), but only in the 2D case. When investigating Mars, the anisotropic flexure of a thin elastic shell would have to be modelled, which is significantly more complex than that of a thin elastic shell (Wieczorek, 2007) and has not been attempted yet to my knowledge.

Fifth, this model treats the initial load correlation r and the initial load ratio F as being independent of the spherical harmonic degree l which is of course in practice not the case. Any set of surface and subsurface topographies will have different amplitudes at different spherical harmonic degrees which generally do not coincide. While keeping F and r constant for all spherical harmonic degrees is a rather unrealistic assumption, estimating a separate parameter for each l would leave too many degrees of freedom in the model. Forsyth (1985) estimated F as a function of wavelength, but this greatly increased the number of estimated parameters and therefore led to the data always being close to perfectly fit.

Finally, two of the largest assumptions in the modelling in this study are related to the multitapering.

Firstly, all parameters are assumed to be homogeneous within the window, including the six estimated parameters, but also the densities and other lithospheric parameters which are assumed constant globally in this study. Considering that the typical window sizes used in this study, ranging from diameters of 20° to 60°, usually include several geologic provinces, this assumption is quite limiting, which is also why windows have been kept as small as possible.

Secondly, the windowing introduces correlations between the spherical harmonic degrees of the input fields, so that the observations do not follow a Gaussian distribution any longer. The coefficients of each spherical harmonic degree and order of gravity and topography are distributed as independent, Gaussian random variables. This would be important for an analytical calculation of the confidence intervals of the estimated parameters (Simons and Olhede, 2013) which has not been attempted in this study for this reason. By correlations between the spherical harmonic degrees, the coefficients develop mutual dependencies. Therefore, only a Monte Carlo approach could be applied to retrieve estimates of the model accuracy.

The Monte Carlo simulations which have been performed for nine localized windows on Mars (Section 4.6) have given some insight into the behavior of the model. The retrieval of the principal parameter of interest, the elastic thickness, is sometimes difficult. When synthetic topographies are generated using low $T_e < 30$ km, the input value could be reproduced quite well. For higher values of T_e, the most likely solutions are either low or at the maximum of allowed values, $T_e = 300$ km. The actual input value is rarely reproduced for $T_e > 30$ km. This is a major problem because it does not allow to make any meaningful constraints for locations where the elastic thickness is high.

The load ratio, on the contrary, can always be resolved very well. In the case of the load correlation, the model fails to distinguish between positive and negative correlation. When a strong positive load correlation is used as an input parameter for the Monte Carlo simulation, both strong positive and strong negative correlations are about equally likely to result from it, and vice versa. These difficulties in the retrieval of model parameters stand in contrast to the very encouraging results of Simons and Olhede (2013) and are insofar unexpected. I identify the grid spacing and the multitapering as possible reasons for the model failure for high T_e and r. Because of computational limitations, the most likely parameter set is chosen from a range of possible sets which are sampled on a rather coarse grid (see Table 4.1). A sampling interval of 10 km is potentially too large to find the maximum likelihood T_e values in a six dimensional parameter space. The same holds for r which is sampled in intervals of 0.2. Simons and Olhede (2013) applies some unspecified kind of tapering, or blurring, to the data in his simulations, but the multitaper localization on the sphere may have significantly worse properties, which are a result of the spherical nature of the problem and of the low resolution of the observed data fields. The multitapering may therefore blur the simulated data to an extent that they are no longer reproducable.

The maximum likelihood framework for the estimation of the elastic thickness estimates the load correlation r as a free parameter which has not been accomplished by other studies. However, it has been revealed that a very strong correlation is the most likely solution in almost all cases. This corresponds to the assumption of $r = 1$ which is common in planetary science (Belleguic et al., 2005; Beuthe et al., 2012; McGovern et al., 2002). It remains to be assessed how much advantage an estimation of r as a free parameter gives over this assumption, especially in the context of how unconstrained the model is when it comes to determining r.

6

Conclusion

6.1. Summary

In this study, maximum likelihood estimation has been applied to constrain the effective elastic thickness of the Martian lithosphere both globally and locally. Because of the large amplitudes of the Martian shape and gravity fields and its comparably small radius, the estimation framework of Simons and Olhede (2013) had to be redeveloped for the spherical case, resulting in a flexure model very similar to those used by McGovern et al. (2002) and Audet (2014). For the localization of the global shape and gravity fields, spherical multitaper analysis was used, which is optimally concentrated (Wieczorek and Simons, 2005).

The input observables to the geophysical model are surface and subsurface topography, or the distance of surface and crust-mantle boundary from the center of mass of Mars. In a pre-processing step, the subsurface topography has been obtained from the free-air gravity using the method of Wieczorek and Phillips (1998) which determines the subsurface topography that could have caused the observed gravity while respecting large amplitudes of the Martian gravity field. The resulting global map of the crustal thickness exhibits values ranging from 3 to ~ 100 km.

Using a two-layer flexure model where loading and compensation occur as perturbations on the two interfaces, the modelled covariance spectrum of surface and subsurface topography has been determined. This covariance spectrum depends on a set of six free parameters, including the elastic thickness T_e, the initial load ratio F, the initial load correlation r, and three parameters of the Matérn covariance function, namely the smoothness ν, the decorrelation distance ρ, and the variance σ^2. These are sampled in the six dimensional parameter space and the covariance spectrum is computed for each combination of parameters.

For each parameter set, the log-likelihood Equation 3.72 is evaluated. The inputs for this equation are the observed or derived surface and subsurface topography and their modelled covariance spectra. All of these quantities have to be localized with suitable windowing functions to receive local estimates.

On a grid of 4°, localization windows have been applied to the whole globe, and for each of the points, a most likely solution of six estimated parameters has been determined. The maps which have been created in this way reveal the global distribution of the elastic thickness and the other parameters on Mars. The results are given for several tapering parameters. When using only one taper, the window size can be decreased to $\theta_0 = 10°$ while still retaining sufficient bandwidth for the analysis. Maps using such a small window size are best to characterize small features in inhomogeneous terrain. For global studies, larger windows are useful, because more tapers can be used to improve the statistical significance. A map using windows with $\theta_0 = 30°$ was presented to reveal low elastic thickness values in the southern uplands of Mars, and higher values in the northern lowlands and the volcanic provinces. Transitional areas such as the hemispheric dichotomy boundary are difficult to analyze because the parameters change within the size of the window, which is not reflected in the model.

For nine specific locations on Mars the contours of the log-likelihood were presented to investigate the constraint of the model parameters. The elastic thickness is most likely to be 10 km in the southern uplands, 20 km at Elysium Mons, 30 to 40 km at the Tharsis Montes, and 60 km at Olympus Mons. The elastic thickness decreases with the age of the features which can be explained by a lithosphere which has cooled down over time. The northern lowlands received a most likely estimate of 210 km which is very large and does not correspond to this interpretation. All locations at which the elastic thickness was larger than 30 km had very

unconstrained solutions.
This impression was confirmed by a Monte Carlo simulation. Synthetically generated planetary topographies have been used to investigate the reliability of the model. On the basis of the most likely parameter set for each location, synthetic topographies were generated, which were then treated as input data to a new estimation. The most likely parameter sets from this new estimation revealed that the elastic thickness can be reproduced very well when it is small, but the reproduction fails when T_e is large. A lack of constraint and confidence on the solution in previous studies has been one of the reasons why this study did not use the more conventional admittance and coherence methods and instead the maximum likelihood framework was implemented for the first time. In its current state, however, maximum likelihood estimation can not yet reach the quality of elastic thickness modelling which is currently the standard in literature.

6.2. OUTLOOK

More research is needed to determine if maximum likelihood estimation can be a viable alternative to admittance and coherence methods for elastic thickness modelling. I identify several features which are likely to improve the processing used in this study meaningfully, but were out of its scope.
For all experiments in this study, the six dimensional parameter space has been sampled at certain grid points where the log-likelihood was determined. The spacing of this sampling is limited by the computational effort it creates and the flexural model had to be computed and multitapered for 412500 possible combinations of parameters. Still, the resolution is not sufficient. For example, the elastic thickness is sampled in intervals of 10 km. While a geological interpretation is possible with this resolution (Beuthe et al., 2012), it might be problematic for finding the most likely value. This is even more of a problem for the other parameters, which are sampled at larger intervals.
I therefore recommend the implementation of an iterative algorithm which does not need to evaluate the log-likelihood at all grid points, but rather progressively searches for the most likely solution. This promises a higher resolution of the solution after far less than 412500 iterations and, equivalently, model evaluations. The original reason not to implement was the goal of creating a global map. When the most likely parameter set has to be determined, the model evaluations only have to be carried out once and can be reused at every map grid point. If future studies focus on single locations or on the methodology itself, this will not be a problem. Iterative algorithms for finding maxima in six dimensional parameter spaces are readily available when lower and upper bounds are known for all parameters.
For nine parameter sets, which are the most likely parameter sets of the localization windows investigated in Section 4.6, synthetic topographies were created. 100 of those simulations were used again as inputs for the same model to test the capacity of the model to reproduce its input values. This has already led to the conclusion that low elastic thickness values can be reproduced better than high ones. It would be helpful to assess this model behavior more systematically, and not just on the basis of nine parameter sets. This would give insights into when exactly it is difficult to retrieve T_e and the other parameters. Such a procedure would also be of special importance for the estimation of r. Most likely values for r tend strongly towards strong positive or negative correlation. A systematic analysis could reveal if this is a modelling bias because the parameter cannot be retrieved properly, or if the initial load correlation is indeed almost always strong on Mars.
Finally, when this research has been carried out and the estimation procedure has been understood more thoroughly, different physical models could be implemented. The flexural model used in this study is as simple as possible while keeping it realistic. Simplicity is beneficial for the understanding of a model and to keep the number of parameters small, and thereby the estimation process tractable. When the model is well understood, more features can be added to it to make it more realistic.
Most importantly, the currently used model does not account for density differences apart from crust and mantle densities. There is geological evidence for example for higher density surface loads in volcanic regions, a hemispheric difference in crustal thickness, and subsurface loads of other density (Belleguic et al., 2005). There are several studies which include such slightly more sophisticated assumptions into their model to receive good results for Mars (Belleguic et al., 2005; Beuthe et al., 2012; McGovern et al., 2002). The density can also be included as a free parameter into the model which would increase the number of parameters to seven.
Another interesting problem in elastic thickness estimation is anisotropy. The model used in this study treats the lithosphere completely isotropically, which is manifested in many parts of it, such as the flexural model, the spectral Matérn covariance function, and the multitapering. However, there is strong evidence from radio science tracking analyses that the elastic thickness on Mars behaves anisotropically (Beuthe et al., 2012).

Unfortunately, to date no flexural model for a thin elastic shell which does not assume isotropy exists to my knowledge, so that considerable theoretical work would be needed to investigate the anisotropy of Mars's lithosphere using spectral methods.

A

SPHERICAL HARMONICS

This appendix gives a short overview over the spherical harmonics representation used in this study. Similar introductions can be found e.g. in Hofmann-Wellenhof and Moritz (2006) or Wieczorek (2007).
A generic function on the sphere $f(\Omega)$ can be represented as a linear combination of spherical harmonics as

$$f(\Omega) = \sum_{l=0}^{\infty} \sum_{m=-l}^{l} f_{lm} Y_{lm}(\Omega) \tag{A.1}$$

where Y_{lm} are the spherical harmonics of degree l and order m, f_{lm} are the spherical harmonics coefficients, and $\Omega = (\theta, \lambda)$ is the position on the sphere, with θ being the colatitude and λ the longitude. The equivalent Cartesian wavelength to spherical harmonic degree l is (Wieczorek, 2008)

$$\lambda_l \approx \frac{2\pi \bar{R}^t}{\sqrt{l(l+1)}} \tag{A.2}$$

The spherical harmonics are defined as

$$Y_{lm} = \bar{P}_{l|m|}(\cos\theta) \begin{cases} \cos(m\lambda) & \text{for} \quad m \geq 0 \\ \sin(|m|\lambda) & \text{for} \quad m < 0 \end{cases} \tag{A.3}$$

where $\bar{P}_{lm}(x)$ are the normalized associated Legendre functions given by

$$\bar{P}_{lm}(x) = \sqrt{(2-\delta_{0m})(2l+1)\frac{(l-m)!}{(l+m)!}} P_{lm}(x)\,, \tag{A.4}$$

with δ_{ij} the Kronecker delta. The unnormalized associated Legendre functions $P_{lm}(x)$ are related to the Legendre polynomials $P_l(x)$ by

$$P_{lm}(x) = (1-x^2)^{\frac{m}{2}} \frac{\mathrm{d}^m}{\mathrm{d}x^m} P_l(x) \tag{A.5}$$

and the Legendre polynomials are given by

$$P_l(x) = \frac{1}{2^l l!} \frac{\mathrm{d}^l}{\mathrm{d}x^l} (x^2-1)^l\,. \tag{A.6}$$

The spherical harmonics are then orthogonal with a 4π-normalization which is commonly used in geodesy:

$$\iint_{\Omega} Y_{lm}(\Omega) Y_{l'm'}(\Omega) \mathrm{d}\Omega = 4\pi \delta_{ll'} \delta_{mm'}\,. \tag{A.7}$$

Parsival's theorem on the sphere relates the power in the spatial and spectral domains:

$$\frac{1}{4\pi} \int_0^{2\pi} \int_0^{\pi} f^2(\Omega) \sin\theta \mathrm{d}\theta \mathrm{d}\lambda = \sum_{l=0}^{\infty} \sum_{m=-l}^{l} f_{lm}^2\,. \tag{A.8}$$

B

DIFFERENTIAL OPERATORS

The gradient of a scalar $a(\theta,\lambda)$ on the surface of a sphere $\mathcal{S}^2$ is

$$\nabla a = \begin{pmatrix} \frac{\partial}{\partial\theta} \\ \csc\theta\frac{\partial}{\partial\lambda} \end{pmatrix} a = \begin{pmatrix} \frac{\partial a}{\partial\theta} \\ \csc\theta\frac{\partial a}{\partial\lambda} \end{pmatrix}. \tag{B.1}$$

The surface divergence of a vector $\boldsymbol{b} = [b_\theta, b_\lambda]^\top$ is given by

$$\nabla\cdot\boldsymbol{b} = \csc\theta\left(\frac{\partial(\sin\theta\, b_\theta)}{\partial\theta} + \frac{\partial b_\lambda}{\partial\lambda}\right). \tag{B.2}$$

The surface Laplacian operator is the surface divergence of the surface gradient of a scalar $a(\theta,\lambda)$ and given by

$$\nabla^2 a = \nabla\cdot\nabla a = \frac{\partial^2 a}{\partial\theta^2} + \cot\theta\frac{\partial a}{\partial\theta} + \csc^2\theta\frac{\partial^2 a}{\partial\lambda^2}. \tag{B.3}$$

Besides, we write (Beuthe, 2008)

$$\left(\nabla^2\right)' = \nabla^2 + 2. \tag{B.4}$$

In spherical harmonic space, the surface Laplacian operator of a function $Y_{lm}(\Omega)$ can be simply written as (Audet, 2014)

$$\nabla^2 Y_{lm}(\Omega) = -l(l+1)\,Y_{lm}(\Omega). \tag{B.5}$$

C

Overview of symbols

Table C.1: Overview of symbols used in this study, including their descriptions, units, and the equations in which they are defined or first mentioned.

Symbol	Unit	Description	Eq.
f	-	Generic function	
x	-	Generic function argument	
$\boldsymbol{r}$	m	Position vector	2.1
$\boldsymbol{d}$	m	Distance vector between two arbitrary points	3.56
r	m	Distance of a point from the center of mass	2.1
Ω	-	Surface location vector	A.1
θ	rad	Colatitude	A.1
λ	rad	Longitude	A.1
ψ	rad	Great circle distance	3.62
l	-	Spherical harmonic degree	A.1
m	-	Spherical harmonic order	A.1
L	-	Maximum degree of spherical harmonic expansion	
λ_l	-	Equivalent Cartesian wavelength	A.2
Y_{lm}	-	Spherical harmonics	A.3
$\bar{P}_{lm}$	-	Normalized associated Legendre functions	A.4
P_{lm}	-	Unnormalized associated Legendre functions	A.5
P_l	-	Legendre polynomials	A.6
G	$m^3kg^{-1}s^{-2}$	Universal gravitational constant	2.1
M	kg	Mass of a planet	2.1
R_g	m	Reference radius of the gravity field	2.1
$\bar{R}^t$	m	Mean planetary radius	2.9
$\bar{R}^b$	m	Mean radius of the subsurface interface	3.31
U	m^2s^{-2}	Gravitational potential	2.1
V	m^2s^{-2}	Potential of reference body	2.6
T	m^2s^{-2}	Disturbing potential	2.6
σ_l	-	Spherical harmonic degree variance	2.2
σ	-	Root of the potential power per coefficient	2.3
g	ms^{-2}	Gravitational attraction	3.18
Δg	ms^{-2}	Gravity anomaly	2.4
Δg_B	ms^{-2}	Bouguer correction	2.8
g_B	ms^{-2}	Bouguer anomaly	2.7
C_{lm}	-	Stokes coefficients	2.1
C_{lm}^{BC}	-	Stokes coefficients of the Bouguer correction	2.9

Symbol	Unit	Description	Eq.
C_{lm}^{BA}	-	Stokes coefficients of the Bouguer anomaly	2.10
χ_l	-	Downward continuation filter	3.30
λ	-	Lagrange multiplier	3.30
D	Nm	Flexural rigidity of the lithosphere	1.1
T_e	m	Elastic thickness of the lithosphere	1.1
T_c	m	Crustal thickness	4.1
E	ms^{-2}	Young's modulus	1.1
ν	-	Poisson's ratio	1.1
ρ_c	kgm^{-3}	Crustal density	2.8
ρ_m	kgm^{-3}	Mantle density	
$\Delta\rho$	kgm^{-3}	Density difference between crust and mantle	3.17
u	m	Deflection of a shell	3.11
q	Nm^{-2}	Loading pressure on a shell	3.11
ξ	Nm^{-3}	Flexural parameter	3.13
τ	Nm^{-3}	Flexural parameter	3.13
f_1	-	Parameter dependent on the spherical harmonic degree	3.14
f_2	-	Parameter dependent on the spherical harmonic degree	3.14
f_3	-	Parameter dependent on the spherical harmonic degree	3.14
L^t	Nm^{-2}	Loading pressure onto the surface interface	3.50
L^b	Nm^{-2}	Loading pressure onto the subsurface interface	3.50
h	m	Final (measurable) surface topography (shape) after flexure	3.33
w	m	Final (measurable) subsurface topography (shape) after flexure	3.29
h^t	m	Equilibrium surface topography caused by top loading	3.17
w^t	m	Equilibrium subsurface topography caused by top loading	3.17
h^b	m	Equilibrium surface topography caused by bottom loading	3.24
w^b	m	Equilibrium subsurface topography caused by bottom loading	3.24
h^i	m	Initial surface topography before flexure	3.35
w^i	m	Initial subsurface topography before flexure	3.36
α^t	-	Flexural filter of top loading	3.21
α^b	-	Flexural filter of bottom loading	3.27
$\boldsymbol{h}$	m	Vector of final surface and subsurface topography	3.42
$\boldsymbol{h}^i$	m	Vector of initial surface and subsurface topography	3.42
$\boldsymbol{M}_{T_e}$	-	Geophysical model matrix	3.42
$\bar{\boldsymbol{h}}$	m	Multitapered vector of final surface and subsurface topography	3.72
q	s^{-2}	Isostatic response function	1.2
$\bar{q}$	s^{-2}	Fourier transform of isostatic response function, admittance	1.3
γ^2	-	Coherence	1.4
$\bar{g}$	ms^{-2}	Fourier transform of gravity	1.3
$\bar{h}$	m	Fourier transform of topography	1.3
F	-	Load ratio	1.5
f^2	-	Loading fraction	1.6
r	-	Load correlation coefficient	3.48
S_{hh}	m^2	Spectral auto-covariance of final surface topography	3.44
$\boldsymbol{S}_{\boldsymbol{hh}}$	m^2	Spectral cross-covariance matrix of final topographies	3.44
$S_{h^i h^i}$	m^2	Spectral auto-covariance of initial surface topography	3.45
$\boldsymbol{S}_{\boldsymbol{h}^i \boldsymbol{h}^i}$	m^2	Spectral cross-covariance matrix of initial topographies	3.45
$\bar{\boldsymbol{S}}_{\boldsymbol{hh}}$	m^2	Multitapered spectral covariance matrix of final topographies	3.72
c	-	Spatial concentration quality	3.1
H	-	Bandlimited taper function	3.1
$\boldsymbol{H}$	-	Vector of taper coefficients	3.7

Symbol	Unit	Description	Eq.
$D_{ll'}$	-	Coefficient of matrix $\boldsymbol{D}$	3.6
$\boldsymbol{D}$	-	Matrix of Legendre functions	3.7
L_b	-	Bandwidth	3.3
N_0	-	Space-bandwidth product	3.10
θ_0	rad	Size of spherical cap window	3.10
K	-	Number of near-perfectly concentrated tapers	
M	-	Matérn covariance	3.56
σ^2	m^2	Variance of the Matérn covariance	3.56
ν	-	Smoothness parameter	3.56
α	-	Scale parameter	3.56
ρ	-	Range parameter, decorrelation distance	3.61
$\Gamma(x)$	-	Gamma function	3.56
$\mathscr{K}_\nu(x)$	-	Modified Bessel function of the second kind	3.57
$\mathscr{I}_\nu(x)$	-	Modified Bessel function of the first kind	3.58
d	-	Dissimilarity	4.3
$X_{lm}, X^1_{lm}, X^2_{lm}$	-	Sequences of independent, real-valued, standard normally distributed random variables	3.76
$\mathscr{P}$	-	Probability function	3.70
$\mathscr{L}$	-	Likelihood function	3.72
$\boldsymbol{y}$	-	Set of parameters to be estimated in the maximum likelihood estimation	3.71
y_i	-	A generic parameter	4.2
n_{y_i}	-	Number of values at which a generic parameter is sampled	4.2
n_{tot}	-	Number of parameter sets for which the likelihood is calculated	4.2

Bibliography

Abramowitz, M. and Stegun, I. A. (1964). *Handbook of mathematical functions: with formulas, graphs, and mathematical tables*. 55. Courier Corporation.

Audet, P. (2011). Directional wavelet analysis on the sphere: Application to gravity and topography of the terrestrial planets. *Journal of Geophysical Research: Planets (1991–2012)*, 116(E1).

Audet, P. (2014). Toward mapping the effective elastic thickness of planetary lithospheres from a spherical wavelet analysis of gravity and topography. *Physics of the Earth and Planetary Interiors*, 226:48–82.

Audet, P. and Bürgmann, R. (2011). Dominant role of tectonic inheritance in supercontinent cycles. *Nature Geoscience*, 4(3):184–187.

Audet, P. and Mareschal, J.-C. (2007). Wavelet analysis of the coherence between Bouguer gravity and topography: application to the elastic thickness anisotropy in the Canadian Shield. *Geophysical Journal International*, 168(1):287–298.

Banerdt, W. (1986). Support of long-wavelength loads on Venus and implications for internal structure. *Journal of Geophysical Research: Solid Earth (1978–2012)*, 91(B1):403–419.

Baran, Á. and Terdik, G. (2015). Power spectrum estimation of spherical random fields based on covariances. In *Annales Mathematicae et Informaticae*, volume 44, pages 15–22.

Belleguic, V., Lognonné, P., and Wieczorek, M. (2005). Constraints on the Martian lithosphere from gravity and topography data. *Journal of Geophysical Research: Planets (1991–2012)*, 110(E11).

Beuthe, M. (2008). Thin elastic shells with variable thickness for lithospheric flexure of one-plate planets. *Geophysical Journal International*, 172(2):817–841.

Beuthe, M., Le Maistre, S., Rosenblatt, P., Pätzold, M., and Dehant, V. (2012). Density and lithospheric thickness of the Tharsis Province from MEX MaRS and MRO gravity data. *Journal of Geophysical Research: Planets (1991–2012)*, 117(E4).

Blakely, R. J. (1996). *Potential theory in gravity and magnetic applications*. Cambridge University Press.

Burov, E. and Watts, A. (2006). The long-term strength of continental lithosphere: "jelly sandwich" or "crème brûlée"? *GSA today*, 16(1):4–10.

Burov, E. B. and Diament, M. (1995). The effective elastic thickness (T_e) of continental lithosphere: What does it really mean? *Journal of Geophysical Research: Solid Earth (1978–2012)*, 100(B3):3905–3927.

Carr, M. H. and Head, J. W. (2010). Geologic history of Mars. *Earth and Planetary Science Letters*, 294(3):185–203.

Daly, E., Brown, C., Stark, C., and Ebinger, C. (2004). Wavelet and multitaper coherence methods for assessing the elastic thickness of the Irish Atlantic margin. *Geophysical Journal International*, 159(2):445–459.

Di Achille, G. and Hynek, B. M. (2010). Ancient ocean on Mars supported by global distribution of deltas and valleys. *Nature Geoscience*, 3(7):459–463.

Djomani, Y. H. P., Fairhead, J. D., and Griffin, W. L. (1999). The flexural rigidity of Fennoscandia: reflection of the tectonothermal age of the lithospheric mantle. *Earth and Planetary Science Letters*, 174(1):139–154.

Dorman, L. M. and Lewis, B. T. (1970). Experimental isostasy: 1. Theory of the determination of the Earth's isostatic response to a concentrated load. *Journal of Geophysical Research*, 75(17):3357–3365.

Driscoll, J. R. and Healy, D. M. (1994). Computing Fourier transforms and convolutions on the 2-sphere. *Advances in applied mathematics*, 15(2):202–250.

Forsyth, D. W. (1985). Subsurface loading and estimates of the flexural rigidity of continental lithosphere. *Journal of Geophysical Research: Solid Earth (1978–2012)*, 90(B14):12623–12632.

Gneiting, T. et al. (2013). Strictly and non-strictly positive definite functions on spheres. *Bernoulli*, 19(4):1327–1349.

Grott, M. and Breuer, D. (2008). The evolution of the martian elastic lithosphere and implications for crustal and mantle rheology. *Icarus*, 193(2):503–515.

Grott, M. and Breuer, D. (2010). On the spatial variability of the Martian elastic lithosphere thickness: Evidence for mantle plumes? *Journal of Geophysical Research: Planets (1991–2012)*, 115(E3).

Guinness, J. and Fuentes, M. (2016). Isotropic covariance functions on spheres: Some properties and modeling considerations. *Journal of Multivariate Analysis*, 143:143–152.

Guttorp, P. and Gneiting, T. (2006). Studies in the history of probability and statistics XLIX: On the Matern correlation family. *Biometrika*, 93(4):989–995.

Hahn, B., McLennan, S., and Klein, E. (2011). Martian surface heat production and crustal heat flow from Mars Odyssey Gamma-Ray spectrometry. *Geophysical Research Letters*, 38(14).

Handcock, M. S. and Stein, M. L. (1993). A Bayesian analysis of kriging. *Technometrics*, 35(4):403–410.

Hanssen, A. (1997). Multidimensional multitaper spectral estimation. *Signal processing*, 58(3):327–332.

Head, J. W., Hiesinger, H., Ivanov, M. A., Kreslavsky, M. A., Pratt, S., and Thomson, B. J. (1999). Possible ancient oceans on Mars: evidence from Mars Orbiter Laser Altimeter data. *Science*, 286(5447):2134–2137.

Hofmann-Wellenhof, B. and Moritz, H. (2006). *Physical geodesy*. Springer Science & Business Media.

Hoogenboom, T. and Smrekar, S. E. (2006). Elastic thickness estimates for the northern lowlands of Mars. *Earth and Planetary Science Letters*, 248(3):830–839.

Jeong, J. and Jun, M. (2015). A class of Matérn-like covariance functions for smooth processes on a sphere. *Spatial Statistics*, 11:1–18.

Kirby, J. and Swain, C. (2009). A reassessment of spectral T_e estimation in continental interiors: the case of North America. *Journal of Geophysical Research: Solid Earth (1978–2012)*, 114(B8).

Kirby, J. F. (2014). Estimation of the effective elastic thickness of the lithosphere using inverse spectral methods: the state of the art. *Tectonophysics*, 631:87–116.

Konopliv, A. S., Asmar, S. W., Folkner, W. M., Karatekin, Ö., Nunes, D. C., Smrekar, S. E., Yoder, C. F., and Zuber, M. T. (2011). Mars high resolution gravity fields from MRO, Mars seasonal gravity, and other dynamical parameters. *Icarus*, 211(1):401–428.

Konopliv, A. S., Yoder, C. F., Standish, E. M., Yuan, D.-N., and Sjogren, W. L. (2006). A global solution for the Mars static and seasonal gravity, Mars orientation, Phobos and Deimos masses, and Mars ephemeris. *Icarus*, 182(1):23–50.

Lang, A. and Schwab, C. (2015). Isotropic Gaussian random fields on the sphere: Regularity, fast simulation and stochastic partial differential equations. *The Annals of Applied Probability*, 25(6):3047–3094.

Lemoine, F. G., Smith, D. E., Rowlands, D. D., Zuber, M., Neumann, G., Chinn, D., and Pavlis, D. (2001). An improved solution of the gravity field of Mars (GMM-2B) from Mars Global Surveyor. *Journal of Geophysical Research: Planets (1991–2012)*, 106(E10):23359–23376.

Lowry, A. R. and Smith, R. B. (1994). Flexural rigidity of the Basin and Range-Colorado Plateau-Rocky Mountain transition from coherence analysis of gravity and topography. *Journal of Geophysical Research*, 99:20–123.

Lowry, A. R. and Zhong, S. (2003). Surface versus internal loading of the Tharsis rise, Mars. *Journal of Geophysical Research: Planets (1991–2012)*, 108(E9).

Matérn, B. (1960). Spatial variation, meddelanden fran statens skogsforskningsinstitut. *Lecture Notes in Statistics*, 36:21.

McGovern, P. J., Solomon, S. C., Smith, D. E., Zuber, M. T., Simons, M., Wieczorek, M. A., Phillips, R. J., Neumann, G. A., Aharonson, O., and Head, J. W. (2002). Localized gravity/topography admittance and correlation spectra on Mars: Implications for regional and global evolution. *Journal of Geophysical Research: Planets (1991–2012)*, 107(E12):19–1–19–25.

McGovern, P. J., Solomon, S. C., Smith, D. E., Zuber, M. T., Simons, M., Wieczorek, M. A., Phillips, R. J., Neumann, G. A., Aharonson, O., and Head, J. W. (2004). Correction to "Localized gravity/topography admittance and correlation spectra on Mars: Implications for regional and global evolution". *Journal of Geophysical Research: Planets*, 109(E7). E07007.

McKenzie, D. (2003). Estimating T_e in the presence of internal loads. *Journal of Geophysical Research: Solid Earth (1978–2012)*, 108(B9).

McKenzie, D. (2010). The influence of dynamically supported topography on estimates of T_e. *Earth and Planetary Science Letters*, 295(1):127–138.

McKenzie, D. (2015). A note on estimating T_e from Bouguer coherence. *GEM-International Journal on Geomathematics*, pages 1–14.

McKenzie, D., Barnett, D. N., and Yuan, D.-N. (2002). The relationship between Martian gravity and topography. *Earth and Planetary Science Letters*, 195(1):1–16.

McKenzie, D. and Bowin, C. (1976). The relationship between bathymetry and gravity in the Atlantic Ocean. *Journal of Geophysical Research*, 81(11):1903–1915.

McKenzie, D. and Fairhead, D. (1997). Estimates of the effective elastic thickness of the continental lithosphere from Bouguer and free air gravity anomalies. *Journal of Geophysical Research: Solid Earth (1978–2012)*, 102(B12):27523–27552.

Myung, I. J. (2003). Tutorial on maximum likelihood estimation. *Journal of mathematical Psychology*, 47(1):90–100.

Neumann, G., Zuber, M., Wieczorek, M., McGovern, P., Lemoine, F., and Smith, D. (2004). Crustal structure of Mars from gravity and topography. *Journal of Geophysical Research: Planets (1991–2012)*, 109(E8).

Nimmo, F. (2002). Admittance estimates of mean crustal thickness and density at the Martian hemispheric dichotomy. *Journal of Geophysical Research: Planets (1991–2012)*, 107(E11):27–1.

Pérez-Gussinyé, M., Lowry, A. R., Watts, A. B., and Velicogna, I. (2004). On the recovery of effective elastic thickness using spectral methods: examples from synthetic data and from the Fennoscandian Shield. *Journal of Geophysical Research: Solid Earth (1978–2012)*, 109(B10).

Phillips, R. J., Zuber, M. T., Smrekar, S. E., Mellon, M. T., Head, J. W., Tanaka, K. L., Putzig, N. E., Milkovich, S. M., Campbell, B. A., Plaut, J. J., et al. (2008). Mars north polar deposits: Stratigraphy, age, and geodynamical response. *Science*, 320(5880):1182–1185.

Seidelmann, P., Abalakin, V., Bursa, M., Davies, M., De Bergh, C., Lieske, J., Oberst, J., Simon, J., Standish, E., Stooke, P., et al. (2002). Report of the IAU/IAG working group on cartographic coordinates and rotational elements of the planets and satellites: 2000. *Celestial Mechanics and Dynamical Astronomy*, 82(1):83–111.

Simons, F. J. and Olhede, S. C. (2013). Maximum-likelihood estimation of lithospheric flexural rigidity, initial-loading fraction and load correlation, under isotropy. *Geophysical Journal International*, 193:1300–1342.

Simons, F. J., Zuber, M. T., and Korenaga, J. (2000). Isostatic response of the Australian lithosphere: Estimation of effective elastic thickness and anisotropy using multitaper spectral analysis. *Journal of Geophysical Research: Solid Earth (1978–2012)*, 105(B8):19163–19184.

Smith, D. E., Sjogren, W. L., Tyler, G. L., Balmino, G., Lemoine, F. G., and Konopliv, A. S. (1999a). The gravity field of Mars: results from Mars Global Surveyor. *Science*, 286(5437):94–97.

Smith, D. E., Zuber, M. T., Frey, H. V., Garvin, J. B., Head, J. W., Muhleman, D. O., Pettengill, G. H., Phillips, R. J., Solomon, S. C., Zwally, H. J., et al. (2001). Mars Orbiter Laser Altimeter: Experiment summary after the first year of global mapping of Mars. *Journal of Geophysical Research: Planets (1991–2012)*, 106(E10):23689–23722.

Smith, D. E., Zuber, M. T., Solomon, S. C., Phillips, R. J., Head, J. W., Garvin, J. B., Banerdt, W. B., Muhleman, D. O., Pettengill, G. H., Neumann, G. A., et al. (1999b). The global topography of Mars and implications for surface evolution. *Science*, 284(5419):1495–1503.

Stark, C., Stewart, J., and Ebinger, C. (2003). Wavelet transform mapping of effective elastic thickness and plate loading: Validation using synthetic data and application to the study of southern African tectonics. *Journal of Geophysical Research: Solid Earth (1978–2012)*, 108(B12).

Stein, M. (1999). *Interpolation of Spatial Data: Some Theory for Kriging*. Springer Series in Statistics. Springer New York.

Tesauro, M., Audet, P., Kaban, M. K., Bürgmann, R., and Cloetingh, S. (2012). The effective elastic thickness of the continental lithosphere: Comparison between rheological and inverse approaches. *Geochemistry, Geophysics, Geosystems*, 13(9).

Timoshenko, S. and Woinowsky-Krieger (1959). *Theory of plates and shells*, volume 2. McGraw-Hill, New York.

Turcotte, D., Willemann, R., Haxby, W., and Norberry, J. (1981). Role of membrane stresses in the support of planetary topography. *Journal of Geophysical Research: Solid Earth (1978–2012)*, 86(B5):3951–3959.

Turcotte, D. L., Shcherbakov, R., Malamud, B. D., and Kucinskas, A. B. (2002). Is the Martian crust also the Martian elastic lithosphere? *Journal of Geophysical Research: Planets (1991–2012)*, 107(E11):1–1.

Tyler, G. L., Balmino, G., Hinson, D. P., Sjogren, W. L., Smith, D. E., Woo, R., Asmar, S. W., Connally, M. J., Hamilton, C. L., and Simpson, R. A. (1992). Radio science investigations with Mars Observer. *Journal of Geophysical Research: Planets (1991–2012)*, 97(E5):7759–7779.

Watts, A. and Burov, E. (2003). Lithospheric strength and its relationship to the elastic and seismogenic layer thickness. *Earth and Planetary Science Letters*, 213(1):113–131.

Watts, A. B. (2001). *Isostasy and Flexure of the Lithosphere*. Cambridge University Press.

Wieczorek, M. A. (2007). The gravity and topography of the terrestrial planets. In Spohn, T., editor, *Planets and Moons: Treatise on Geophysics*, 5, pages 165–206. Elsevier.

Wieczorek, M. A. (2008). Constraints on the composition of the martian south polar cap from gravity and topography. *Icarus*, 196(2):506–517.

Wieczorek, M. A., Meschede, M., and Oshchepkov, I. (2015). SHTOOLS - Tools for working with spherical harmonics (v3.1).

Wieczorek, M. A. and Phillips, R. J. (1998). Potential anomalies on a sphere: Applications to the thickness of the lunar crust. *Journal of Geophysical Research: Planets (1991–2012)*, 103(E1):1715–1724.

Wieczorek, M. A. and Simons, F. J. (2005). Localized spectral analysis on the sphere. *Geophysical Journal International*, 162(3):655–675.

Wieczorek, M. A. and Zuber, M. T. (2004). Thickness of the Martian crust: Improved constraints from geoid-to-topography ratios. *Journal of Geophysical Research: Planets*, 109(E1).

Zuber, M. T. (2001). The crust and mantle of Mars. *Nature*, 412(6843):220–227.

Zuber, M. T., Solomon, S. C., Phillips, R. J., Smith, D. E., Tyler, G. L., Aharonson, O., Balmino, G., Banerdt, W. B., Head, J. W., Johnson, C. L., et al. (2000). Internal structure and early thermal evolution of Mars from Mars Global Surveyor topography and gravity. *Science*, 287(5459):1788–1793.